Italian National Agency for New Technologies,
Energy and Sustainable Economic Development

CONCEPTUAL DESIGN REPORT

A 250 GHz Radio Frequency CARM Source for Plasma Fusion

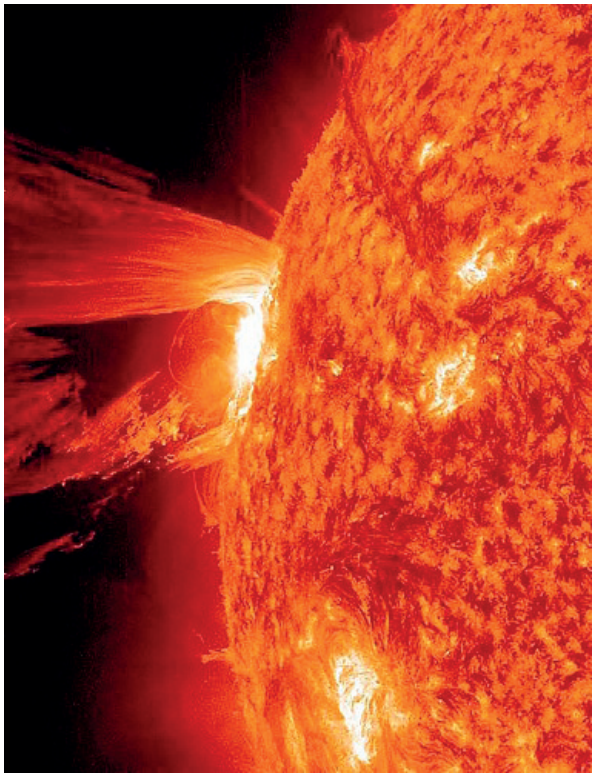

Conceptual Design Report

A 250 GHz Radio Frequency CARM Source for Plasma Fusion

Marcello Artioli [1], Massimo Aquilini [2], Ezio Campana [2], Mauro Cappelli [2], Mariano Carpanese [2], Silvio Ceccuzzi [2], Franco Ciocci [2], Giuseppe Dattoli [2], Domenico De Meis [2], Sergio Di Giovenale [2], Emanuele Di Palma [2], Luigi Di Pace [2], Andrea Doria [2], Gian Piero Gallerano [2], Naum S. Ginzburg [3], Emilio Giovenale [2], Mikhail Y. Glyavin [3], Alessandro Lampasi [2], Silvia Licciardi [2,4], Giuseppe Maffia [2], Luca Mezi [2], Francesco Mirizzi [5], Federico Nguyen [2], Simonetta Pagnutti [6], Nikolai Y. Peskovc [3], Alberto Petralia [2], Piero Petrolini [2], Aldo Pizzuto [2], Stefano Polenta [2], Bernardo Raspante [2], Gian Luca Ravera [2], Giuliano Rocchi [2], Elio Sabia [2], Andrey V. Savilovc [3], Ivan Spassovsky [2], Svilen Sabchevski [7], Benedetto Tilia [2], Angelo A. Tuccillo [2], Simonetta Turtù [2], Pietro Zito [2]

[1] Bologna Research Centre, Energy Efficiency Technical Unit, Via Martiri Monte Sole, 4, 40121, Bologna, Italy

[2] Frascati Research Centre, Fusion and Technology for Nuclear Safety and Security Department, Via Enrico Fermi 45, 00044, Frascati, Rome, Italy

[3] Institute of Applied Physics of the Russian Academy of Sciences, Dpt. of Plasma Physics and High-Power Electronics, 46 Ul'yanov Street, 603950, Nizhny Novgorod, Russia

[4] University of Catania, Department of Mathematics, Via Santa Sofia, 64, 95125 Catania, Italy

[5] Consorzio CREATE, Via Claudio 21, 80125, Naples, Italy

[6] Bologna Research Centre, Energy Technologies Department, Via Martiri Monte Sole, 4, 40121, Bologna, Italy

[7] Institute of Electronics of the Bulgarian Academy of Sciences, Department of Plasma Physics and Engineering, 72 Tzarigradsko Shose Blvd, 1784, Sofia, Bulgaria

2016 ENEA
National Agency for New Technologies, Energy and Sustainable Economic Development

ISBN 978-88-8286-339-5

Contents

Preface

We present the conceptual design for a Cyclotron Auto Resonance Maser source, operating at *250 GHz* and conceived for Plasma Fusion research activities.

The study discussed here is aimed at planning the construction of such a device at the ENEA Frascati Center, within the framework of the researches pertaining to the Fusion department. This foreseen activity gather together different skills traditionally present in the Agency and including Fusion, accelerator technology, beam handling and transport, superconductivity...

The report covers the different details of the project and is devided in two parts. The first contains a general description of the entire system, furthermore it describes the motivations underlying the choice of the device, the relevant theoretical foundations, the reasons for the choice of the operating parameters and the expected performances of the source.

In the second part the project details are reported and each constituting item is properly described in the technical annexes. We discuss indeed the cathode design and the electron beam shaping and transport, we report on the power supply and electrical pulse forming line, on the Superconducting magnet and CARM cavity characteristics. Finally we discuss the code development effort for the analysis of the radiation output performances.

Introduction

This report describes the conceptual design and development plan of a Cyclotron Auto Resonance Maser (CARM) for thermonuclear fusion experiments in magnetically confined machines of tokamak or stellarator type. The realization of a high-power, high-frequency CARM source is a mid-size, long-term, theoretical, and experimental project, whose various steps are discussed in this document. The technical design of most components and units can be carried out at the ENEA (Italian National Agency for New Technologies, Energy and Sustainable Economic Development) laboratories in Frascati (Rome, Italy) by a specifically established task force. Fabrication and tests have to be addressed in the frame of domestic and international collaborations with partner institutions and private companies.

The motivation that suggested to undertake this project is the unavailability of electromagnetic sources that fully meet the demands of future heating, current drive, and diagnostics systems in the Electron Cyclotron Range of Frequency (ECRF). The successful use of Electron Cyclotron (EC) waves in magnetic fusion devices has been demonstrated with reference to several applications. Among them, there are heating (ECRH), current drive (ECCD), plasma breakdown, assisted start-up, instability control, disruption avoidance, impurity control, and wall conditioning [1], [2]. Furthermore EC waves present peculiar features that favor their technology with respect to other radiofrequency systems. On the top of them there are the high power density injected through the port surface, the safe use of remote launching structures, and the position control of power absorption in the plasma thanks to real-time steering mirrors. Electron cyclotron systems are thus a fundamental tool in present-day fusion experiments as well as in next-generation tokamaks and stellarators.

Concerning the control of instability through EC waves, which is one of main applications of EC systems, it is worth mentioning a close analogy with Free Electron Laser (FEL) devices. In the recent past, a great deal of interest arose within the framework of FEL physics as a consequence of experimental evidences showing that the electron beam "heating", induced by the FEL interaction itself, provides the switch off of instabilities, like those of saw tooth type, head tail. . . , plaguing the operation of high intensity storage rings [3]. Furthermore the "FEL-Heater" became a routinely exploited device to suppress the synchrotron instability in high intensity

LINACs devoted to fourth generation synchrotron radiation sources.

The state of the art for ECRF sources is embodied by the *170 GHz*, *1 MW*, continuous wave (CW) gyrotrons developed for the International Tokamak Experimental Reactor (ITER) [4]. There is instead no vacuum tube capable of delivering the same amount of CW power at frequencies above *200 GHz*, as requested for optimal ECRF operations in the DEMOnstrator power plant (DEMO), which will be the ITER successor. The development of high-power sources at very high frequency, i.e., around *300 GHz*, is also needed for diagnostics applications as for instance for the Collective Thomson Scattering (CTS) in the Large Helical Device (LHD) [5].

Most of the experience, acquired so far, in the ECRH & CD field has relied upon the use of gyrotrons as microwave sources. A significant amount of progress has been done in this direction and further substantial R & D will be done in the future to meet EC system requirements in reactor conditions. The gyrotron technology has grown to a high maturity level, but there are still problems to be overcome to establish their full suitability in fulfilling the future demands of EC systems in the most effective way.

The quest for the parallel development of a different typology of devices is therefore justified. CARM sources have been viewed as promising devices since the *80*'s of the last century. The experimental effort put forward in the successive decade was frustrated by several technological issues, associated with the difficulties of getting a high quality intense electron beam, which did not allow the possibility of obtaining the required performances in terms of efficiency.

Major achievements in the design of cathodes providing high quality e-beam, along with significant improvements in analytical and numerical modeling capability and the availability of unprecedented computational resources, are the key issues to overcome the quoted technological drawbacks. These reasons motivate the proposal of a new CARM program research at ENEA Frascati.

The working frequency of the proposed CARM is chosen by taking into account the expected demands of reactor-relevant machines like DEMO with regard to EC waves. In July *2012* the institutions coordinating the fusion research in Europe released two DEMO models: a pulsed device with a flat top of *2* hours and a toroidal field of *6.8 T* and a steady-state machine with a toroidal field of *5.84 T*. Depending on the plasma density profile configurations (peaked or flat), the central electron temperatures range from *53 keV* to *64 keV*. The most suitable scheme for both EC heating and current drive is the low field side injection of the ordinary mode with absorption primarily at the fundamental resonance.

The relativistic wave-particle resonance condition is [6]

$$\gamma - \frac{n\Omega_p}{\omega} - N_{\parallel} u_{\parallel} = 0 \tag{1}$$

with n being the harmonic number, $\Omega_p = \dfrac{eB}{m_e}$ (the sub-index P refers to the electron cyclotron frequency inside the plasma) $\gamma = \sqrt{1+u^2}$ the relativistic Lorentz factor, u is the normalized momentum and $N_{\parallel}$ is the component of the refractive index $\left(N = \dfrac{ck}{\omega}\right)$ parallel to the equilibrium magnetic field. The parallel momentum component satisfying the resonance condition lies between the two roots

$$u_{\parallel,\pm} = \frac{N_{\parallel}\dfrac{n\Omega_p}{\omega} \pm \sqrt{\left(\dfrac{n\Omega_p}{\omega}\right)^2 - \left(1 - N_{\parallel}^2\right)}}{1 - N_{\parallel}} \tag{2}$$

the condition for the wave absorption is ensured by the reality of the roots provided by

$$\left(\frac{n\Omega_p}{\omega}\right) \geq \sqrt{\left(1 - N_{\parallel}^2\right)} \tag{3}$$

Furthermore, assuming a radial dependence of the magnetic field such that $\Omega_p = \Omega_p^0 \dfrac{R_0}{R}$, the point at which the absorption of the first harmonic is possible, is given by:

$$\begin{aligned} R &= \frac{\Omega_P^0 R_0}{\omega\sqrt{1 - N_{\parallel}^2}}, \\ \frac{\Omega_P^0}{2\,\pi}\,[GHz] &= 28\,B_0[T] \end{aligned} \tag{4}$$

where R_0 is the major radius of the torus. A contour plots of R versus frequency and $N_{\parallel}$ is given in Fig. 1, showing that the higher the wave frequency, the further the wave travels undamped, thus reaching more internal layers before being absorbed. Considering that the optimum current drive efficiency occurs at higher $N_{\parallel}$, the operational frequencies of *230* and *280 GHz* were proposed for the steady state and pulsed DEMO models, respectively. Such choice indeed allowed the EC waves with larger$N_{\parallel}$ to reach the geometrical axis of the tokamak, which was *8.5 m* and *9.6 m* for the steady-state and pulsed versions of DEMO.

The aforementioned DEMO options have been revised in *2015*, and a new model with a toroidal field of *5.67 T* became the reference design [7]. The latter is less demanding in terms of ECRH & CD system, notwithstanding, the frequency must exceed *200 GHz*. The European Consortium for the

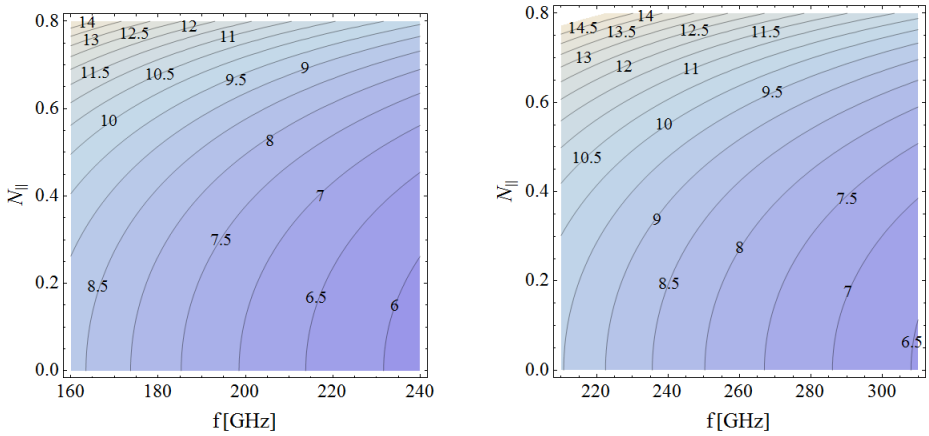

(a) Steady-state DEMO (b) Pulsed DEMO

Figure 1: Contour plots of the largest radial position $[m]$ for first harmonic absorption vs. plasma parallel refractive index and frequency.

Development of Fusion Energy (EUROfusion) is supporting the study of continuous wave gyrotron sources at frequencies around *240 GHz* [8], and future tokamak reactors will rely on higher toroidal fields, entailing the request for ECRF systems at higher working frequencies.

According to previous remarks, we fix the frequency of the CARM device to be developed at around *250 GHz*. This value represents a choice relevant to DEMO and to the expected ECRF systems in next-generation fusion reactors; moreover it enables the use on FTU to perform second-harmonic EC experiments with toroidal magnetic field intensities of around *4-5 T*. In medium size tokamaks, a reliable estimation of the suitable frequency for EC system can be indeed calculated with the practical formula

$$f\ [GHz] = 28\ nB_0 \tag{5}$$

that, for $n = 2$ and $B_0 = 4.46\ T$, yields $f = 250\ GHz$.

Regarding the amount of power, we will address our design to values around *1 MW* with electron efficiency of the order of *30%*.

It is worth stressing that this power level, even though insignificant for heating purposes, is interesting as local heater for instability damping [9].

level of power we have specified and the required efficiency above *30%* allows fixing the e-beam power around *3 MW*.

The structure of this document is the following:

1. **The introductory and motivational part consisting of *3* Chapters**

   In Ch. 1 we provide a quick review of the physical mechanisms underlying ECRH and clarify the reasons which suggested the design choices developed in this document. The theoretical aspects of CARM devices will be discussed in Ch. 2. A comparison between CARM and other heating sources will be discussed in Ch. 3, where we also discuss the ENEA activity in the field along with an analysis of previous proposals and R&D strategy regarding the various components.

2. **The design, consisting of *8* sections detailing the elements composing the CARM device**

   The relevant sections and the topics discussed are reported below

   - General layout design
   - Modulator and Power Supply
   - Gun and e-beam qualities
   - Electron Transport (Solenoids, CARM high field magnet)
   - Interaction region (resonant cavity)
   - Bragg reflectors (delimiting the resonant cavity itself)
   - Mode selection and operating configuration
   - Performance (output power and efficiency)

3. **Microwave Components and RF Optics**

   This Chapter is devided in *2* Sections regarding structure of the resonator and solutions involving the Bragg Reflector.

4. **Technical Annexes, detailing the design solutions**

   This part conteins Technical Addenda regarding specific design details outlined below.

   - General design considerations
   - Layout of the proposed solution
   - Design details
   - Control System

Chapter 1

Physical Foundations and Design Criteria

The coherent electromagnetic source, considered in this report, is a Free Electron Device of CARM type, designed to operate at *250 GHz* and driven by an e-beam having a ***"kinetic"*** power of few MW.

The device we propose is intended to deliver a power of the order of 1MW, with large enough efficiency to be interesting for FUSION applications.

The paradigmatic elements of any long wave-length free electron generator of coherent radiation are those reported in Fig. 1.1. The first stage of the device (framed in a blue circle) consists of an electron gun, producing and accelerating an electron beam, playing the role of power reservoir. The second part is provided by a waveguide immersed in a magnetic field, where the radiation is excited and stored

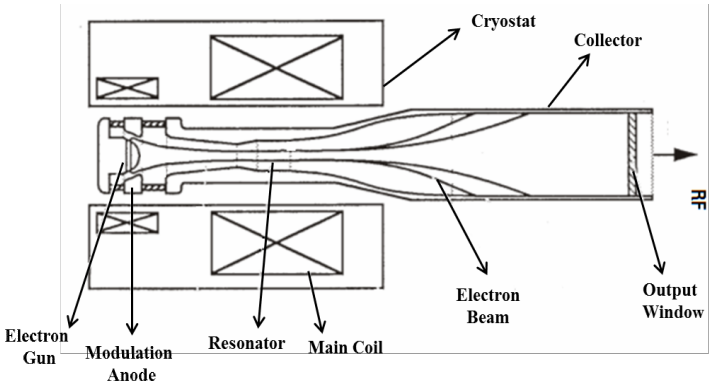

Figure 1.1: Layout of a Free Electron generator of coherent radiation.

The electrostatic accelerator is characterized by an accelerating potential V and delivers an e- beam with current I and suitable characteristics, in terms of energy and angular dispersions, allowing the most efficient cou-

pling to a selected mode of the resonant cavity itself. In any Free Electron generator of coherent radiation, the goal is that of subtracting a certain amount of power to the electron beam and to transform it into coherent electromagnetic power.

Without entering the specific mechanisms, allowing such an interplay, we write the field- beam power balance in the form

$$\begin{aligned} P_{RF} &= \hat{\eta}\, P_E \\ P_E &= IV \end{aligned} \tag{1.1}$$

The parameter $\hat{\eta}$ is the efficiency of the device, which is a measure of the capability of the system of converting the electron kinetic power (P_E) into radiating power (P_{RF}). The previous equation states a mere proportionality between radiation and e-beam power and can be exploited to figure out the characteristics of the e-beam in terms of current intensity. Inverting eq. (1.1) yields indeed

$$I = \frac{P_{RF}}{\hat{\eta} V} \tag{1.2}$$

Requiring therefore an RF power around $1\ MW$, an efficiency of $\hat{\eta} \cong 0.3$, and keeping a moderately relativistic beam with $V \cong 0.7\, MV$ we obtain a corresponding current around $5\ A$ and therefore a beam power around 3.5 MW.

The first part of this study will be therefore dedicated to the design of such an accelerator, in which the afore mentioned characteristics in terms of beam power and current is only an aspect of the problem, the relevance of the other Energy spread and angular dispersion will be discussed later in this section.

The next step is understanding how the other elements, regarding the intensity of the main magnetic field and the frequency selection as well, can be figured out. To this aim we need a few clarifying remarks.

Free Electron Laser (FEL) is an almost undefined term, which indicates different kinds of coherent electromagnetic sources with laser like properties; all these sharing, as common feature, the fact that the active medium consists of radiating electrons, not bound in a quantum atomic or molecular environment. Very crudely speaking, in these devices a "fraction" of the electron beam kinetic power is transformed into electromagnetic radiation. A major role in the design of these device is played by an appropriate definition of the "fraction" delivered by the electron beam to the electromagnetic intensity, which, in turn, fixes the efficiency of the device itself.

In a CARM-FEL a moderately relativistic e-beam is injected into the wave guide of a resonant cavity, where an axial static magnetic field constrains the electrons, travelling with relativistic factor γ, along an helical path characterized by a cyclotron frequency $\Omega_0 = \dfrac{e\,B}{m_e}$ and a period

$$\begin{aligned} \Lambda &= 2\,\pi\frac{c}{\Omega}, \\ \Omega &= \frac{\Omega_0}{\gamma} \end{aligned} \tag{1.3}$$

(see Fig. 1.2, where the relevant geometry is reported). The electrons are likely to lose power by "pumping" a selected cavity mode, provided that the appropriate resonance conditions are satisfied. The interaction process can be reduced to what is sketched in Fig. 1.1, namely an electron, with longitudinal velocity v_z, propagating in a longitudinal magnetic field in the presence of a co-propagating electromagnetic field characterized by a wave-vector k_z, linked to the wave phase velocity v_p and frequency by

$$k_z = \frac{\omega}{v_p} \tag{1.4}$$

The beam kinematical variables, which are specified by the longitudinal (v_z) and transverse ($v_\perp$) velocity components, are furthermore linked to the relativistic factor by:

$$\begin{aligned} \beta_z^2 + \beta_\perp^2 &= 1 - \gamma^{-2}, \\ \beta_{z,\perp} &= \frac{v_{z,\perp}}{c}, \\ \alpha &= \frac{v_\perp}{v_z} \end{aligned} \tag{1.5}$$

where α is the so called "*pitch factor*".

As already underscored the electron wave coupling occurs if the so called resonance condition is satisfied. To get such a condition we follow a rather straightforward argument.

Being the radiation and electron velocities different, we expect that at each helix path the radiation has overcome the electron by the quantity

$$\delta = (v_p - v_z)\,\frac{\Lambda}{c} \tag{1.6}$$

Since δ is linked to the phase advance of the electromagnetic wave with respect to the electrons, constructive interference of the wave front of the emitted radiation at the next period is ensured if

$$\delta = \lambda \tag{1.7}$$

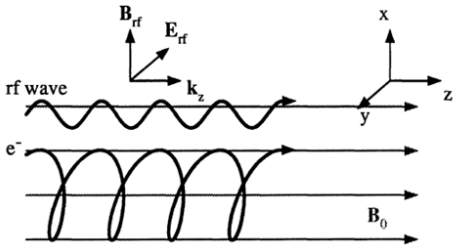

Figure 1.2: Geometry of the CARM interaction.

where λ is the frequency of the co-propagating field.

The use of eqs. (1.5)-(1.7) yields the following form for the CARM resonance condition

$$\omega = \frac{\Omega_0}{\gamma} + k_z c \beta_z \tag{1.8}$$

The above equation defines the wave frequency corresponding to a mode of the cavity which can exchange power with the electrons. Such a resonance condition depends on the magnetic field intensity, on the mode wave vector and on the electron kinematic quantities. Before drawing any further consequence from eq. (1.8), we note that it has been obtained on the basis of a simple kinematical argument. Which does not include any consideration relevant to the dispersive properties of the wave guide, where the interaction occurs. From the mathematical point of view the matching condition amounts to the simultaneous solution of eq. (1.8) and the corresponding dispersion equation for the cavity mode, namely

$$\omega^2 = c^2(k_\perp^2 + k_z^2) \tag{1.9}$$

where $k_\perp$ is the transverse mode wave number and $\omega_c = ck_\perp$ the associated cutoff frequency.

The (ω, k_z) plane (some-times called Brilluoin diagram) is a useful conceptual framework to understand the frequency selection mechanism in geometrical terms. It can indeed be viewed as the intersection between the straight line (1.4), characterized by an angular coefficient v_z , and the parabola (1.9) (see Fig. 1.3). Accordingly we find two roots

$$\omega_\pm = \Omega \frac{1 \pm \beta_z \sqrt{1 - (1-\beta_z^2)\left(\frac{\omega_c}{\Omega}\right)^2}}{1-\beta_z^2} \cong \Omega \frac{1 \pm \beta_z \left[1 - \frac{1}{2}(1-\beta_z^2)\left(\frac{\omega_c}{\Omega}\right)^2\right]}{1-\beta_z^2} \tag{1.10}$$

For any practical purpose, the last term in the square brackets can be neglected, so that the two roots, the up-shifted (+) and the down shifted (−), become

$$\begin{aligned}\omega_+ &\cong \frac{\Omega}{1-\beta_z} \equiv \text{CARM Frequency},\\ \omega_- &\cong \frac{\Omega}{1+\beta_z} \equiv \text{Gyrotron Frequency}\end{aligned} \tag{1.11}$$

The down shifted intersection (close to the cavity cutoff), some-times called gyrotron mode, is associated with the interaction of the electrons and a wave having much larger phase velocity, the relevance of this mode in the CARM operation will be discussed later in this section.

We will refer to ω_+ as the resonant (CARM) frequency and, to better understand its role, it will be rewritten as

$$\begin{aligned}\omega_R &\cong \frac{\Omega}{1-\beta_z} = \frac{\Omega}{1-\sqrt{1-\dfrac{1}{\gamma_z^2}}} \cong 2\,\gamma_z^2\Omega,\\ \gamma_z &= \frac{\gamma}{\sqrt{1+\bar{\alpha}^2}},\ \ \bar{\alpha} = \gamma\beta_\perp\end{aligned} \tag{1.12}$$

based upon the assumption that γ_z be sufficiently large that

$$\sqrt{1-\frac{1}{\gamma_z^2}} \cong 1-\frac{1}{2\gamma_z^2} \tag{1.13}$$

Eq. (1.12) accounts for the frequency Doppler up-shift mechanism, characterizing most of the free electron devices. The meaning of the second solutions will be discussed below. It is evident that eq. (1.12) are reconciled with eqs. (1.4)-(1.6) only if we assume that $\beta_p = \dfrac{v_p}{c} = 1$[1].

The electron energy is specified by

$$E = |e|\ V + m_e c^2 = \sqrt{\left(m_e c^2\right)^2 + c^2\left(p_z^2 + p_\perp^2\right)} \tag{1.14}$$

The relativistic factor is therefore given by

$$\gamma = \frac{|e|\ V}{m_e c^2} + 1 \tag{1.15}$$

By combining the equations on the frequency selection and the Hamiltonian (1.14) we end up with the following condition on the magnetic field necessary to get the resonance condition

[1] If we do not make such an assumption the expression for the phase velocity, obtained by comparing eqs. (1.4) and (1.6) is $\beta_p = \dfrac{1+\beta_z\sqrt{Q}}{\beta_z+\sqrt{Q}}$, $Q = 1-(1-\beta_z^2)\left(\dfrac{\omega_c}{\Omega}\right)^2$

$$B = \frac{m_e \omega_r}{|e|}\left[\frac{|e|\,V}{m_e c^2}+1\right]\left(1-\sqrt{1-\frac{\beta_\perp^2}{\beta_z^2+\beta_\perp^2}\left(\frac{|e|\,V}{m_e c^2}+1\right)^2}\right) \tag{1.16}$$

Requiring $f_r = \dfrac{\omega_r}{2\,\pi} \cong 250\,GHz$ we find a corresponding magnetic field intensity of the principal coil $B \cong 5\,T$

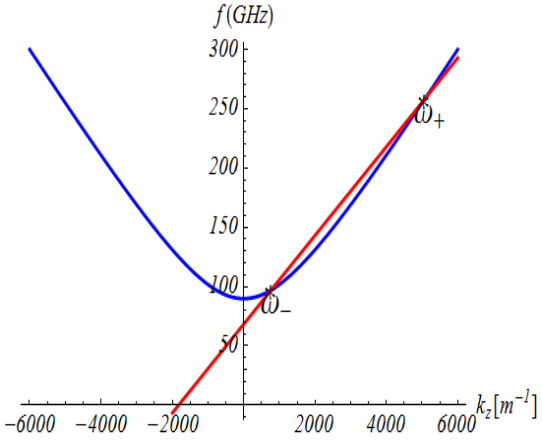

Figure 1.3: CARM Brillouin diagram and position of the CARM upshifted and gyrotron frequencies.

We have so far provided an indication for the electron beam current, energy and magnetic field but we did not mention what are the appropriate characteristics of the beam in terms of the quality of the energetic and angular distributions.

The technical annex, devoted to the numerical analysis of the CARM process, contains a detailed report of the impact of the beam distribution and of the relevant energy and angular dispersion, in this section we use heuristic arguments to infer the relevant role on the radiation output performances.

The dynamical behavior of any FEL type device is characterized by a first phase in which the interaction of the electrons with the cavity electromagnetic field mode determines their energy modulation, which turns into a density modulation, followed by a coherent RF emission, when the electrons are bunched on a scale comparable to the RF electric field wavelength. The field growth is finally counteracted by the saturation mechanism. This effect is due to an increase of the e-beam energy spread, determining a dilution of the gain and to the reduction of energy of the electron beam, which causes the loss of the resonance condition.

Regarding this last point CARM devices are peculiar with respect to the other Free Electron generators, because the auto-resonance is guaranteed

even near saturation. Any increase of Ω is indeed balanced by a corresponding decrease of the longitudinal velocity (see eq. (1.12)). This mechanism is in turn responsible for the intrinsic high efficiency of these devices. The Brilluoin diagram can be exploited to gain a geometrical insight into this effect, as shown in Fig. 1.4, where the different slopes associated with the electron line represent the energy variation during the interaction, while the intersection with the mode of the dispersion curves remains fixed.

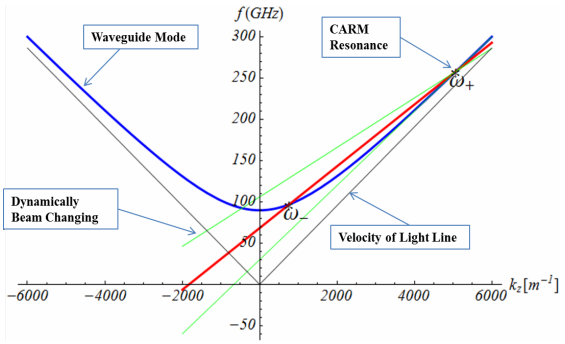

Figure 1.4: Brillouin diagram and auto-resonance mechanism.

In eq. (1.1) we have linked the CARM power to the electron beam power via the proportionality coefficient $\hat{\eta}$ defining the efficiency of the process. The peculiar nature of the process requires a distinction between single particle $\hat{\eta}_{sp}$ and collective efficiency $\hat{\eta}_C$ which yield

$$\hat{\eta} = \hat{\eta}_{sp}\hat{\eta}_C \tag{1.17}$$

The single particle contribution is easily calculated using the standard argument exploited for conventional FEL physics. The energy which can be subtracted to one electron is linked to the width of the gain curve; the power transfer process switch off when the energy lost by the electrons bring the system out of resonance, we find therefore (see technical Annex D)

$$\eta_{sp} \cong \frac{\Delta E}{E} \cong \frac{\Lambda}{L} \tag{1.18}$$

where L is the interaction length. As shown in the Annex D, $\dfrac{L}{\Lambda}$ yields the number of helix passes in one interaction length, thus providing an analogy with conventional undulator based FEL devices.

The further term is fixed by other kinematical quantities associated with the kinematical quantities linked to the longitudinal and transverse velocities and to the velocity phase difference between radiation and electrons, namely (see Annex D)

$$\hat{\eta}_{\mathrm{C}} \cong \frac{1}{(1-\beta_p^{-2})\,(1-\gamma_0^{-1})}\frac{\beta_\perp^2}{b},$$
$$b = \frac{\beta_\perp^2}{2\,\beta_z\beta_p\left(1-\dfrac{\beta_z}{\beta_p}\right)} \tag{1.19}$$

thus finally getting

$$\mathrm{P_S} \cong \frac{1}{(1-\beta_p^{-2})\,(1-\gamma_0^{-1})\,N}\frac{\beta_\perp^2}{b}P_E \tag{1.20}$$

This is a rough indication, to be refined in the following, but useful to get an idea of the efficiency we should expect with the previously fixed parameters, which yield $\hat{\eta} \cong 30\%$. This is however not the end of the story, because, as shown in Fig. 1.5, the efficiency is extremely sensitive to the beam characteristics. An inspection to the figure shows that if the velocity spread slightly increases we may expect a significant decrement of the efficiency. To be on the safe side and ensure an operation of the CARM device with a sufficiently large efficiency the driving the use of a beam of electrons with "reasonably" small dispersion of the energy and velocity distributions. We can obtain an upper limit to the previously quoted dispersions, by noting that

1. The inhomogeneous line broadening induced by the longitudinal velocity spread is (see eqs. (1.12), (1.14))

$$\left\langle\frac{\Delta\omega}{\omega}\right\rangle \cong \frac{\sigma_{\beta_z}}{1-\beta_z} \tag{1.21}$$

   requiring that it be smaller than its homogeneous counterpart we end up with the following condition on σ_{β_z}

$$\frac{\sigma_{\beta_z}}{1-\beta_z} < \frac{1}{N} \tag{1.22}$$

2. From eq. (1.5) we end up with

$$\alpha^2\sigma_{\beta_z} + \sigma_{\beta_\perp} = \frac{1}{\bar{\alpha}}\sigma_\gamma \tag{1.23}$$

   Using therefore $\sigma_{\beta_\perp} \leq 10^{-3}$ (as suggested by Fig. 1.5) and $\sigma_{\beta_z} \leq 3{\cdot}10^{-3}$ (as derived from eq. (1.22)) we find $\sigma_\gamma \leq 0.5\%$.

We can finally summarize in Tab. 1.1 the design request for the electron beam and the magnetic field.

The numbers reported in the previous table fix the conditions for a safe operation of the CARM device, but do not specify the form of operation,

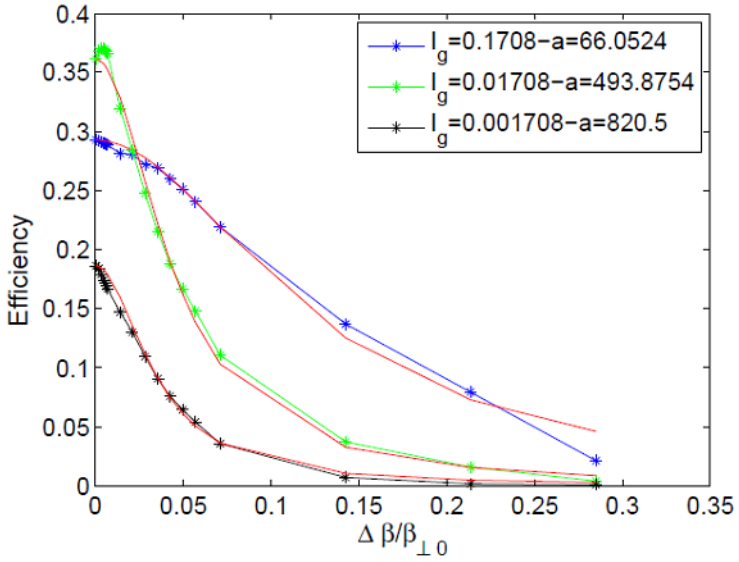

Figure 1.5: CARM efficiency vs. transverse energy spread.

Table 1.1: **Preliminary Design Parameters**

Beam current	5 A
Beam voltage	700 kV
Longitudinal and transverse Velocity Spread	< 0.3 %
Energy spread	< 0.5 %
Magnetic Field	5 T

which can be either an amplifier or an oscillator. Within the present framework, the latter is more convenient for various reasons: it removes the quest for an input source and input couplers, requires a shorter length of the interaction region, with the consequent need of a long high field intensity magnet. Furthermore the amplifier operation demands for the suppression of the backward-wave instability.

In order to ensure the CARM oscillations in the desired Doppler shifted frequency, it will be necessary to design the system in such a way that the relevant threshold current be less than that of the competing modes. This will be done by an appropriate choice of the beam and cavity parameters, as properly discussed in the Annex D.

The structure we are foreseen is that reported in Fig. 1.6a . The resonator is provided by a Bragg reflector, whose geometry is reported in Fig. 1.6b. The Q of the resonator is optimized to fix the appropriate threshold current for the desired mode selection (see Annex D).

The on-set of the gyrotron mode is prevented by an appropriate choice of the beam pitch ratio and by a suitable design of the relevant Q which is

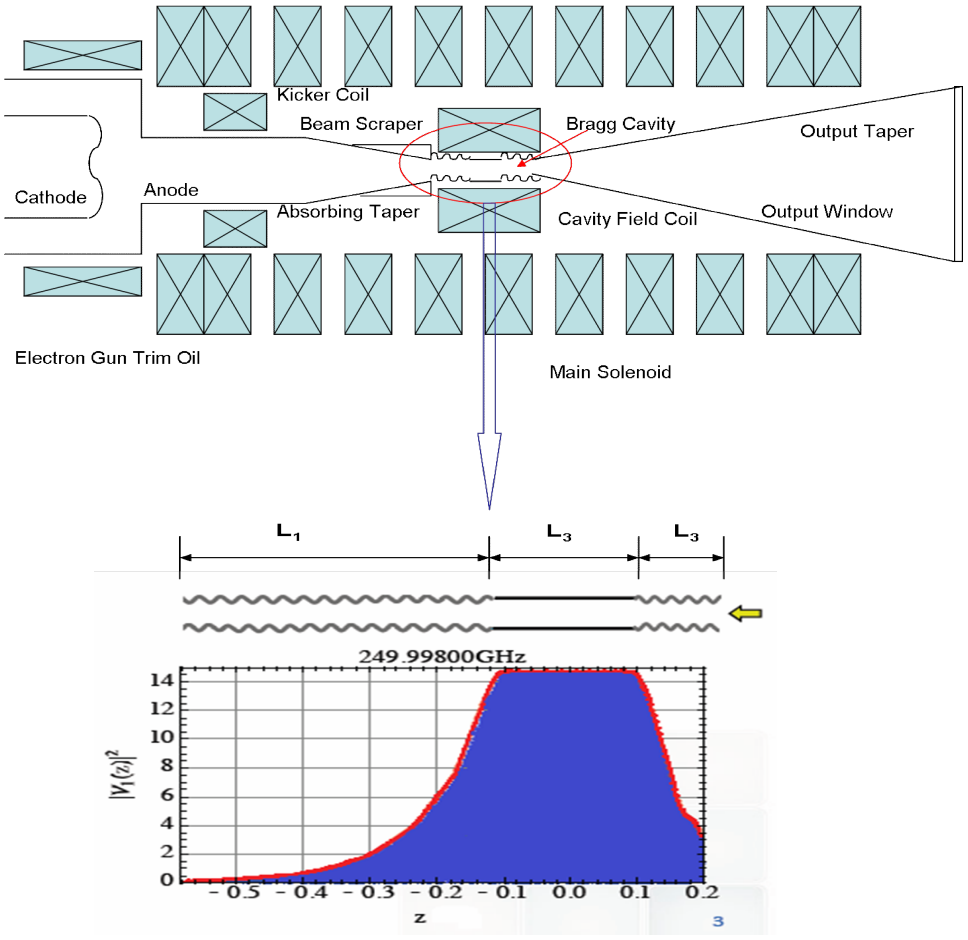

Figure 1.6: Layout of the CARM interaction with schematic of the oscillator and electric field distribution.

kept as low as possible.

The results of the various optimizations are reported in Tab. 1.1 representing our design parameters.

Chapter 2

General Layout

In the previous section it has been put in evidence that the final aim of this study is the realization of a CARM source delivering *1 MW* at *250 GHz* with an efficiency of *30%* , In this section instead is given an overview of the various elements composing the device, whose layout is reported in Fig. 2.1.

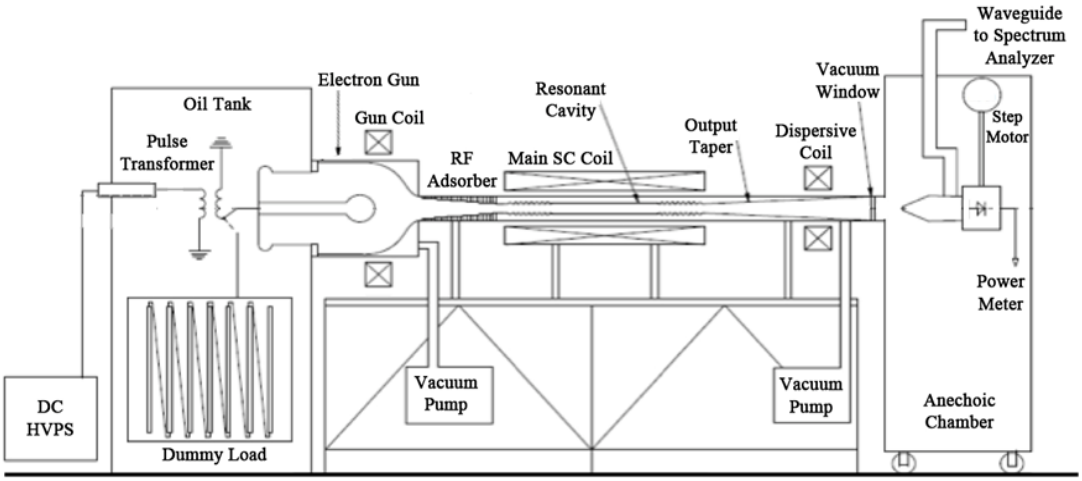

Figure 2.1: Layout of the CARM source including all the ancillary devices.

The relevant components are listed below:

a) High Voltage Modulator

b) Electron Gun

c) RF Circuit

d) Magnetic Circuit

e) Beam Dump

f) Vacuum System

g) Supporting Structure

h) Diagnostic Tools

i) Cold Test Facility

j) Experimental Room

k) Control Room and Control System

a) ***High Voltage Modulator***

The High Voltage Modulator is one of the most crucial, complex and expensive part of the whole CARM system. The relevant complexity comes from the noteworthy required stability of its electrical parameters, comparable to that of the modulators for High Power Klystrons.

The design and realization complexity has suggested the strategy of developing the ENEA CARM project in two steps.

The first step is mainly aimed at the realization of a CARM device to be tested in pulsed operation, with a maximum pulse length of *50* μs, at low repetition rate. With these tests the CARM electrical parameters will be optimized for maximizing the output power at the nominal output frequency.

The second step is instead aimed at developing a long pulse to CW CARM prototype equipped with a depressed collector for beam energy recovery, and a Vlasov-like output mode converter to conveniently extract the RF power.

Due to the power losses into the RF circuit, an intensive, forced water, cooling circuit will be necessary.

The main difference between the two steps is in the pulse length, even if rise and fall times and flat top accuracy of the pulses will be the same for both the steps. A different design approach will be therefore required for the HV modulator (see *Ch. IV*).

The single shot operation is an easiest way to test the single components and parts of the CARM and the CARM assembly as a whole. Apart of the Modulator all the other CARM components and units are or will be designed for CW operation. The pulsed modulator for the first step will cover the pulse length range from *1* to *50* μs with a voltage tunability of *0.1%* at the maximum output voltage of *700* kV. The other two important modulator parameters are the voltage ripple and the flat top smoothness, which should be in the range of *0.1%* too.

The modulator will be fully immersed in a metallic oil tank together with a dummy load and the cathode holder of the Electron Gun.

b) ***Electron Gun***

The electron beam is emitted and formed inside a diode type electron gun and then transported through a drift tube immersed in a direct high magnetic field. Most of the resulting helical beam properties are strongly dependent on the gun design. In general the electron beam is very sensitive to small changes of the emitter dimensions, emitter surface roughness and to its chemical properties. The road map followed during the preliminary design of the electron gun is the limitation of both the maximum surface electric field and the initial electrons velocity spread.

As a rule of thumb, for a gun designed for CW operation, the surface electric field at any point inside the gun region must be less than $10\ kV/mm$.

The electron velocity spread is determined by the geometrical shape of the electrodes, their surface roughness, the emitter temperature and its uniformity over the whole emitter surface.

The space charge effect is proportional to the beam current density and is known as an emitter current load. In the preliminary design of the emitter the current density has been limited to $3\ A/cm^2$, a value that will assure it a long lifetime ($> 10.000\ h$). The emitter operational temperature was limited to $1300\ ^{\circ}C$ to minimize the electron beam initial thermal velocity spread and to increase the emitter resistance to poisoning. These values are lower than the present technological limits and will guarantee the highest possible beam quality.

c) ***RF Circuit***

The CARM RF circuit is the assembly of the RF cavity, the RF beam expander provided by the output tapered bringing the radiation to the vacuum window. Any component is designed for CW operation.

Within the RF resonant cavity of a CARM, usually oscillating in a TE_{mnp} mode, the electron beam energy is partially transferred to the high frequency electric field. The energy transfer efficiency depends on the electron beam quality, mainly determined by a high performance gun design. The efficiency level also depends on the appropriate coupling between the electron beam and the cavity $TEmnp$ mode. The RF cavity must therefore guarantee an efficient beam interaction with the generated electromagnetic wave, characterized by a Doppler up shifted frequency, and the suppression of the down shifted (cutoff) counterpart. The mode selection is therefore of crucial importance for the CARM efficiency.

An oversized cylindrical cavity, which dimensions are set by the acceptable RF power dissipation limits on the cavity wall and by the electric breakdown in vacuum, will be used. In general it is extremely difficult to design a stable high Q cavity operating far from the cutoff. In addition the electron beam geometry along the CARM longitudinal axis has to be accurately studied because any interaction with the cavity walls, mainly during CW operations, must be absolutely avoided.

In this frame, the use of a quasi-optical resonant cavity, even though a fairly natural solution from the conceptual point of view in this frequency range, has been "a priori" discarded because of the thermal loads induced by the RF on the reflecting mirrors and also because of the difficulties with the electron beam transport.

The solution adopted for the ENEA CARM is a cylindrical smooth cavity delimited by Bragg reflectors, which, although complicated from the mechanical point of view, provides a distributed feedback and does not exhibit crucial drawbacks on the cavity cooling and on the electron beam transport.

The resonant cavity is connected to the larger CARM circular output waveguide through an accurately designed taper able to avoid any accidental mode conversion. The electron beam waste energy is dissipated on the CARM collector while the microwave radiation is launched into an anechoic chamber through a short circular transmission line. A CVD circular vacuum window, axially brazed on the collector wall, separates the evacuated CARM device from the transmission line. The optimum vacuum level is assured by a suitable pumping system assisted by an accurate mechanical design of the CARM RF inner components.

The CARM prototype object of the second design step, will be completed with an output mode converter, transforming the TE_{mn} operational mode into a gaussian RF beam, and with a depressed collector in order to increase the overall efficiency of the device.

d) ***Magnetic Transport System***

The magnetic channel provides the correct electron beam formation before the injection into the cavity. It consists of a gun coil, a large cavity coil and a kicker coil. On the occurrence an additional correcting coil, positioned before the cavity coil, will be used to properly shape the desired magnetic field topology along the CARM longitudinal axis. All the components of the CARM assembly must be aligned very accurately along the CARM horizontal axis in order to realize an efficient beam transport and an optimal beam–RF coupling into the resonant cavity.

The gun coil encircles the gun region of the CARM and provides the necessary magnetic field for an appropriate electron beam emission and transport inside the diode.

The design of this coil has been done with the help of the CST tracking code to obtain the proper magnetic field intensity, which, in synergy with the static electric field inside the diode, allows the most appropriate electron beam kinematic conditions at the input of the RF cavity for the optimum CARM operations.

The relatively weak magnetic field in the gun region can be obtained by a short, water-cooled, coil. Its diameter must be larger than the grounded gun electrode. Its large cross section, short length and significant weight require a sophisticate supporting structure and an accurate alignment procedure.

The cavity magnetic field, due to its relatively high intensity, will be provided by a superconducting magnetic coil.

Both length and field intensity profile of the cavity coil have been evaluated by following the induced electron motion trajectory tracking along the system.

The design of additional coils for an accurate field profile correction is however foreseen to optimize the beam-wave interaction.

d.2) ***Kicker Coil***

The magnetic system includes also a kicker coil that generates a field with a nominal value in the range *0.08 - 0.1 T*, perpendicular to the longitudinal CARM axis. This coil is aimed at removing any stray electrons by forcing them into the grounded wall .

e) ***Beam Dump***

Once left the resonant cavity region, the exhaust electron beam is uniformly spread on the collector walls, where its waste energy is finally dissipated.

The impact of the high-energy electron beams (*700 keV*) of the ENEA CARM on the metallic collector walls generates hence a significant amount of X-ray radiation by bremsstrahlung. Thus the beam dump has to be carefully designed for absorbing the X-ray flux. Usually a multi-layered lead screen encloses this part to protect the surrounding area from the stray X-ray radiation. The beam impact also heats the CARM collector due to both

scattering and ohmic losses. Therefore, the beam dump is cooled through suitable water pipes brazed on the outer part of its wall.

f) ***Vacuum System***

An efficient vacuum system is of capital importance for the correct operation of any high-power microwave tube. This system is designed to maintain inside the CARM an extremely low pressure at high pumping rate. In general a bad vacuum level is responsible for two extremely dangerous phenomena. The first one is a vacuum breakdown due to a high electric field across the electrode gaps. The second one is a surface breakdown due to a high surface electric field. There are rules regulating the limiting values for both cases that must be strictly respected during the design.

The CARM region under vacuum is about two meters long with a minimum cross-section radius of *15 mm*. The very first CARM prototype will operate at pulse lengths up to *50* μs. Thus to maintain a pulse repetition rate of *10 Hz*, a double side pumping is required. Most of the components in the evacuated region cannot be slotted or drilled for a better pumping performance. Thus these components need to be carefully designed from the mechanical point of view in order to assure a suitable vacuum level around them.

A low vacuum level is also important for the emitter just to avoid a poisoning possibility. A special chemical treatment of the components assembled in the vacuum region before the final assembling has been therefore considered.

$g-h$) ***Supporting Stucture & Diagnostics***

An anechoic chamber is the most important diagnostic tool for characterizing a CARM device. It is a large metallic box, whose inner walls are lined with microwave absorbing material, pyramidally shaped for reducing the RF reflections. This chamber in practice simulates the free space propagation. The microwave pattern generated by the CARM output waveguide inside the anechoic chamber is sampled with a horn pickup, an open-ended rectangular waveguide with a cut off frequency of about *170 GHz*, externally dressed by RF absorbing epoxy foam. The microwave signal picked up by the horn is split by two. One half of this signal is directly sent to a power meter, the second half is instead sent to a frequency spectrum analyzer in order to have a complete characterization of the RF power launched in the vacuum chamber. The horn is supported by a dielectric rod and moved inside the anechoic room by a remotely controlled motor. The total emitted RF power can be measured by mapping the radial pattern of the microwave radiation and then by integrating it over the whole chamber volume.

i) ***Cold Test Facility***

The Cold Test facility is an important section of any microwave laboratory aimed either at the development of new devices or at the characterization of the existing ones. The optimum performances of any microwave devices in facts depend on the accuracy of the cold tests.

The frequency of the ENEA CARM is part of a not completely explored sector of the frequency spectrum, so that many microwave components, also necessary for completing the cold test facility, must be expressly designed and developed at home. In particular a complex mode converter for feeding the CARM cylindrical resonant cavity in the TE_{53} mode, starting from the TE_{10} mode generated by a network analyzer in rectangular waveguide, is presently investigated.

A preliminary list of an essential outfit for our cold test facility is given in the following:

1. Network analyzer with output frequency up to *300 GHz*,
2. Mode converters from the TE_{10} mode in rectangular waveguide (*WR 3* or *WR 4*) to the cavity mode (i.e. the TE_{53}) in circular waveguide.
3. Circular tapers to connect the previous mode converter to the oversized circular waveguide of the resonant cavity.
4. Splitters, bends, attenuators, phase shifters, directional couplers and so on.

A more comprehensive analysis of microwave components to be developed for the CARM design and test is given in the Technical Addendum F.

j − *k*) ***Experimental Room, Control Room and Control System***

See Annex K.

Chapter 3

Gun Design and e-Beam Qualities

According to the discussion reported in Ch. I, the generation of an electron beam with appropriate qualities is the prerequisite to achieve the desired CARM performances.

A thermionic gun has been designed and proven to be a suitable tool for the production of the electron beam with the foreseen velocity and angular spread. In Table 3.1 we have summarized the design parameters of the gun-beam system.

Table 3.1: **Gun properties**

Cathode Voltage	$500 \div 700\ kV$
Relativistic Factor γ	$2 \div 2.4$
Beam Current	$1 \div 10\ A$
Pitch ratio $(v_\perp/v_\parallel)$	γ^{-1}
Axial and transverse velocity spread	$< 0.5\ \%$
Electric field at the cathode surface	$< 10\ kV/mm$

The considered gun is essentially a diode, which, unlike the triode gun used for gyrotron, is a non-adiabatic device. The relevant constituents: the cathode and the anode, are shown in Fig. 3.1.

The gun parameters of Table 3.1 have been figured out on the basis of a simple argument, which takes the heating power as pivoting reference. RF and electron beam power are linked by

$$P_{e-b} = \frac{P}{\hat{\eta}} \tag{3.1}$$

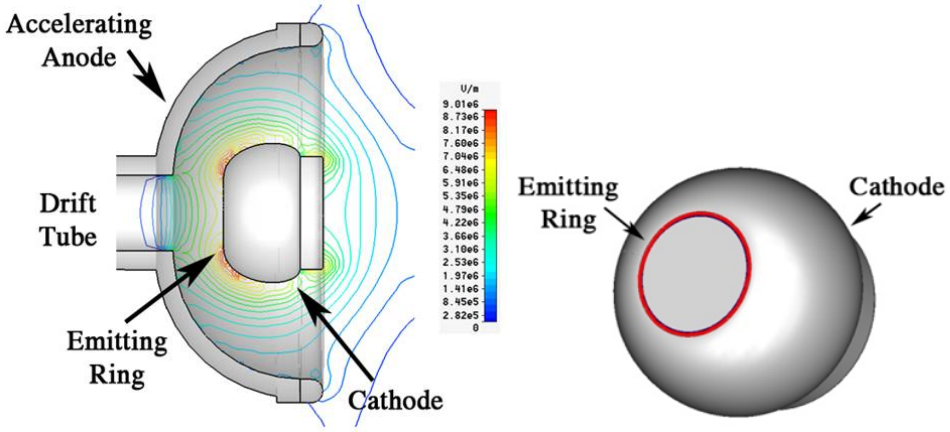

Figure 3.1: a) Diode-like gun, b) Emitter ring.

Furthermore, since P_{e-b} is given by the product of the current time the accelerating voltage

$$P_{e-b} = IV \tag{3.2}$$

we obtain

$$I = \frac{P}{\hat{\eta}\, V} \tag{3.3}$$

If we require a total electron efficiency around *30%* and demand for a CARM rf power of about *1 MW* we find for the corresponding e-beam power $P_{e-b} \cong 3\, MW$, which can be achieved by imposing suitable constraints on the accelerating voltage and beam current.

The efficiency of *30%* can be obtained if the beam energy spread is suitably small, therefore the most convenient design solution is that of as high as possible accelerating voltage to increase the e-beam kinetic energy and a low current to avoid additional velocity spread, induced by the space charge effects. By choosing e.g. an accelerating voltage of *600 kV*, the resulting beam current is about *4.5 A*.

A non-secondary issue in the design of the gun is the necessity of producing an electron beam with a ring shape to be positioned on a selected radial RF-field maximum of the desired cavity mode, allowing the optimum coupling conditions. Usually, those devices use the whispering gallery modes for operation which determines the beam profile (see Fig. 3.1). The electrons emitted from the ring are pushed ahead by the strong electrostatic field given by the accelerating tension and are guided by a longitudinal magnetostatic field generated by a gun coil.

Having specified the value of the accelerating voltage we can provide a first idea of the relevant geometrical dimensions by starting from the

following relation between the cathode and anode radii $R_{cath,an}$ in the case of a spherical shape

$$R_{cath} \;=\; \frac{R_{an}}{2}\left(1 \;-\; \sqrt{1 \;-\; 4\,\frac{V}{E_{surf}R_{an}}}\right) \tag{3.4}$$

which implies an equilibrium condition between the accelerating field V and the electric field E_{surf} at the cathode surface . The condition to be fulfilled to ensure the positivity of the of the argument of the square root in the previous equation is

$$R_{an} \leq\; 4\,\frac{V}{E_{surf}} \tag{3.5}$$

the use of the threshold value of $E_{surf} \cong 10^7\,\dfrac{V}{m}$, ensuring no cold field emission effects, implies $R_{an} \cong$ *30 cm*.

The electron beam generation and transport can be roughly divided in three parts:

a) The electrons are emitted from a circular corona at the cathode emitting surface, which is kept flat to ensure an homogeneous longitudinal velocity. At the exit of the corona the electrons are captured by the gun accelerating (longitudinal) field and guided by a superimposed static magnetic field, focusing the beam by compensating the transverse components of the velocity, induced by a transverse electric field having a cusp at the transition edge of the diode and drift tube (see Fig. 3.2a).

b) Near the drift tube the electrons receive a transversal kick induced by the transverse electric field acting as a beam defocusing lens.

c) Inside the drift tube the electron beam undergoes the combined effect of the fringing fields of the gun coil and the cavity coils (Figs. 3.2a, 3.2b and Figs. 3.3a, 3.3b) .

The longitudinal and transverse velocities (in m/s) along the gun (axis) in mm is shown in Figs. 3.3a, 3.3b respectively.

The longitudinal and transverse relative velocity spread are reported in Figs. 3.4a e 3.4b respectively, while the pitch ratio is shown in Fig. 3.5. The results provided by the simulation are compatible with the homogeneity requests quoted in the previous sections.

The proposed gun design is based on a non-adiabatic electric field solution, with a transverse component in correspondence of the ending edge of the diode (see Fig. 3.2b). The magnitude of the effect can be easily understood, the use the standard formulae for the Pierce gun design, we write the electric field at anode

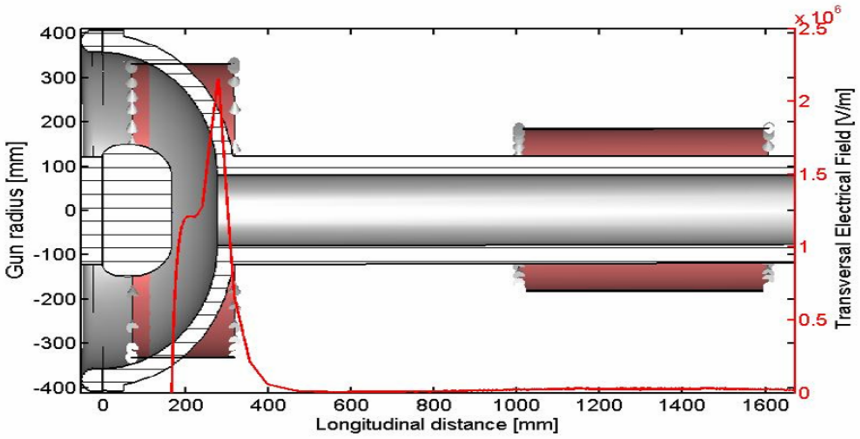

(a) Gun geometry.

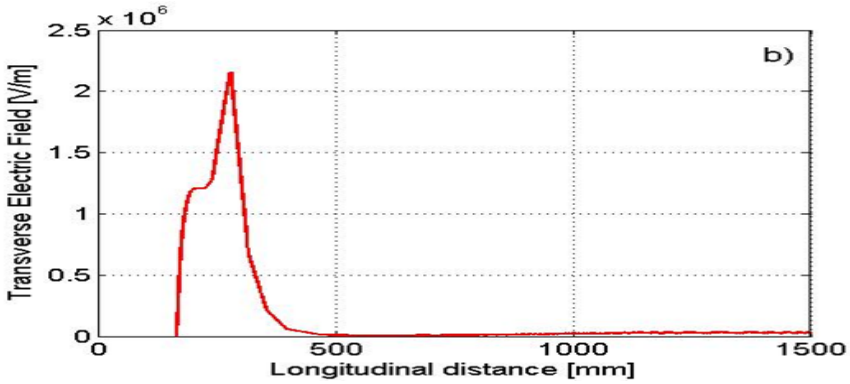

(b) Transverse electric field induced by the anode edge.

Figure 3.2: Longitudinal distance.

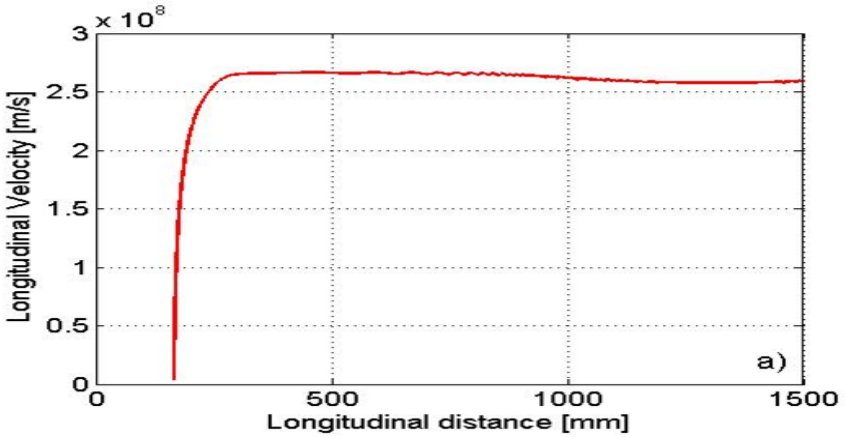

(a) Longitudinal velocity vs. $z[mm]$.

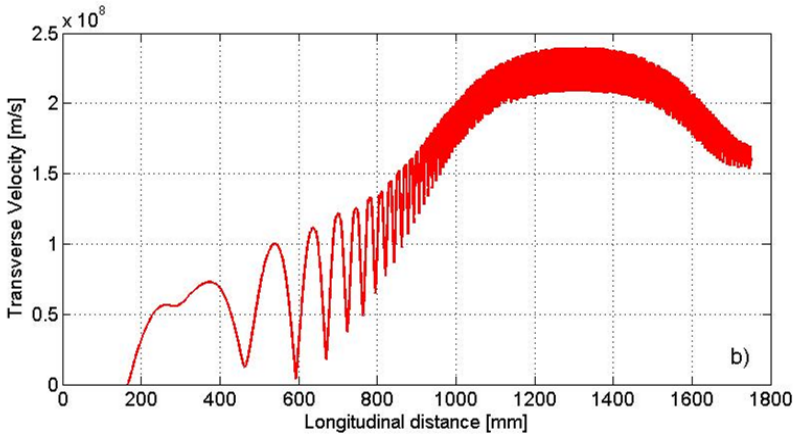

(b) Transverse velocity Component vs. $z[mm]$.

Figure 3.3: Longitudinal and transverse relative velocity spread.

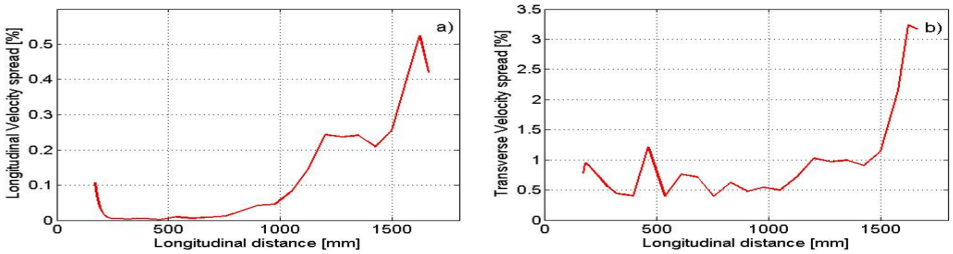

(a) Relative longitudinal velocity spread.

(b) Relative transverse velocity spread.

Figure 3.4: Velocity spread vs. z.

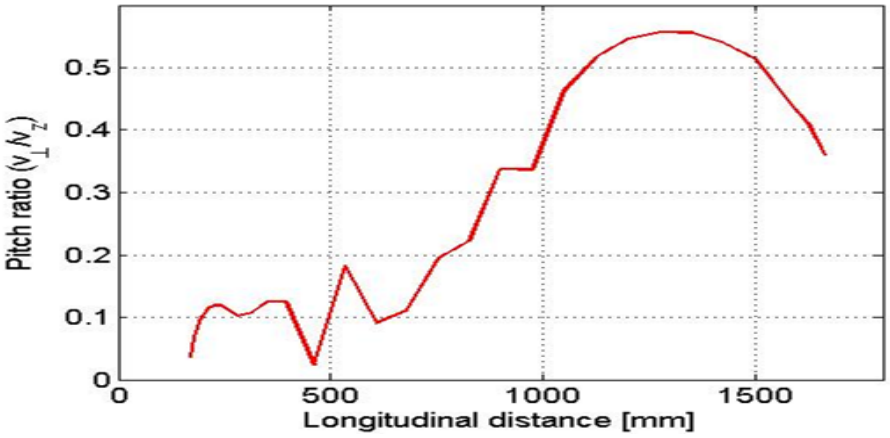

Figure 3.5: Pitch ratio vs. z.

$$E_A \cong \frac{V}{|R_{cath} - R_{an}|} \frac{R_{cath}}{R_{an}} \tag{3.6}$$

thus getting, for our design parameters an anode field value on the order of $10^6 \frac{V}{m}$, which agrees with the results provided by the simulation.

Owing to the cusp the effect of the field on the electrons can be viewed as a defocusing with a focal length specified by

$$f = -4\frac{V}{E} \cong -4\frac{\rho_c}{\rho_a}(\rho_c - \rho_a) \tag{3.7}$$

An idea of the relevant effect on the particle dynamics is given in Fig. 3.7, where the effect of the field edge on the transverse velocity is emphasized.

As already stressed, the electrons are produced in a ring shaped form to fulfill the optimum overlapping with the chosen operating mode inside the CARM cavity. In the technical annexes we will report the details of mode selection and the beam transport conditions ensuring the safe transport of the annular beam, along the line from the cathode to the interaction region.

In Figs. 3.7 we have reported the beam transverse section at different positions inside the channelfrom the cathode to the CARM cavity; the electrons are distributed along a circular corona ring and crucial parameters are

1. The average beam radius vs. z (see Fig. 3.8).

2. The beam corona section vs. z (see Fig. 3.9).

The beam is captured on a ring orbit with smaller radius inside the cavity, owing to the large strength of the CARM magnetic field. The radius

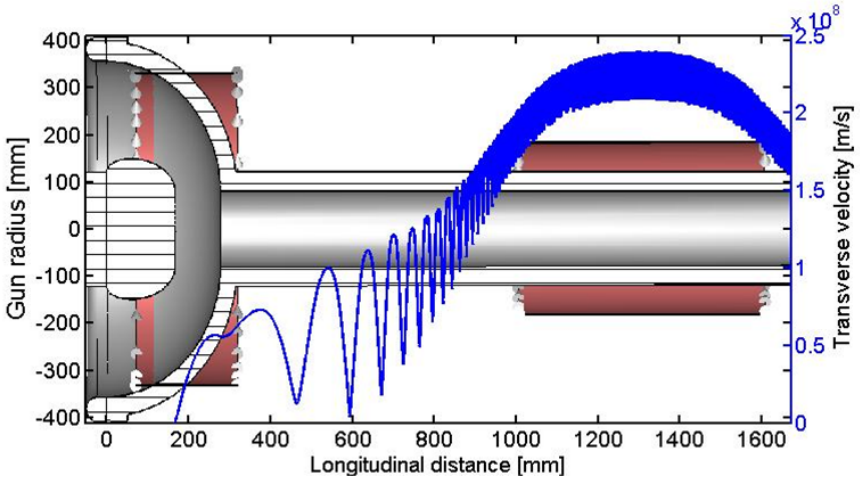

Figure 3.6: Transverse velocity from the cathode to the drift tube

stability is related to stability the magnetic field produced by the set of the solenoids. The width of the corona undergoes a kind of strong focusing effect yielding a minimum at the center of the cavity and is then defocused. The importance of the beam radius control comes from the coupling conditions with the CARM operating modes.

The preliminary considerations, developed in this section, show that the e-beam can be transported preserving its shape, which can be controlled to ensure the desired electron beam electromagnetic mode coupling in the resonant cavity. The specific design details are reported in the technical Annex C.

The beam shaping accuracy, with particular reference to its annular structure, is very important because strictly associated to the interaction between electrons and electric field modes in the resonant cavity, that critically depends on the beam shape and thickness along the cavity itself. It is evident that the mode excitation crucially depends on the portion of beam overlapping the structure of the transverse eigen-modes (see Fig.4, Technical Annex D). This mechanism is crucial for determining the number of excited modes, which can simultaneously grow and eventually induce a reduction of the CARM efficiency. The matching between electron beam and electric field in the resonant cavity will be therefore one of the pivotal topics of the next section.

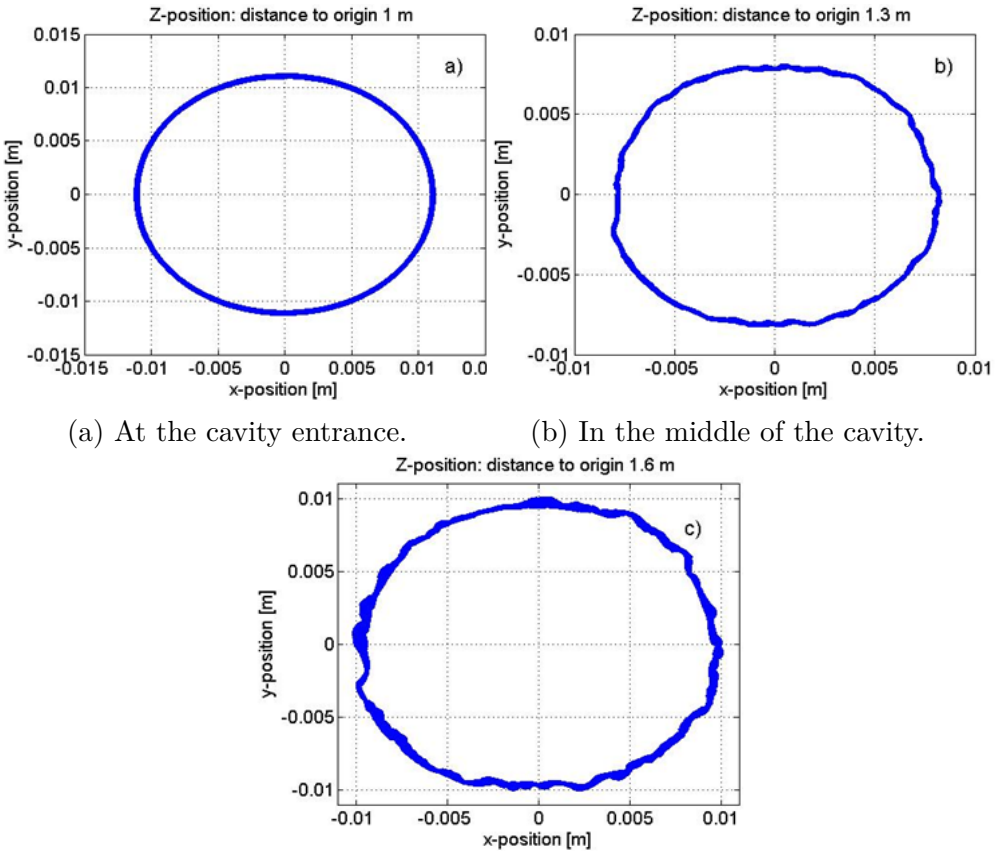

(a) At the cavity entrance. (b) In the middle of the cavity.

(c) At the cavity output.

Figure 3.7: e-Beam ring at different position along the transport line.

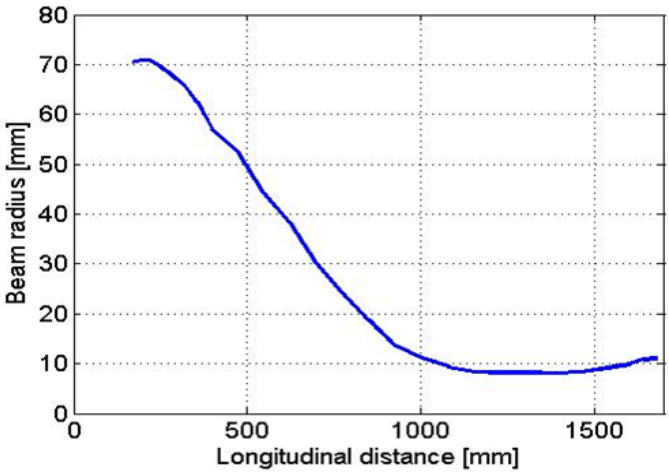

Figure 3.8: Average radius of the electron beam vs. longitudinal coordinate $z[mm]$.

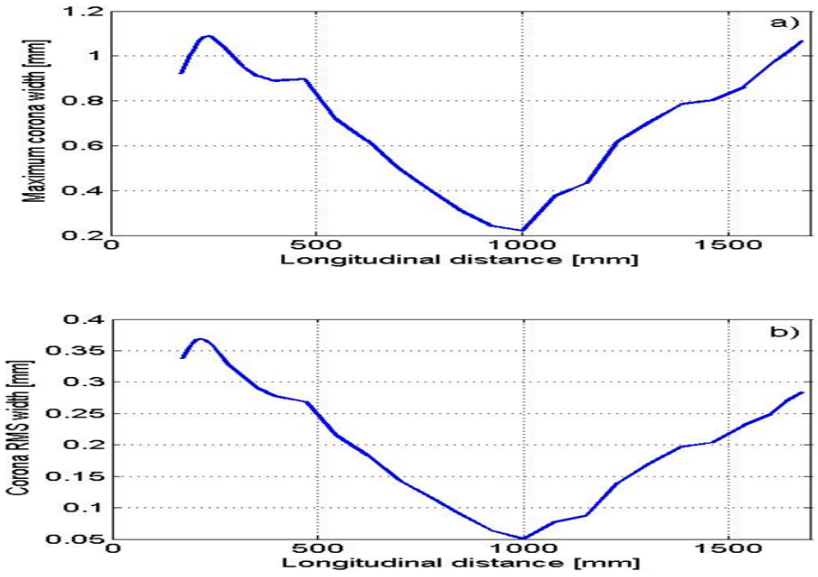

Figure 3.9: Average corona thickness vs z.

Chapter 4

High Voltage Power Supply and Modulator

4.1 Introduction

Most of the previously discussed beam performances depend on the quality of the pulsed high voltage and high precision power supply, whose preliminary design characteristics are discussed in the following.

The desired characteristics are summarized below

- ⋆ output voltage: up to *700 kV*
- ⋆ variable pulse length: *5-50 μs*
- ⋆ overshoot: $<$ *2%*
- ⋆ rise time: $<$ *1 μs*
- ⋆ voltage drop - ripple - stability: $<$ *0.1%*

The preliminary design consists of four main parts:

1. AC/DC converter with transformer;
2. IGBT-based DC/DC pulse modulator with output voltage of *4 kV*;
3. Multi-primary pulse transformer with *8* primary windings and one *700 kV* secondary winding.
4. Pulse Width Modulation (PWM) PID-based control system, optimized to follow very fast pulses.

As the voltage of the DC/DC modulator capacitance reaches a fixed threshold value, the control system starts to modulate. A MATLAB/Simulink model was predisposed in order to identify the best system layout, configuration and parameters with respect to pulse transformer and modulator. The simulations show that the designed power supply is able to satisfy technical specifications and requirements.

4.2 Requirements of CARM HVPS

The main technical requirements are summarized in the following Table 4.1.

Table 4.1: Characteristics of the CARM HVPS

Characteristic	**CARM HVPS**
Output Voltage	$500 - 700\ kV$
Load Resistance	Range 23.33 $k\Omega$ and 35 $k\Omega$ ($20\ A < I_{max} < 30\ A$)
Pulse Length	Variable Pulse Length 5 μs up to 50 μs
Repetition Frequency	minimum 1 Hz at 50 μs
Voltage Var. at Flattop	< 0.1 % (700 V)
Overshoot	< 2 %
Rise-Time	$< 1\ \mu s$
Energy into arc	$< 10\ J$ (for arc voltage = 100 V)
Pulse to Pulse stability	< 0.1 %
Ripple	< 0.1 %

4.3 Design of CARM HVPS

To answer to these requirements, the CARM HVPS is composed by the following subsystems:

1. Transformer HV/LV;
2. AC/DC converter diode/thyristor bridge rectifier;
3. DC/DC pulse modulator;
4. pulse transformer output voltage *700 kV*;
5. pulse width modulation (PWM) digital control system.

The conceptual design of CARM HVPS is based on the Matlab simulation scheme given in Fig. 4.1.

The main pulse transformer parameters come from scientific literature and IEEE Standards, with a pulse lenght up to 50 μs. The pulse modulator circuit configuration Matlab simulations show high flexibility related both to pulse magnitude and duration, fast dynamic response and high precision. The PID PWM controller parameters simulations show a high stability.

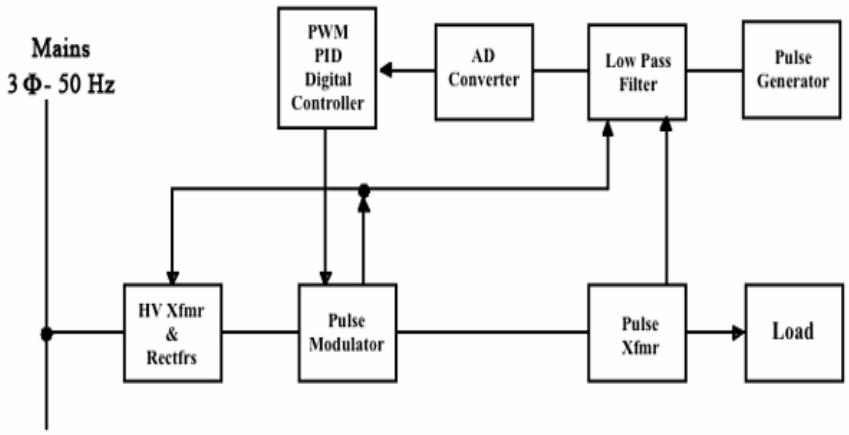

Figure 4.1: Simulink model reference scheme of CARM HVPS.

4.4 Pulse Transformer Design

The pulse transformer parameters were determined according to scientific literature and IEEE standards, considering a pulse width up to *50* μs.

Some definitions are reported as follows:

1. t_r : *rise time*, the time interval of the leading edge between the instants at which the instantaneous value first reaches the specified lower and upper limits of *10%* and *90%* of V_{max};

2. ΔV_{max} : *overshoot*, the amount by which the first maximum occurring in the pulse-top region exceeds the straight-line segment fitted to the top of the pulse;

3. ΔS_{max} : *tilt* (droop), the difference between V_{max} and the value at the end of pulse flat top, expressed in amplitude units or in percentage of V_{max};

4. C_D : *distributed capacitance*;

5. L_σ : *leakage inductance*;

6. L_m : *magnetizing inductance*;

7. n: *transformer ratio.*

According to IEEE standards, the equivalent circuit of pulse transformers [12] is shown in Fig. 4.3a. In order to simplify the analysis of the transient behaviour for operation with rectangular pulse voltages, if n>>1 the standard equivalent circuit can be reduced to the equivalent circuit shown in Fig. 4.3b during the leading edge.

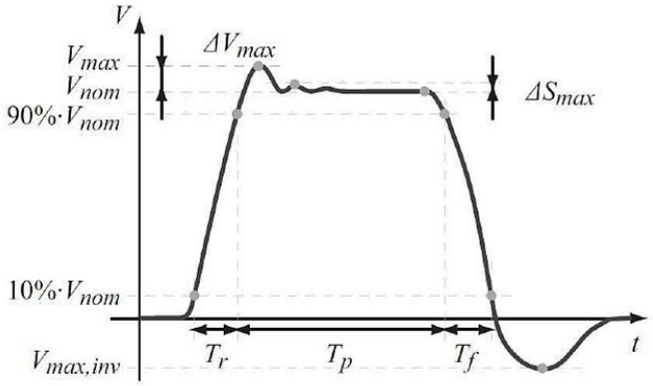

Figure 4.2: Typical pulsed waveform.

In order to satisfy the design specification, the rise time and the overshoot are achieved as follows:

$$t_r = 2\pi \; T_{10\%-90\%} \cdot \sqrt{L_\sigma C_d} \leq 1\mu s \tag{4.1}$$

and

$$\Delta V_{\max} = 2R_{load}\sigma = \sqrt{\frac{L_\sigma}{C_d}} \leq 2\% \tag{4.2}$$

Where $T_{10\%-90\%}$ depends on the selected damping coefficient σ and equals the time in which the voltage $V_{load}(t)$ rises from *10%* to *90%* [13] and [14]. Considering a damping coefficient $\sigma = 0.8$ and a normalized rise time $T_{10\%-90\%} = 0.392$ (Fig. 4.5), the distributed capacitance and the leakage inductance values are:

$$\begin{aligned} L_\sigma &\leq 1.95 \; mH, \\ C_d &\leq 84.58 \; pF \end{aligned} \tag{4.3}$$

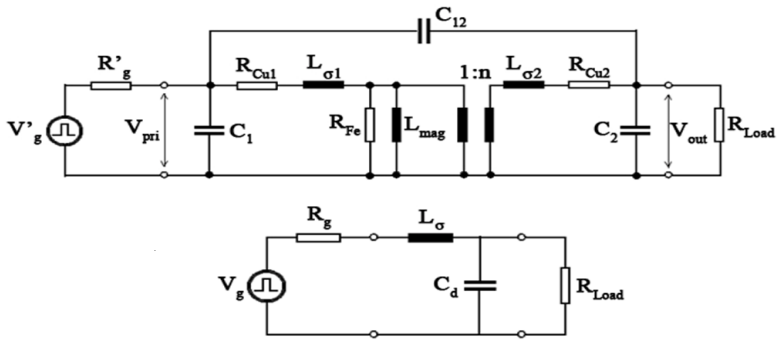

Figure 4.3: Equivalent pulse transformer scheme and reduced equivalent scheme during leading edge.

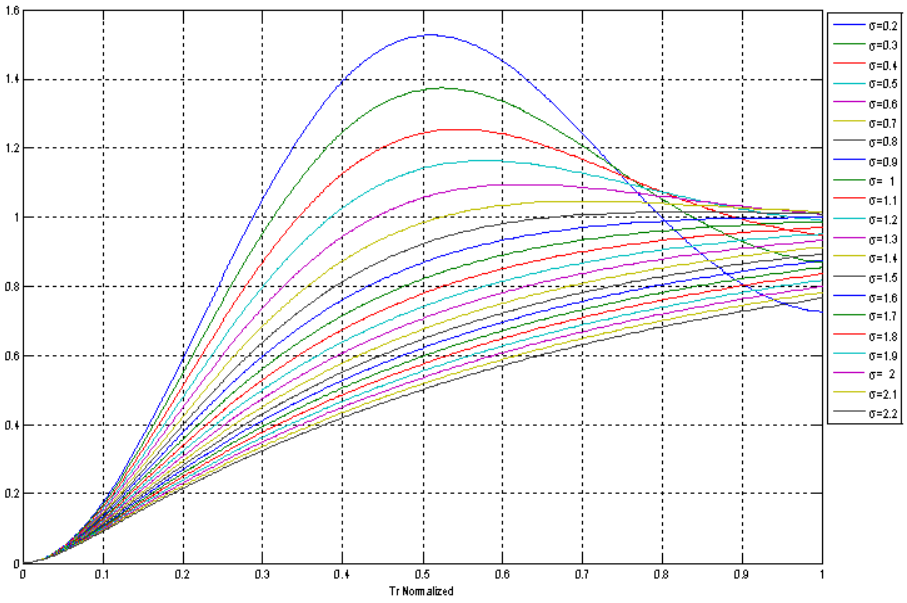

Figure 4.4: Transient behavior of the normalized output voltage for different damping coefficients σ.

The magnetizing inductance L_m is achieved imposing tilt $\Delta S_{max} \leq 0.1\%$ during flat top pulse.

$$\frac{Rt_p}{L_m} \leq 0.1\% \tag{4.4}$$

is the equivalent parallel resistance referred to the primary, therefore

$$L_m \geq 0.13\ H \tag{4.5}$$

In the Simulink model, the pulse transformer is made of eight separated pulse transformers with separated primary windings and one only secondary winding connected in series. This solution has been simulated through MATLAB code connecting in series the secondary windings of eight pulse power transformers and using the parameters previously set up. The simulation model was devoted to verify that pulse transformers parameters satisfy the design specifications.

4.5 Pulse Modulator Design

The pulse modulator circuit configuration in Fig. 4.6 allows to reach high pulse magnitude and duration, flexibility, fast dynamic response and high precision, within the design specifications. The Pulse Modulator is implemented by a multistage DC/DC converter based on IGBT and buck topology.

On the rising edge of the gate drive signal the fast IGBT is turned on, the inductor current slope is constant and it can be expressed by

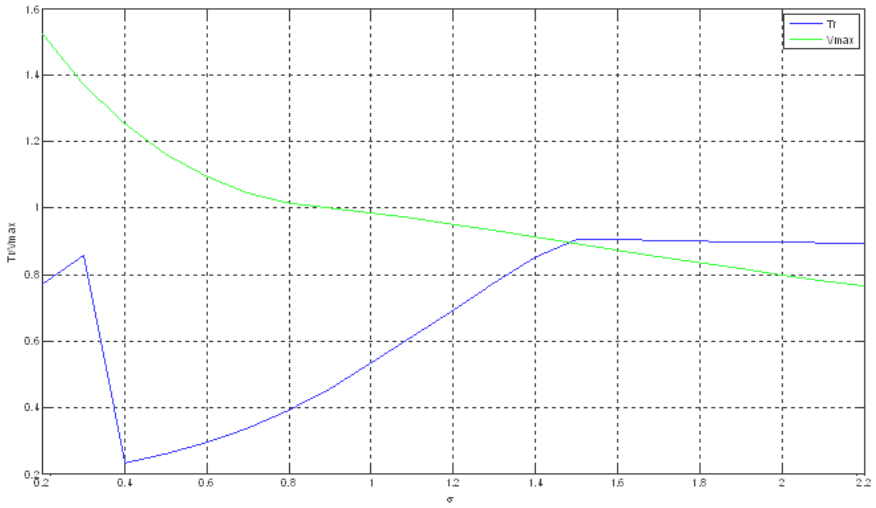

Figure 4.5: Normalized rise time and normalized output voltage in term of the damping coefficients σ.

$$S_{on} = \frac{V_{in} - V_{out}}{L} \tag{4.6}$$

Whereas on the falling edge of the gate drive signal the fast IGBT is turned off, the slope of the inductor current is given by

$$S_{on} = \frac{-V_{out}}{L} \tag{4.7}$$

The inductor current ripple can be expressed by

$$\Delta I_L = \frac{V_{in}\,(1-D)\,D}{L} T \tag{4.8}$$

where D is the duty cycle and T the switching period; whereas the voltage ripple across output capacitance is given by

$$\Delta V = \frac{q}{C} = \frac{\Delta I_L T}{8C} \tag{4.9}$$

Increasing the output capacitance value and/or the frequency of switching improves the output voltage regulation. To protect the RF source, the energy into an internal fault must be limited to less than 10 J. Typical achievable values are around four joules. The energy stored easily exceeds this value, therefore a high-speed SCR crowbar shall be located downstream of the filter to limit the energy dissipated into the CARM RF source if the CARM RF source has an internal fault.

4.6 PID Digital Controller Design

The PID PWM digital controller parameters set up shows high stability. The control algorithm strategy and block diagram is shown in Fig. 4.7.

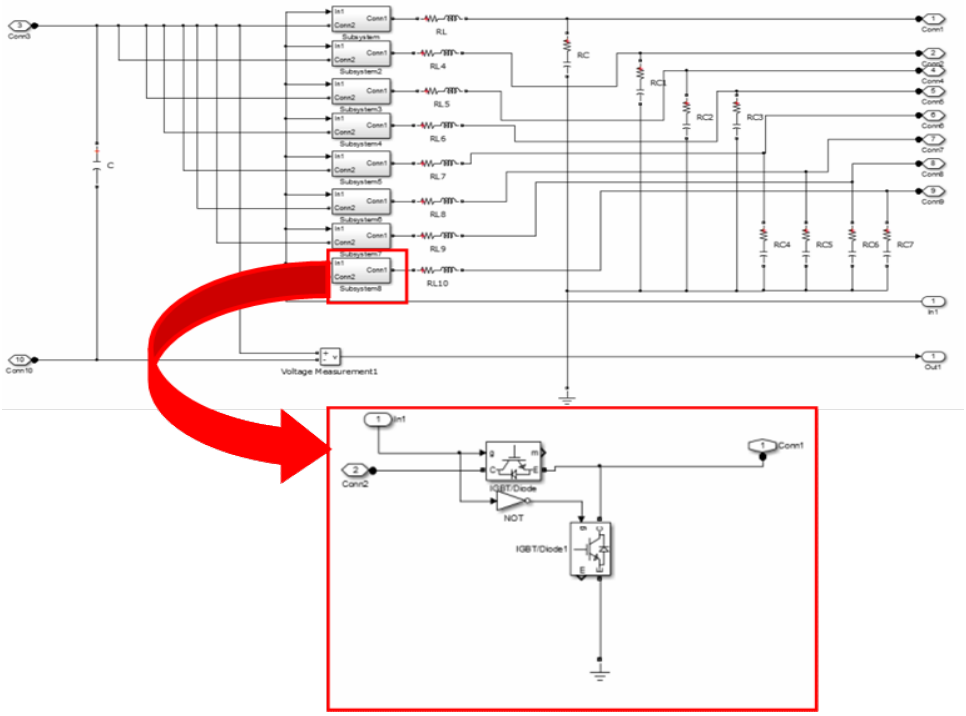

Figure 4.6: The circuital scheme of Pulse Modulator.

The digital controller is PID based with anti-windup, able to follow so fast rectangular pulsed waveforms sample frequency $f_s = 1\ GHz$ (sample time $T_s = 1 \cdot 10^{-9} s$). The control system starts the modulation when the voltage on the capacitance of 8 DC/DC pulse modulators reaches a fixed threshold $V_{thr} = 4\ kV$. On the closed control loop, there is a signals processing system composed by an analogical low-pass filter and an analogical/digital converter.

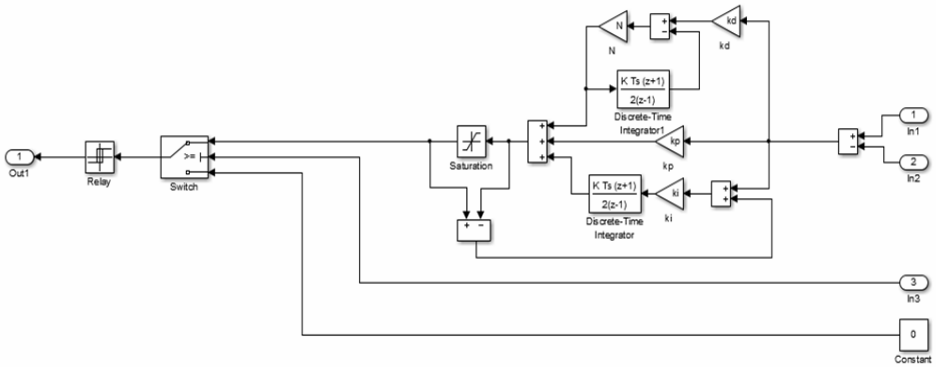

Figure 4.7: PID PWM digital controller block diagram.

4.7 Transformer and AC/DC converter

The Pulse modulator is powered by a converter transformer and a thyristor/diode converter as shown in Fig. 4.8. The thyristor AC/DC converter is need to charge the input capacitance of Pulse Modulator. In order to reduce the peak of current absorbed during the charge transient of capacitor of the Pulse Modulator, a voltage controller is implemented reproducing a output ramp voltage and hence an almost constant absorbed current.

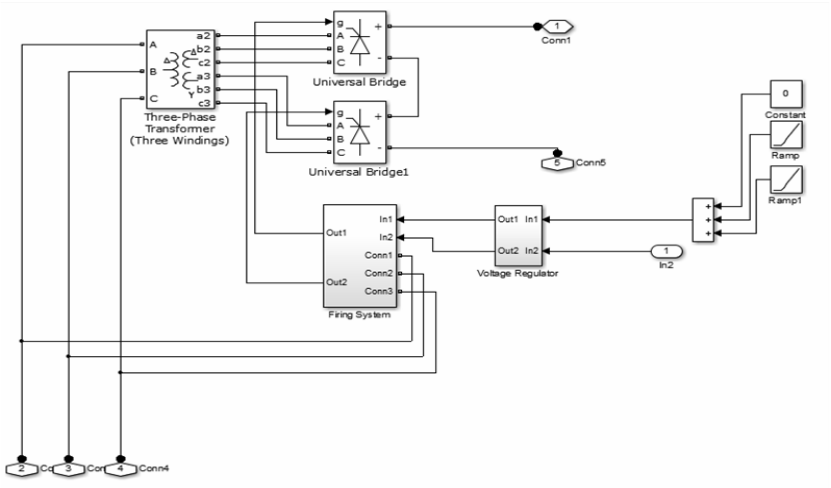

Figure 4.8: Transformer and AC/DC converter.

4.8 Simulation results

A set of simulations were carried out in order to validate the design choices made. The simulations parameter values are shown in Table 4.2. The simulation outcomes are reported as follows:

- ⋆ Output voltage of CARM HVPS;
- ⋆ IGBT currents of pulse modulator;
- ⋆ IGBT voltages of pulse modulator;
- ⋆ Output voltage of pulse modulator (Figs. 4.9a-4.11c).

The pulse modulator circuit configuration given above shows high flexibility about pulse magnitude / length, fast dynamic response and high precision within the design specifications.

Finally, with our choice for the PID PWM controller parameters set up, the system itself has a shown high output stability.

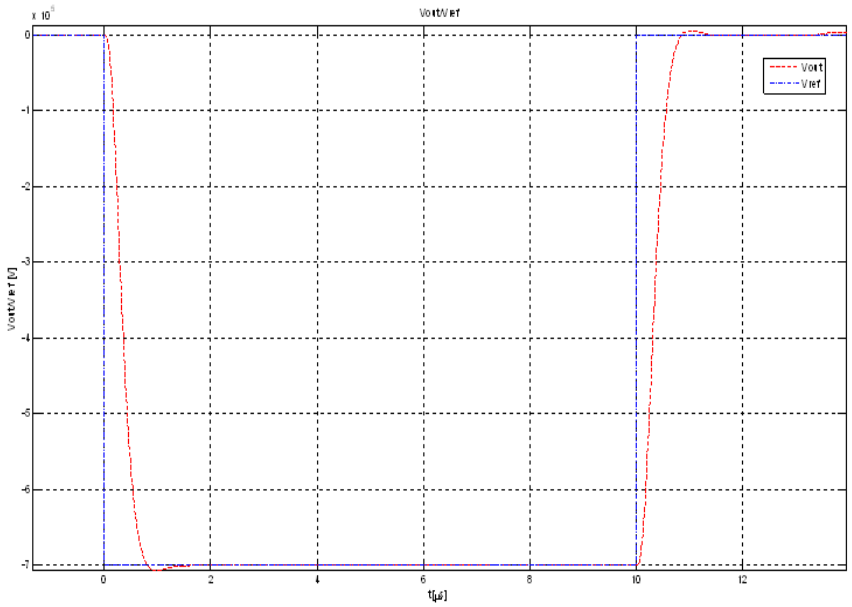

(a) Output voltage of CARM HVPS pulse length *10 μs*.

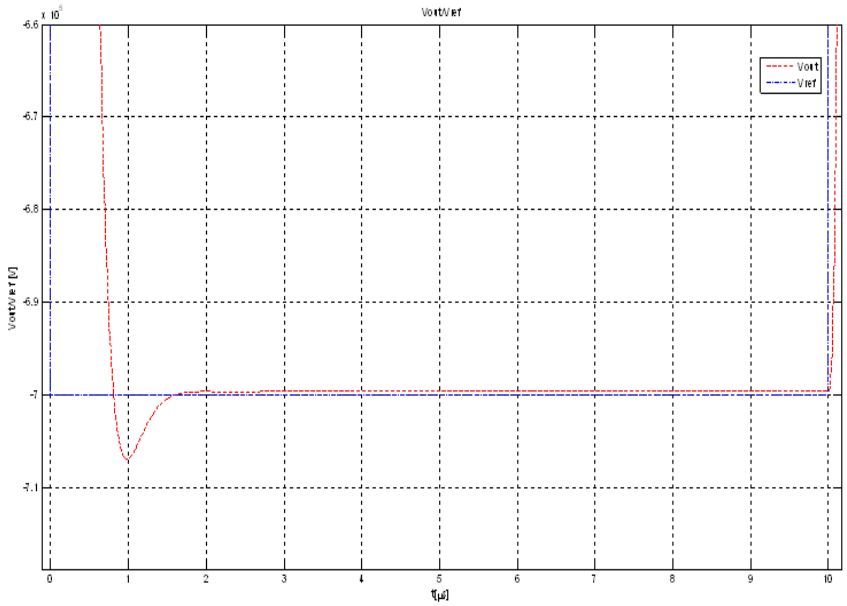

(b) Zooming output voltage of CARM HVPS pulse length *10 μs*.

Figure 4.9: Output voltage of pulse modulator.

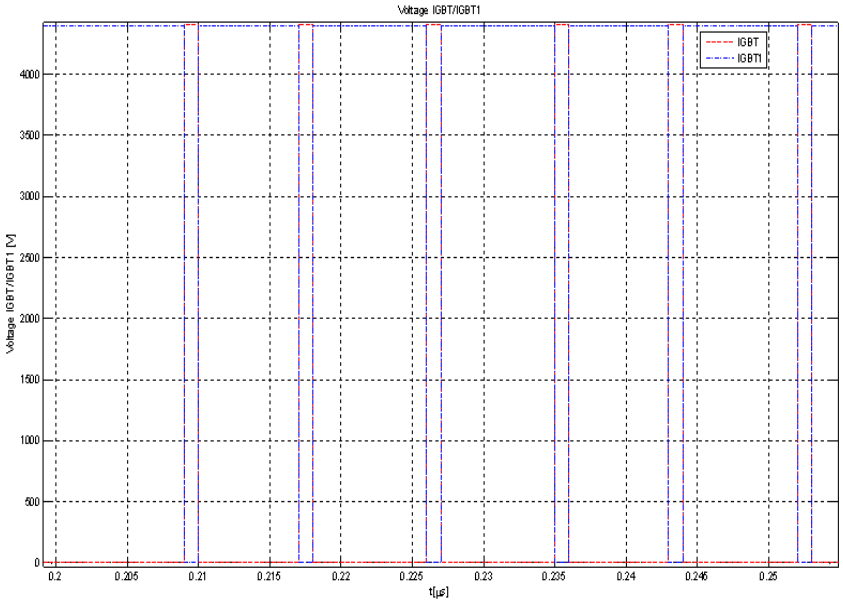

(a) IGBT voltages of pulse modulator.

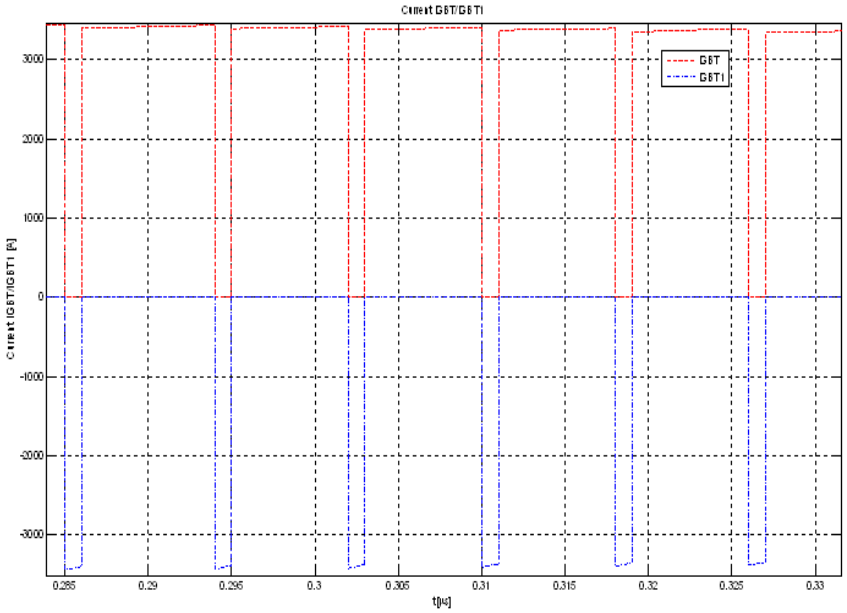

(b) IGBT currents of pulse modulator.

Figure 4.10: Output currents of pulse modulator.

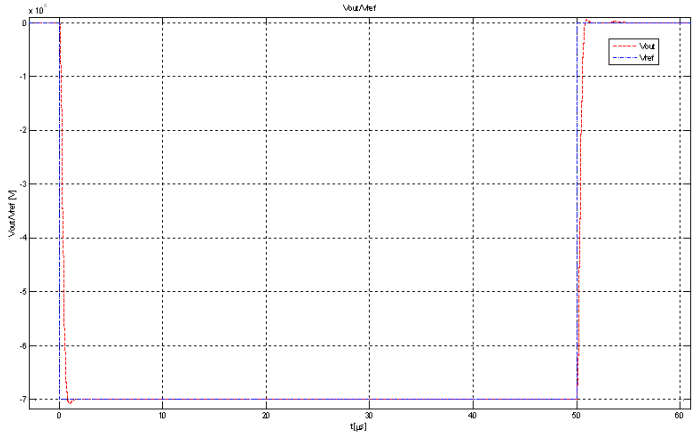

(a) Output voltage of CARM HVPS pulse length *50 μs*.

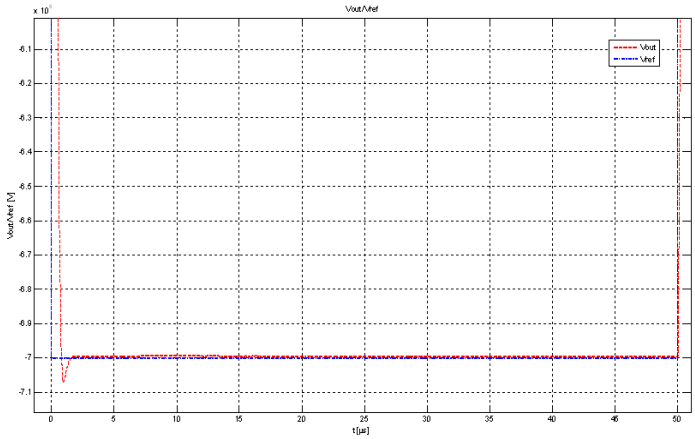

(b) Zooming output voltage of CARM HVPS pulse length *50 μs*.

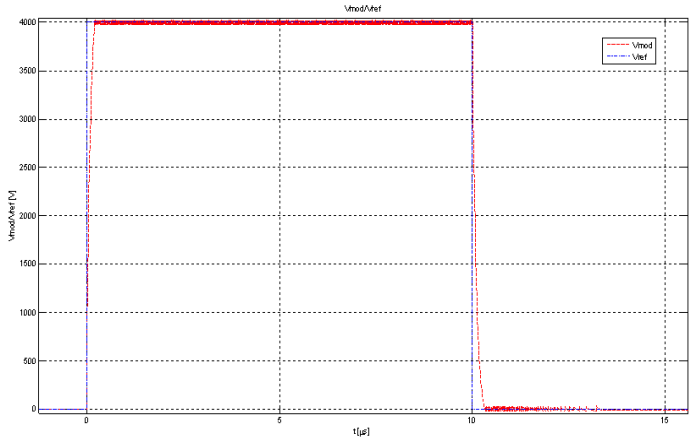

(c) Output voltage of Pulse Modulator

Figure 4.11: Output currents of pulse modulator.

Table 4.2: **Parameters for simulations**

Parameter	Value
Pre-charged input capacitance	$C_{in} = 120\ mF,\ V = 4\ kV$
Output capacitance value	$C_{out} = 1\ \mu F$
Inductance value	$L = 0.1\ \mu H$
Resistor value of inductor	$R_L = 1\ m\Omega$
Resistor value of capacitor	$R_c = 1.1\ \Omega$
Proportional action	$k_p = 10$
Integral action	$k_i = 0.01$
Derivative action	$k_d = 1 \cdot 10^{-6}$
Sample time	$T_s = 1 \cdot 10^{-9}\ s$
Distributed capacitance	$C_d = 33.83\ pF$
Leakage inductance	$L_\sigma = 0.78\ mH$
Magnetizing inductance	$L_m = 10\ H$
Windings resistance	$R_{sc} = 0.5\ m\Omega$
Core resistance	$R_c = 1\ M\Omega$
Transformer ratio	$V_1/V_{20} = 4\ kV/87.5kV$
1/ transformer ratio	$1/n = 21.875$

Chapter 5

Microwave Components

5.1 General Considerations

The design of the CARM oscillator source foresees the use of a resonant cavity delimited by Bragg reflectors. It is realized by a straight cylindrical wave-guide section with rippled wall reflectors at both ends, according to sketch reported in Fig. 5.1.

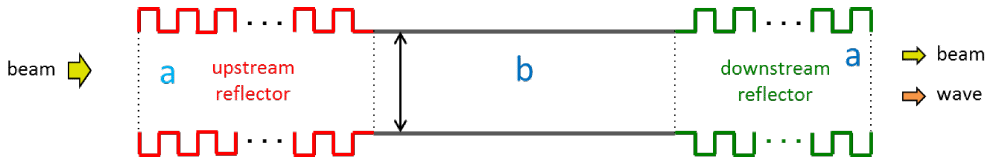

Figure 5.1: CARM cavity and Bragg reflectors: *a*) Rippled sections; *b*) Straight cylindrical wave guide.

This configuration allows the passage of an intense electron beam and, at the same time, ensures a high diffractive *Q-factor*. Just to give an idea of how such a configuration contributes to the transmission of a signal at a given frequency, we provide below a very preliminary discussion.

The ripples are mathematically reproduced by any periodic wall modulation of the inner cavity radius as e.g.

$$R(z) = R_0 \left(1 + \delta_R \cos\left(k_b z + \phi_b\right)\right) \tag{5.1}$$

with $k_b = \dfrac{2\pi}{\Lambda_b}$ where Λ_b and ϕ_b are the periodicity and the phase of the wall corrugation respectively.

The condition for a Bragg constructive interference is

$$\begin{aligned} \lambda_g &= 2\Lambda_b, \\ \lambda_g &= \frac{2\pi}{k_z} \end{aligned} \tag{5.2}$$

by exploiting the equations of Ch. I, accounting for the CARM resonance condition, we find

$$\Lambda_b = \pi \frac{v_p}{\omega_R} \cong \frac{\beta_p}{2} \left(\frac{\Lambda}{2\gamma_z^2} \right) \tag{5.3}$$

where ω_R denotes the CARM resonant angular frequency, thus finding, for our design, a corrugation period around *600 μm*.

The depth of the ripple can be determined by noting that it should satisfy at least two conditions:

$$\begin{aligned} r_b &\ll 2R_0 - \lambda_R, \\ r_b &\ll \frac{\lambda_R}{2\pi} \end{aligned} \tag{5.4}$$

(where $\lambda_R = \dfrac{2\pi c}{\omega_R}$ is the CARM resonant wave length) imposed by the necessity of avoiding effects associated with slit and single body diffraction effects.

The radius R_0 of the cylindrical cavity can be specified by determining the threshold power density $\bar{P}_{Th}$ allowed by the structure. If we denote the power density inside the optical cavity as

$$\begin{aligned} \bar{P}_I &= \frac{P_I}{S}, \\ S &= \pi R_0^2 \end{aligned} \tag{5.5}$$

and impose the condition $\bar{P}_I = \bar{P}_{Th}$ we obtain

$$R_0 = \sqrt{\frac{1}{\pi} \frac{P_I}{\bar{P}_{Th}}} \tag{5.6}$$

If *1 - 2 MW* is the intra-cavity power P_I and $\bar{P}_{Th} \cong$ *566* $\dfrac{kW}{cm^2}$, given by the copper breakdown condition, we find $R_0 \cong$ *7.5 - 10 mm*.

The ripple amplitude derived from eqs. (5.4) is accordingly given by $r_b \ll$ *200 μm*.

The Q-factor of a resonator with the previous characteristics can be determined using the following approximate formula given by Bratman [10]

$$Q \cong \frac{k^2 L}{k_z \left(1 - \sqrt{R_+ R_-}\right)} \tag{5.7}$$

with $k = \dfrac{\omega}{c}$ the vacuum wavenumber, furthermore kz is the longitudinal wavenumber of the working mode, L is the length of the central section of

the resonator, and R_+ and R_- are the reflectivities (in power) of the upstream and downstream reflectors respectively.

To be more specific we note that for the modes TE_{82} and TE_{53} at *250 GHz* ($k = 5239.6\ m^{-1}$) in a circular waveguide with radius of *7.5 mm* have k_z of *4889.9* m^{-1} and *4896.5* m^{-1} respectively.

To take into account the energy stored in the reflectors by the exponentially decaying fields, some authors [11] replace L with the following effective length

$$L_{eff} = L + \frac{1 - e^{-G_+ L_+}}{G_+} + \frac{1 - e^{-G_- L_-}}{G_-} \tag{5.8}$$

with L_+ and L_- being the length of the upstream and downstream mirror, and G_+ and G_- the coupling coeffients between forward and reflected waves in the two reflectors as reported in the Technical Addendum E.

5.2 The Resonant Cavity and Bragg Reflectors

We have already pointed out that the role of the Bragg reflector is that of playing the role of mirrors delimiting the cavity resonator. The preliminary design of the Bragg reflectors has been done using the coupled-mode theory: an approximate method suitable for non-uniform waveguides with cross-section variations significantly smaller than the vacuum wavelength. The large electrical size of the present cylindrical cavity indeed prevents from adopting volumetric or integrals solvers, typical of commercially available CAD tools.

The resonant cavity consists of an upstream Bragg reflector, a smooth-wall section waveguide and a downstream Bragg reflector. The geometry of a distributed Bragg mirror in circular waveguides is shown in Fig. 5.2 and is defined through the following five parameters:

- Unperturbed radius R_0;
- Ripple period Λ_b;
- Ripple amplitude rb;
- Number of ripple periods;
- Ripple profile.

To properly frame the modelling procedure the following considerations are necessary.

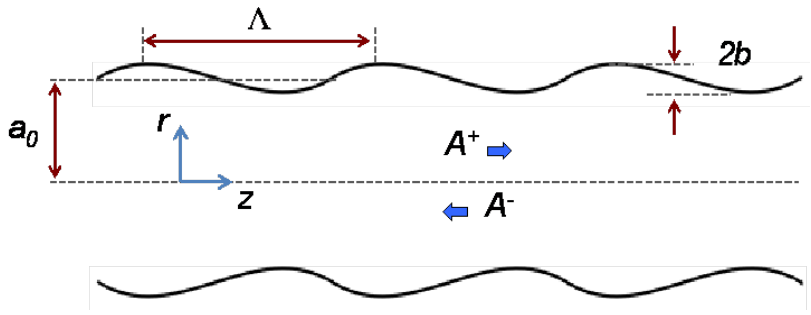

Figure 5.2: Parameters of a rippled wall circular waveguide.

i Deeper corrugations correspond to higher coupling between modes. When increasing the ripple amplitude, the reflectivity initially enhances and then deteriorates because the inter-coupling with the closest mode becomes so strong to induce coupling between modes. In the present application, suitable ripple amplitudes are in the range $10 \div 50\ \mu m$.

ii The further the cut-off frequency of the working mode is *far* from the operational frequency, the worse the reflectivity for a given mirror length. In other words, for fixed frequency and number of ripples, higher-order modes work better than lower-order modes.

iii The longer the device, the narrower the bandwidth. This is a well-known feature of Bragg reflectors.

iv The attenuation constants of TE_{nm} modes increase with the azimuthal index n, while, assuming $n \neq 0$, they exhibit a minimum for a radial index $m = 3$.

In the ENEA CARM proposal, the cut-off frequency of the working mode has to be in the range *80-100* GHz to take full advantage of the relativistic wave-particle resonance condition. Moreover modes with radial index $m = 2$ must be preferred because of the radial position of their maximum amplitude. This choice realizes a compromise between conflicting needs: annular electron beams with higher radius can fulfil more easily the required quality, whereas ohmic losses decrease using $m = 3$ or 4.

In this framework the TE_{82}, with cut-off frequency of *89.8* GHz, maximum amplitude at a radius of *4.85* mm and attenuation constant of *0.26* dB/m, appears the most suitable choice. A cavity has been thus designed with a quality factor around *4000* at a resonant frequency of *258.1* GHz; the latter values have been chosen, according to the expected parameters of the electron beam, for maximizing the efficiency, while keeping acceptable power dissipation at the cavity walls. Copper with standard conductivity ($\sigma = 5.8 \cdot 10^7$) is assumed as material.

The reflectors have sinusoidal ripples with a period of *619.5 μm* and a depth of *20 μm*. Reflectivity of *93.6%* and *15%* is respectively achieved with *700* and *120* corrugations for the up and down-stream mirror, resulting in a total length of *434* and *74 mm* respectively; the plots versus frequency are shown in Fig. 5.3. The length of the smooth-wall section has been set to *180.59 mm*, a value that gives the desired quality factor and finely tunes the resonance at *258.1 GHz*. The behaviour of the resonator is given in Fig. 5.4 for an input signal injected from the downstream mirror. The computed Q-factor for diffractive losses is *3986* and the ohmic losses are *1.4%* of the input power. The approximate formula given by Bratman gives $Q = 1672$, because it neglects the energy stored inside the reflectors by evanescent modes. The use of the Mc Cowan's formula, which instead takes into account such contribution, gives $Q = 3773$. Other propagating modes, intersecting the beam line in the Brillouin diagram very close to their cut-off frequency, exhibit even higher Q-factor, but they are mostly dissipated owing to ***Ohmic*** attenuation.

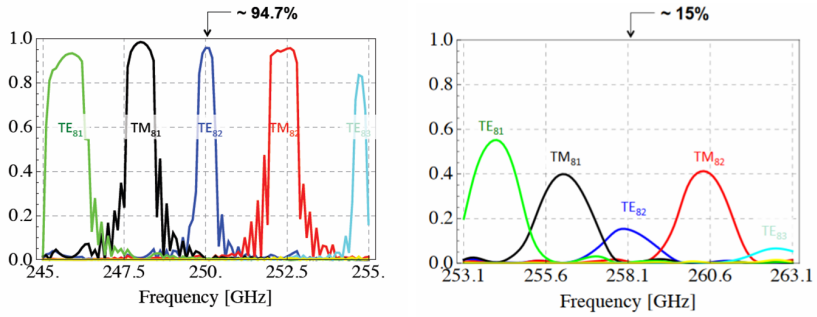

Figure 5.3: Mirror reflectivity vs. frequency.

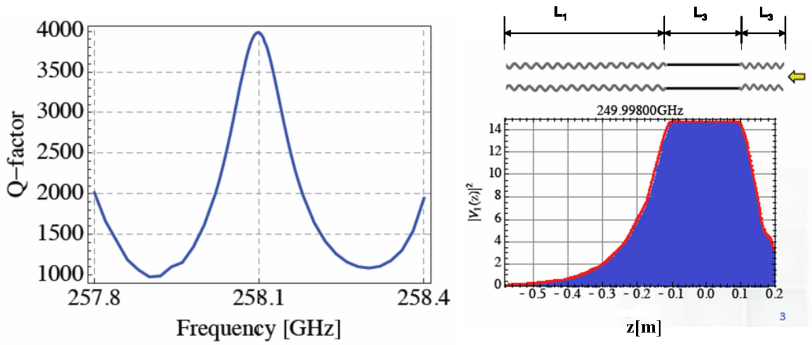

Figure 5.4: Q-factor (left) and E-field amplitude profile (right).

Given a set of modes with the same azimuthal index, previous results demonstrated the effectiveness of a Bragg resonator in selecting the working mode. Different countermeasures have to be taken against modes with the same radial index of the working one, e.g., limiting the amplitude of the

TE_{72} and TE_{92} mode. A first method to reduce this kind of mode competition consists in using rectangular slots equally spaced along the sidewall of the cylindrical cavity.

A slotted cavity allows

- ⋆ Selecting a linear polarization of the operational mode;
- ⋆ Impairing TE modes with low starting current;
- ⋆ Creating vacuum inside the cavity.

In our case the number of slots corresponds to the azimuthal order of the operating mode. Hence there must be eight longitudinal slots rotated of 45 degree and placed along the longitudinal lines where the amplitude of the TE_{82} electric field at the cavity walls is minimum. The position of the slots must be consistent with the linear polarization of the TE_{82} otherwise the operating mode will be affected too. Some simulations with CST Microwave Studio have been executed in the frequency range over the cut-off (*100-120* GHz) to demonstrate the effectiveness of the method in suppressing TE_{m2} modes with m close to eight.

Results are shown in Figs 5.5 and 5.6, where the propagation of some modes along a cylindrical waveguide with length of *60 mm* and radius of *7.5 mm* has been studied. The waveguide is provided with *8* longitudinal rectangular slots having cross-section of 50×0.2 *mm* and length of *50 mm*. In Fig. 5.5 the pattern of the electric field is depicted for a linearly polarized TE_{82} mode considering for two different positions of the slots. In Fig. 5.6 the propagation of the TE_{72} and TE_{92} modes are taken into consideration together with the TE_{82} mode. The S_{21} parameters are plotted, showing a clear insertion loss of the TE_{72} and TE_{92} modes.

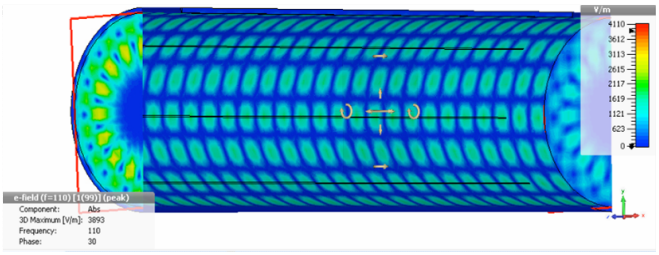

(a) e-Field cavity *110 GHz*.

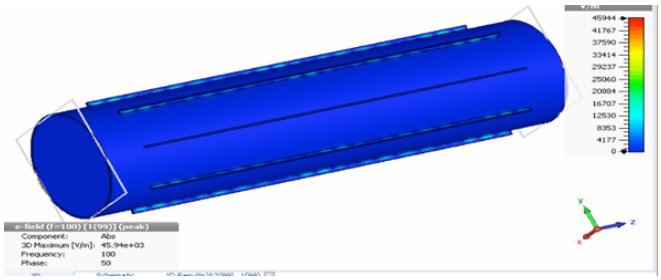

(b) e-Field cavity slots *12.5*.

Figure 5.5: Propagation of the TE_{82} mode at *110 GHz* when slot centres correspond to the minimum (top) and maximum (bottom) of the unperturbed electric field pattern. In the latter case slots are rotated by *11.25 deg* and the mode is destroyed.

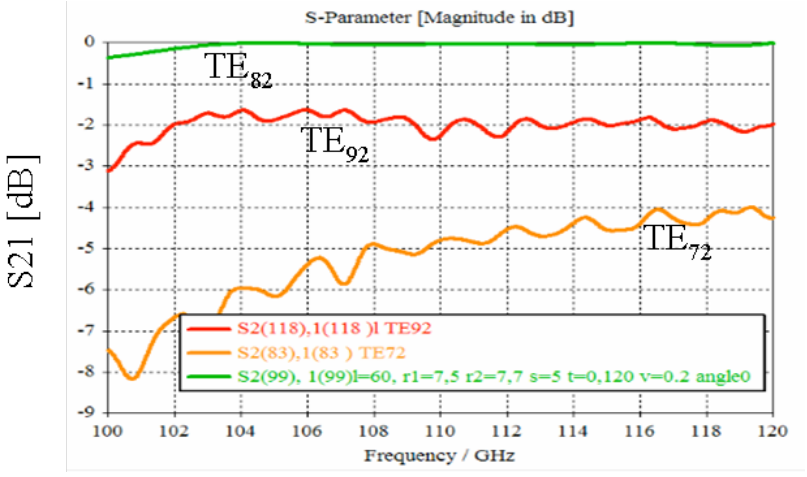

Figure 5.6: At the output port the power levels of the TE_{72} and the TE_{92} at *f=120 GHz* are *-4 dB* and *-2 dB*, respectively, while the transmission of the TE_{82} mode is almost unaffected.

Technical Addenda

In this part of the report we expand and clarify the design details left open in the previous discussion, devoted to the description of the main components of the device itself.

The addenda will cover either construction and cost issues, in particular we will review the design of magnets (cathode coils, superconducting magnet) and report on the details of the electron beam transport.

An accurate description of the cavity modeling will be reported along with the mode selection criteria. Technical issues regarding the vacuum details for the entire device are analyzed too. Finally we present logistic and cost analysis.

The Annexes are specified as “Technical Addendum”.

Technical Addendum A

GUN Solenoid Design

In this note we sketch the essential elements for the design of a finite solenoid for the CARM Plasma Heating (CPH) Frascati project.

We will follow a strategy based on the design of an air core solenoid and use an analytical procedure involving the Biot- Savart law [15].

We remind that for a solenoid with radius a and length L_s, the magnetic field is pointing vs. the axis direction. The on axis field (namely the component in the z - direction at the center of the solenoid) is indeed provided by an almost constant intensity with a smoothly decreasing fringing, starting near the external edge of the ending wires and extending outside the solenoid itself.

A.1 Biot-Savart law and the magnetic field distribution inside a solenoid

We will specify the full solenoid field map by employing the Biot Savart law and by solving the problem in different geometrical representations.

The method we develop is easily amenable for numerical implementation and for its use in the analysis of the evolution of the electron beam distribution, after the cathode emission, as we will show elsewhere.

We will employ a fairly straightforward procedure based on elementary geometrical means and allowing its extension to even more complicated geometries.

A.1.1 Cartesian Coordinates

In Fig. A.1 we have sketched the geometrical framework of the *Biot-Savart* law. The field element $d\vec{B}$ at $p \equiv (x_0, y_0, z_0)$ is generated by the

current I crossing the coil element $d\vec{h}$. The associated vector $\vec{h}$ is specified in terms of the geometrical nature of the wire and

$$\vec{r} = \vec{p} - \vec{h}, \tag{A.1}$$

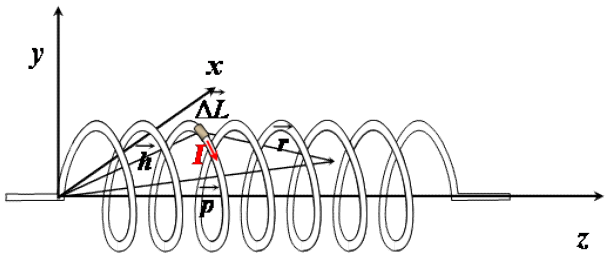

Figure A.1: The Biot-Savart geometry for a solenoid.

According to the previous notation we write

$$d\,\vec{B} = \frac{\mu_0 I}{4\,\pi}\frac{d\vec{h}\times\vec{r}}{|\vec{r}|^3} \tag{A.2}$$

The vector $\vec{h}$, along the helix of the solenoid, can be written in the parametric form

$$\begin{aligned} &\vec{h}(z) \equiv (a\cos(\Omega z), a\sin(\Omega\, z),\ z)\,, \\ &\Omega = 2\pi\frac{n}{L_s} \end{aligned} \tag{A.3}$$

where, again, L is the total length of the solenoid and n the number of coil turns.

For further convenience we recast eq. (A.2) as

$$\begin{aligned} &d\vec{B} = \frac{\mu_0 I}{4\,\pi}\frac{\vec{h}'(z)\times\vec{r}(z)}{|\vec{r}(z)|^3}dz, \\ &\vec{h}'(z) = \frac{d}{dz}\vec{h}(z) \end{aligned} \tag{A.4}$$

with $\vec{r}(z)$ vector provided by

$$\begin{aligned} &\vec{r}(z) = \vec{p} - \vec{h}(z), \\ &\vec{p} \equiv (x_0, y_0,\ z_0) \end{aligned} \tag{A.5}$$

With these assumptions we find that the field in a generic point of the space can be expressed via the integral

$$\vec{B}(x_0, y_0, z_0) = \frac{\mu_0 I}{4\pi} \int_0^{L_s} \frac{\vec{h}'(\zeta) \times \vec{r}(\zeta)}{|\vec{r}(\zeta)|^3} d\zeta \tag{A.6}$$

which can be easily computed.

The behavior of the field-vector components vs. the coordinates is summarized in Figs. A.2, they confirm the results of the analysis carried in the introductory section.

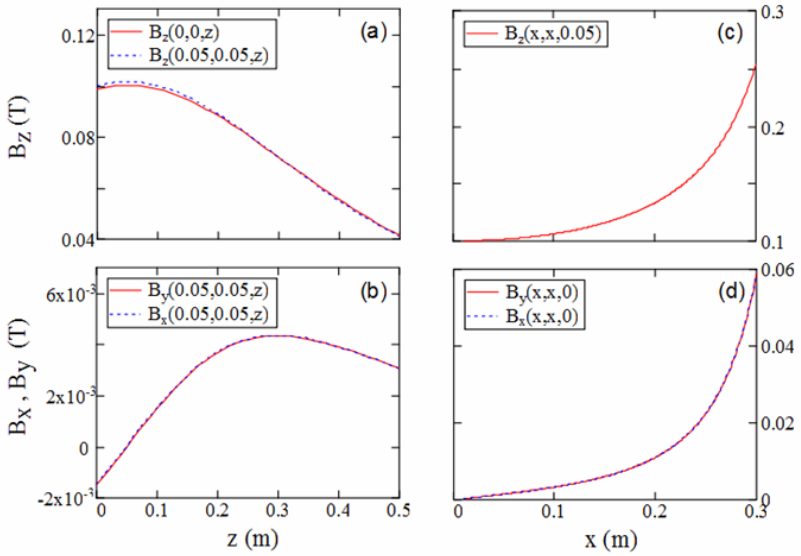

Figure A.2: Field components in the solenoid.

A.1.2 Cylindrical Coordinates

The previous field equations can be written in cylindrical coordinates. The vector potential is, indeed, written in the form [16]

$$A_\phi(z, r) = \frac{\mu_0 n I a}{2\,\pi} \int_0^{\pi} \left[\cos(\phi) \ln \left[\xi + \sqrt{\xi^2 + r^2 + a^2 - 2\,a\,r\cos(\phi)} \right] d\phi \right]_{\xi = z - \frac{L}{2}}^{\xi = z + \frac{L}{2}}$$
$$[A(\xi)]_a^b = A(b) - A(a) \tag{A.7}$$

By recalling that the vector potential and the magnetic field are linked by

$$\begin{aligned} B_r(z, r) &= -\frac{\partial}{\partial z} A_\phi(z, r), \\ B_z(z,\, r) &= \frac{1}{r} \frac{\partial}{\partial r} \left(r\, A_\phi(z,\, r) \right) \end{aligned} \tag{A.8}$$

The field components in polar coordinate can be written as

$$B_r(z,r) = -\frac{\mu_0 nIa}{2\,\pi\,L}\int_0^{\pi}\left[\frac{\cos(\phi)}{\sqrt{\xi^2+r^2+a^2-2\,a\,r\cos(\phi)}}d\phi\right]_{\xi=z-\frac{L}{2}}^{\xi=z+\frac{L}{2}},$$

$$B_z(z,r) = \frac{\mu_0 nIa}{2\,\pi\,L}\int_0^{\pi}\left[\frac{\xi(a-r\cos(\phi))}{\sqrt{\xi^2+r^2+a^2-2\,a\,r\cos(\phi)}(r^2+a^2-2\,a\,r\cos(\phi))}d\phi\right]_{\xi=z-\frac{L}{2}}^{\xi=z+\frac{L}{2}} \tag{A.9}$$

and the relevant distribution is finally given in Fig. A.3.

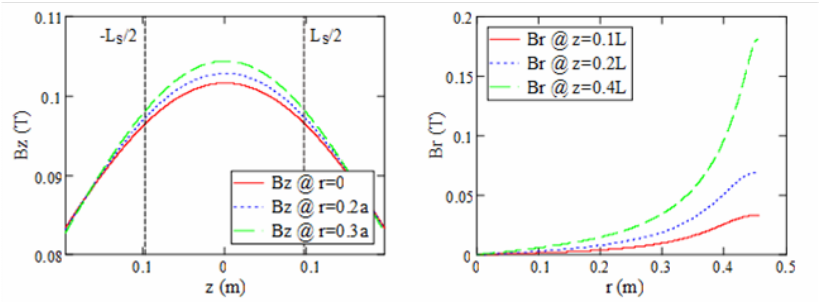

Figure A.3: Magnetic field in cylindrical coordinates. (a) longitudinal field at different distance r from axe (b) radial field at different position z along the solenoid axis; a is the internal radius, L is the solenoid length.

A.2 Definition of Operational Parameters

We can start to optimize the parameters from purely energetic considerations.

If we consider only the on-axis longitudinal field ($r = 0$), eq (A.9) gives [16]

$$B_z(z) = \frac{\mu_0 IN}{2L_s}\left[\frac{z+\frac{L_s}{2}}{\sqrt{a^2+\left(z+\frac{L_s}{2}\right)^2}} - \frac{z-\frac{L_s}{2}}{\sqrt{a^2+\left(z-\frac{L_s}{2}\right)^2}}\right] \tag{A.10}$$

So the on-axis magnetic field at the centre ($z = 0$) of the coil can be expressed as

$$B\left(\frac{L_s}{2}\right) = \frac{\mu_0 IN}{2L_s}\frac{\frac{L_s}{a}}{\sqrt{1+\left(\frac{L_s}{2a}\right)^2}} \tag{A.11}$$

By reversing eq. (A.11) we obtain for the current

$$I = \frac{2BL_s}{\mu_0 N} \frac{\sqrt{1 + \left(\frac{L_s}{2a}\right)^2}}{\frac{L_s}{a}}, \tag{A.12}$$

The ohmic power is accordingly

$$P_H = I^2 R = \frac{B^2}{\mu_0^2} \frac{4}{N^2} \left(\frac{\sqrt{1 + \left(\frac{L_s}{2a}\right)^2}}{\frac{L_s}{a}} \right)^2 R \tag{A.13}$$

where $R = \dfrac{2aN\rho}{r_c^2}$ is the ohmic resistance with r_c the radius of copper filament (assumed to be circular) and ρ the resistivity.

If we keep the magnetic field fixed, the quantity to be reduced is

$$\frac{\Gamma}{\rho} = \frac{4R}{N\rho} \left(\frac{\sqrt{1 + \left(\frac{L_s}{2a}\right)^2}}{\frac{L_s}{a}} \right)^2 = \frac{8a}{N} \frac{a^2}{r_c^2} \left[1 + \left(\frac{L_s}{2a}\right)^2 \right] \tag{A.14}$$

where $\Gamma = \dfrac{P_H \mu_0^2}{B^2}$. As example, if we increase the number of coils by a factor *5*, the length of the solenoid by a factor *3* and reduce $\dfrac{a}{r_c}$ by a factor *2* we achieve a reduction of the required ohmic power larger than a factor *15*.

The geometrical configuration of the machine give constrains on the geometry and dimensions of the solenoid. More in detail we have constrains on the internal radius that must be no smaller than *45 cm* and the length should be around *20 cm*, with an on-axis M-Field at the centre of *0.1 T*.

With this configuration the requested field is reachable by employing high current. Otherwise, as seen before, the number of coils can be increased. The coils have to be packed by distributing the turns over layers, allowing to reduce longitudinal dimension, but in this case a too large number of shells could give additional weight and the overall dimension of the device would be too cumbersome.

What we discussed in previous section, about the magnetic field profile, is valid for a finite thin solenoid where only one radius can be considered for all turns. If we take into account a thick solenoid with several shells, an internal radius a and an external one b can be defined and so the magnetic field equation (A.10) must be revised. For this purpose we can subdivide the thickness of the solenoid in so many infinitesimal concentric cylindrical

shells, of radius a_s generic between a and b. The magnetic field for this solenoid is [17]

$$B(z,a,b) = \frac{\mu_0 IN}{2L_s(b-a)} \cdot$$
$$\cdot \left[\left(z+\frac{L_s}{2}\right) \ln \frac{b+\sqrt{b^2+\left(z+\frac{L_s}{2}\right)^2}}{a+\sqrt{a^2+\left(z+\frac{L_s}{2}\right)^2}} - \left(z-\frac{L_s}{2}\right) \ln \frac{b+\sqrt{b^2+\left(z-\frac{L_s}{2}\right)^2}}{a+\sqrt{a^2+\left(z-\frac{L_s}{2}\right)^2}} \right] \tag{A.15}$$

We can do a simplest approximation by considering finite thickness for different shells with radius a_n discretely variating. In this case the effective M-Field for the solenoid can be evaluate only by summing the contribute of each assuming for each one the effective radius a_n of the $n-th$ shell.

$$B(z) = \sum_{n=0}^{n_s} \frac{mu_0 IN_s}{2L_s} \left[\frac{z+\frac{L_s}{2}}{\sqrt{a_n^2+\left(z+\frac{L_s}{2}\right)^2}} - \frac{z-\frac{L_s}{2}}{\sqrt{a_n^2+\left(z-\frac{L_s}{2}\right)^2}} \right] \tag{A.16}$$

where n_s and N_s are respectively the number of shells and the number of coils for shell.

This latter approximation can be useful in a real application where the wire has a finite section with a large diameter in order to reduce the ohmic resistance.

The longitudinal on-axis profile for the M-Field is shown in Fig. A.4.

A reasonable configuration for the solenoid is given by the optimized parameters given in Tab. A.1.

A.3 Electrical Supply Consideration and Operation Costs

With parameters defined in Tab. A.1 we can lead some consideration about the power supply.

We can better assume a square section φ^2 for the wire since this allows a lower resistance in the same effective size of the device. Assuming that the wire is made of a copper[1] filament with an effective[2] circular section (S) of *8 mm* Assuming a copper wire for the coils, we have for the resistance

[1]The copper resistivity is $\rho = 1.68 \cdot 10^{-8} \Omega \cdot m$

[2]The effective section takes into account the presence of the hole for the cooling flow inside the wire since in this case we should have an hollow conductor.

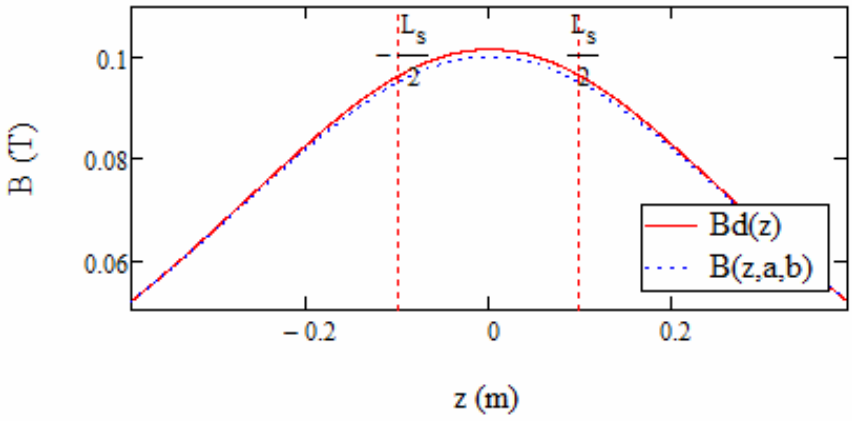

Figure A.4: Longitudinal on-axis profile for the magnetic field of thick solenoid with internal and external radius. A comparison for shapes calculated by using eq. (A.15) (blue dotted line) and eq. (A.16) (red continuous line) is shown. The two curve give a difference of *1%* for the maximum value of the field intensity B (calculated at the centre of the solenoid for $z = 0$).

R (assumed to be only of ohmic kind) $R = 43\ m\Omega$ and an inductance $L = \dfrac{\pi\mu_0\, a^2 N^2}{L_s}$ of the order of $45\ mH$. The characteristic time of the equivalent circuit (see Fig. A.7) is $\tau = \dfrac{L}{R} \cong 1\ s$.

The current waveform derived from the R-L circuit equation is

$$\begin{aligned} \hat{R} I(t) &= V \\ \hat{R} &= \left(L\frac{d}{dt} + R \right) \\ I(t) &= \frac{V}{R}\left(1 - e^{-\frac{t}{\tau}}\right) \end{aligned} \tag{A.17}$$

In eq. (A.17) we have introduced the operatorial impedance $\hat{R}$ and we define the power necessary to sustain the circuit as

$$P = I(t)\hat{R}I(t) = \left(\frac{1}{2} L\frac{d}{dt} + R \right) [I(t)]^2 \tag{A.18}$$

In steady state conditions the dissipated power is just of ohmic nature. Therefore to achieve $800\ A$ a voltage of $34\ V$ is required and the associated power demand in the steady state regime is $27\ kW$.

It is important to estimate also the costs of operation. If we assume a time of operation of about $900\ hour/year$ and a cost for electricity of 0.22 €$/kWh$ (for industrial use), the annual cost is given by

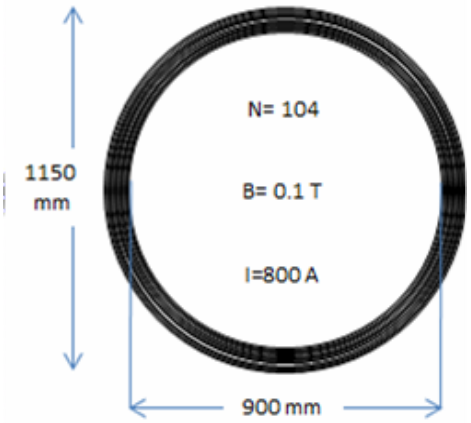

Figure A.5: Conceptual scheme.

Length L_s	195 mm
Mag. Field B	0.1 T
Total nr of turns N	104
nr of shells	8
coil/shell	13
Int. radius a	450 mm
Ext. radius b	575 mm
Current I	800 A
Wire section φ	130.5 mm^2
Wire length L_w	332 m
Ampere turns	832600

Table A.1: Constructive parameters.

Figure A.6: Constructive parameters and conceptual scheme for the GUN solenoid. The chosen parameters allow to match with mechanical and magnetical Dimension have been estimated by assuming a square section hollow wire and by considering also the thickness (*1 mm*) of the insulating enamel between coils.

$$Cost = P \cdot \frac{hour}{year} \cdot \frac{€}{kWh} \tag{A.19}$$

which gives an expense, with the considered parameters, of $5300,00\ €/year$.

The discussed parameters are listed in Tab. A.2

Resistivity ρ	$1.68 \cdot 10^{-8} \Omega m$
Resistance R	43 $m\Omega$
Current	800 A
Dissipated power P	27 $kWatts$
Voltage V	34 $Volts$
Cost	5300 $€/year$

Table A.2: Parameters for the power supply and electricity consumption. The considered costs for electricity is assumed to be 0.22 $€/kWh$at the actual quotation for industrial use.

According to the chosen geometry, the current is the only parameter that can be varied during operation of the machine. It is interesting to have a look at what happens in term of power consumption. Plots of these parameters are shown in Fig. A.8.

Parameters can be relaxed if we want a lower M-Field. Some possible operation sets are given in Tab. A.3.

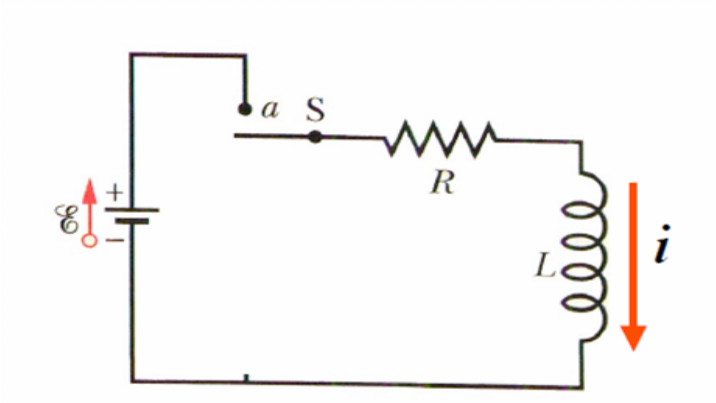

Figure A.7: The equivalent R-L circuit of a solenoid.

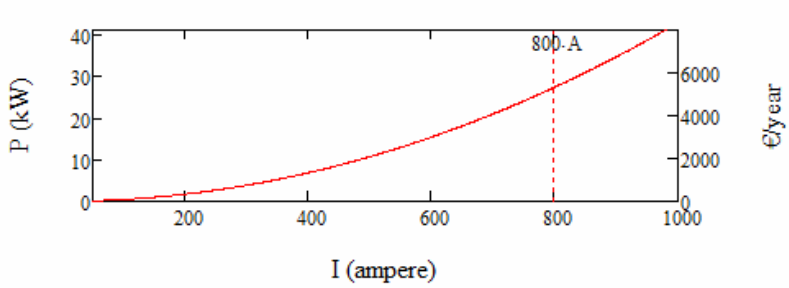

Figure A.8: Power vs. current and relative costs of electrical consumption.

A.4 Other Mechanical Considerations

Before concluding let us consider some technical issue, relevant to the feasibility of such a device.

The magnetic pressure can be calculated from the energy stored inside the solenoid and we find

$$P_M \cong \frac{B^2}{2\,\mu_0} \cong 4 \cdot 10^3 Pa \tag{A.20}$$

By assuming a surface of $0.64\ m^2$ we find that the force due to the coil on the supporting structure is $2.54 \cdot 10^3 N$.

If $d_{cu} = 8.96 g/cm^3$ is the copper density, we can know also the weight of the whole coil as

$$W_c = L_w \varphi^2 d_{cu} = 390\ kg \tag{A.21}$$

The coil must be shielded with a yoke of mild steel to contain the magnetic field line in the outer region. Considering a circular yoke with that have to contain the solenoid, with a thickness of $1.5\ cm$ and the two circular bored lateral plates, on can estimate the yoke weight around $150\ kg$ giving

Current I	800 A	600 A	400 A
Mag. Field B	0.1 T	0.075 T	0.05 T
Dissipated power P	27 $kWatts$	15 $kWatts$	7 $kWatts$
Voltage V	34 $Volts$	26 $Volts$	17 $Volts$
Cost	5300 €/$year$	3000 €/$year$	1300 €/$year$

Table A.3: Possible operating current regime and relative achievable magnetic field and power supply requirements.

a total weight (coil + yoke) of $\approx 540\ kg$.

To be considered also the conductor type related to the cooling system. We already noticed that the section of the wire should be square to reduce the resistance. Also the cooling system gives constraints. The high dissipated power requires that the coolant is directly in contact with the wire and this is possible if an hollow conductor is used [18]. In the previous calculation we considered hollow conductor wire with a bore of diameter 7 mm. The appearance of the coil in section is given in Fig. A.9

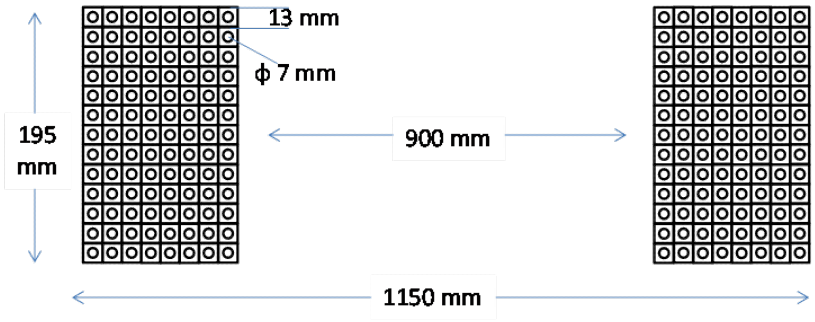

Figure A.9: Horizontal section of the coil. The dimension of the wire and the hollow conductor structure is shown. The real number of wires is reported but the central bore dimension is not in scale.

Technical Addendum B

Superconducting Magnet

B.1 CARM Magnets and Relevant Field Specifications

In Fig. B.1 we have detailed the field profile along with the expected intensity values and we have provided a sketch of the core part of the device from the cathode to the region in which the interaction between the electron beam and the high intensity magnetic field determines the CARM coherent emission.

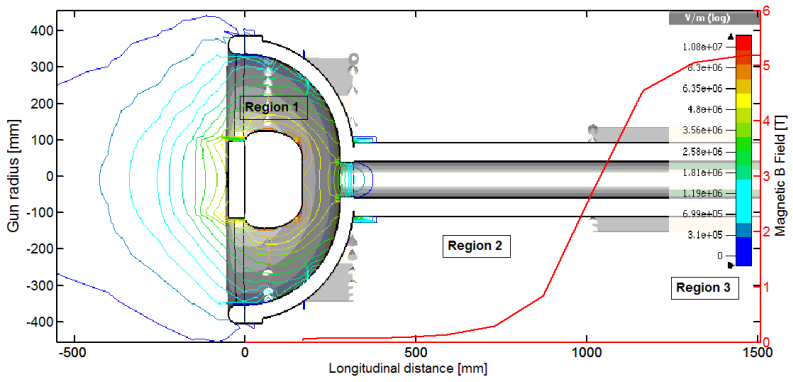

Figure B.1: Magnetic field intensity profile from the cathode to the interaction region with the three operating region: 1) Acceleration and beam forming region, 2) Adiabatic tapering, 3) High field interaction region.

The numbers reported below in Tabs. B.1, B.2 are used as reference values and summarizes what has been discussed in Chs I and III of the general part.

Referring to Fig. B.1 the whole transport line can be described as it follows:

1) ***Cathode-anode region***, external diameter 800 *mm* and total length *110 mm*;

2) ***Adiabatic field region***, space for "smooth" tapering of the electron beam radius before the injection inside the cavity;

3) ***Interaction region***, diameter of *100-120 mm*, length *300 mm* superconducting solenoid magnetic field intensity *7 T* (We are quoting the maximum achievable field, even though a lower intensity is required for CARM operation).

As already discussed in the introductory remarks and detailed in the forthcoming annexes, region "1" is aimed at guiding the electron annular-beam with suitable characteristics (energy spread, emittances, pitch angle ...) inside the cavity, thus ensuring sufficient gain for the CARM operation. Either "2" and "3" provides the core of the interaction; in the region "2" the field is ramped in order to reduce the radius and avoid the growth of the unwanted cavity modes. The field intensity in the region "3" should be sufficiently flat to ensure a correct mode selection and tuning.

The conditions for an appropriate "matching" of the e-beam inside the flat region, will be discussed later. The field intensity profile is reproduced in Figs. B.3 and B.4 and is realized by a superconducting (SC) coil, producing the *7 T* field and by correcting SC coils playing the complementary role of "fine" tuning.

The magnetic field intensity for a superconducting magnet exhibiting the specifications given below was simulated in ENEA Superconducting laboratory by using OPERA software with fully satisfying results. Quotations were then asked to several international enterprises for such a superconducting magnet, both to verify the realizability of the project and to have a rough idea about the cost of the whole magnet system, consisting of:

- Coil/coils,
- Solenoid,
- Current supplier (one ore more),
- Cryo-system (to provide the liquid helium to cool superconducting coils and solenoid),
- Mechanical support (to counteract the magnetic forces between coil and solenoid and to align both coils and solenoid),
- Shields (to protect the electronic devices from the dispersed magnetic flux),
- Control system, for the remote utilization of the superconducting magnet (to be integrated in the general CARM control system).

Maximum field intensity	*7 T*
Field homogeneity	*0.1%*
0.1% homogeneity region extension	*200 mm on the longit. z axis*
Operation regime	*continuous*
Length of the magnet (includes fringing)	*800 mm*
Bore diameter	*150 mm*
Single coil length	*25 mm*
Number of turns × coil	*712*
Number of coils	*21*
Current value maximum field intensity	*300 A*

Table B.1: *7 T* superconducting solenoid specifications.

Maximum field intensity	*0.5 T*
Operation regime	*continuous*
Length of the magnet (includes fringing)	*100 mm*
Bore diameter	*200 mm*
Single coil length	*4.6 mm*
Number of turns × coil	*90*
Number of coils	*4*
Current value 0.5 T field intensity	*153 A (J=200 A/mm^2)*

Table B.2: Superconducting correcting coil.

The relevant characteristics are reported in the Tabs B.1 and B.2 given below.

The transverse structure of the annular beam does not impose any particular prescription about the radial magnetic field profile. Additional correcting coils can be added to adjust the longitudinal field dependence, in order to ensure a further knob for an appropriate beam transport, as discussed in the Annex C, and can be placed in front of the superconductive solenoid and mechanically connected to it. These features of the magnetic system were objects of the discussions between us and the companies we asked the quotation to because it seemed difficult to mechanically connect structures with so big magnetic forces acting one on the other.

The parameters reported in the previous Tabs and the field profile sketched in the figures which follow are the result of numerical simulations performed with **Opera.** The OPERA Suite simulations were performed by using *Ni Ti* wires (Bruke EAS Gmbh; info@bruker-eas.com). The superconducting material used for the wire, and the other relevant characteristics of the the geometry and the details about the wires are given in the Fig. B.2.

The Fig. B.3 shows the longitudinal profile of the magnetic field provided by the superconducting *7 T* magnet without (blue curve) and with

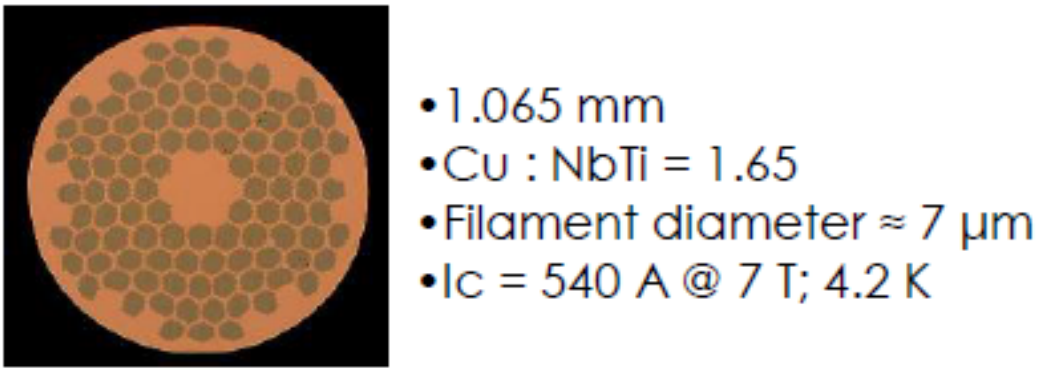

Figure B.2: The detailed structure of the superconducting coil (SC), the relevant geometrical characteristics and the composition of the SC wire.

(red curve) correcting coils.

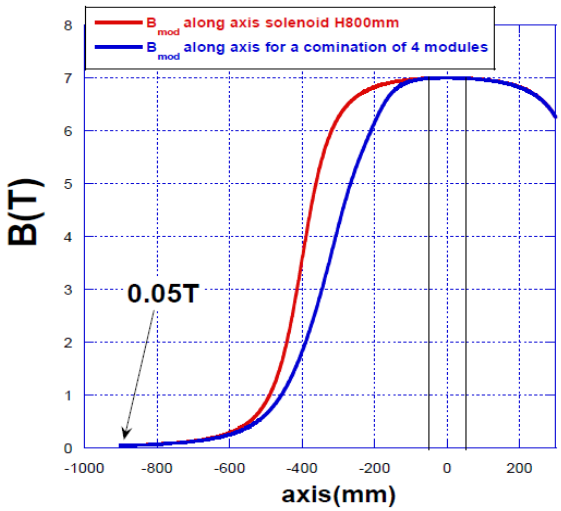

Figure B.3: On axis magnetic field vs. the longitudinal coordinate.

The Fig. B.4 shows several magnetic field profiles associated with different coil details (length of the single coil, length of the whole solenoid...) exhibiting the right value for the homogeneity (*0.1%*) and the right dimension for the *0.1* homogeneity along the z axis.

The approximative cost for the whole system as previously defined in this annex, with only one current supplier and one correcting coil, was quoted by the international enterprises we asked to at nearly *340 K€*.

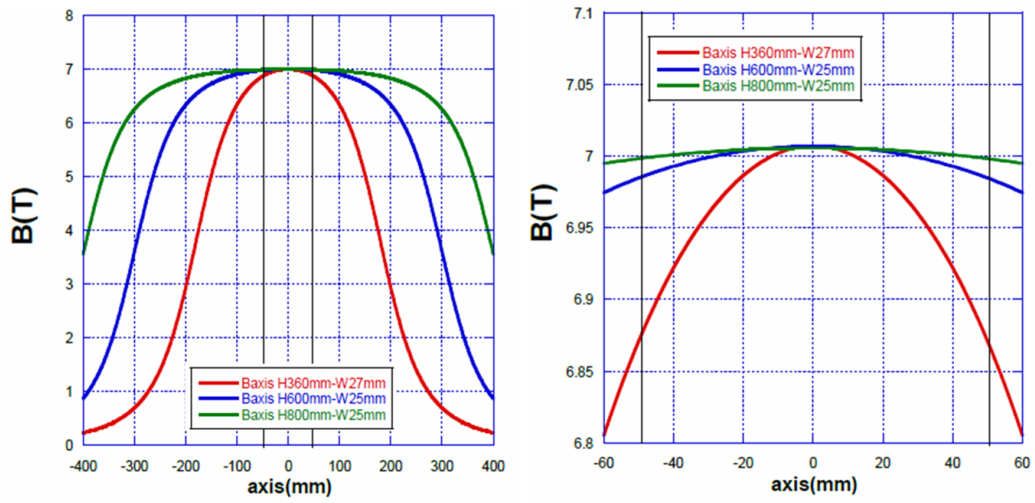

Figure B.4: On axis magnetic field for different coil geometries.

Technical Addendum C

Electron Beam Evolution Along the Transport Line

As already stressed in the introductory parts of this Report, the transport line from the cathode to the cavity region, is of paramount importance to obtain an e-beam with suitable characteristics for the CARM operation. The relevant design strategy can be summarized as it follows (see Fig. B.1):

a) The first part segment (namely the transition from region 1) to 2) has the role of bringing the electrons to a kinetic energy of $0.6\ MeV$, furthermore it is supposed to induce a kick due to the electric field of the edge cusp (see below) leading to a transverse component velocity, yielding an appropriate pitch angle of the e-beam providing a suitably large coupling with the cavity modes.

b) The "drift" section before the region 3), where the combined magnetic field of the principal and correcting coil is present, has a manifold role.

c) To Control the transverse motion components, by adjusting the pitch to an optimum value.

d) To control the radius of the anular beam and eventually the thickness of the corona

e) To match the section of the beam to the cavity mode to be enhanced by the CARM interaction. The matching should be achieved in an adiabatic way by eliminating (through a gentle tapering of the e-beam ring radius) the coupling to unwanted mode in the region of the cavity containing the Bragg reflector (see Fig. B.1 where we have superimposed the field intensity tapering to the cavity region).

In Fig. C.1 we have reported the pitch ratio evolution along the longitudinal coordinate and we have underscored the region where the kick occurs and the successive concurring effect of the magnetic field, which, among the other things, counteracts the growth of the transverse motion.

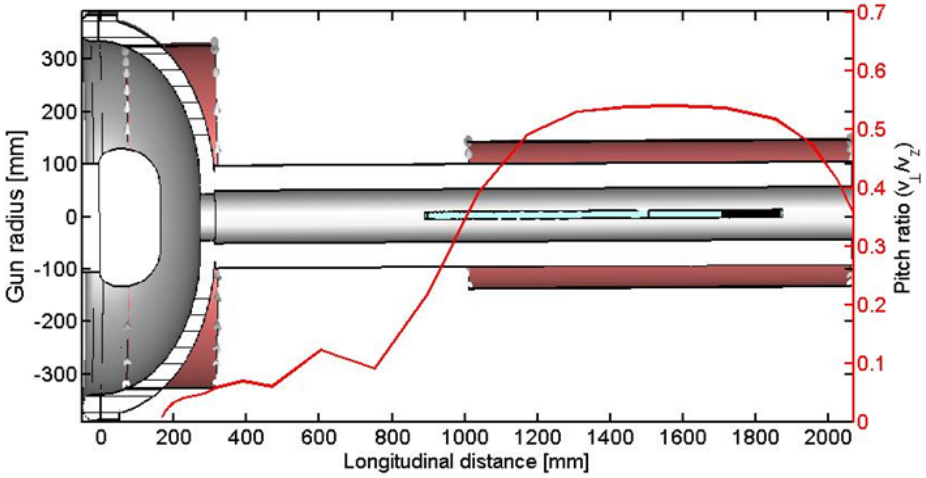

Figure C.1: Pitch evolution $\left(\frac{v_\perp}{v_z}\right)$ vs. the longitudinal direction.

In Fig. C.2 we report the evolution along the transport line of the spread of the longitudinal velocity, which grows with increasing transverse velocity component, but remains, in the interaction region well within the limits for a safe CARM operation.

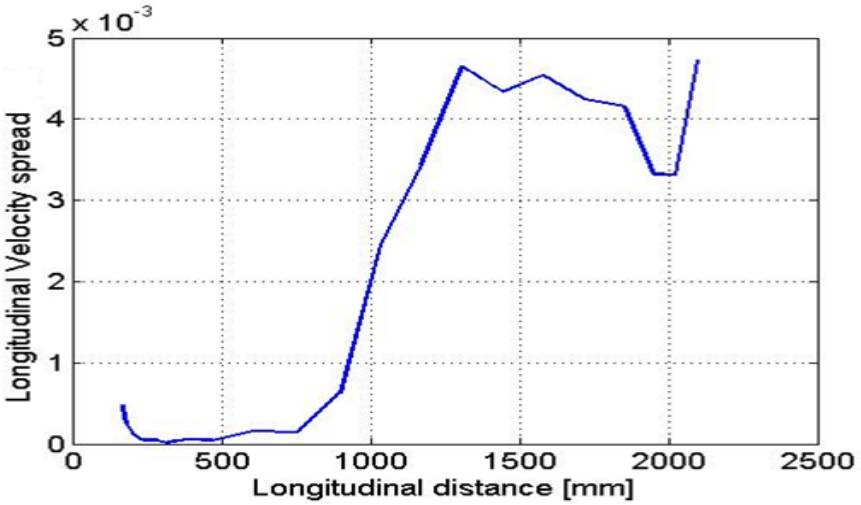

Figure C.2: Relative longitudinal velocity spread $\left\langle \frac{\Delta v_z}{v_z} \right\rangle_{rms}$ along the transport line (coordinate z).

In Fig. C.3 we have reported the beam radius vs. the transport coordinate and it is evident that in the interaction region the beam has the suitable dimensions to couple to the cavity modes.

A more appropriate idea is offered by Fig. C.4, yielding the transverse profile of the beam at different position along the transport line. It is evi-

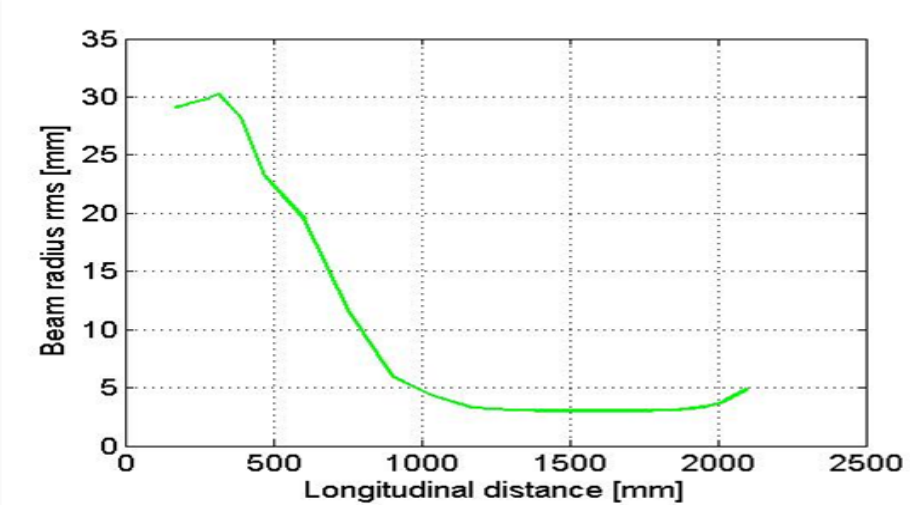

Figure C.3: Annular beam radius vs. the longitudinal coordinate z.

dent that the control of either radius and the thickness of the circular corona may become problematic.

The study we have developed so far is not based on a very refined theory to optimize the transport detail. We have indeed merely used a ray-tracing procedure to study the particle distribution and not an elaborated technique, as in the case of strong focusing, based on a formalism a lá Courant and Snyder. Within such a context concepts like emittance and Twiss parameters could provide a substantive help too. We must however emphasize that we are dealing with the transport of an e-beam with unusual characteristics. In standard acceleration and transport problems the beam is solid (without any hole) so that the concept of quantities like emittance and phase space domain are easily defined. To overcome such a drawback, we have developed a different point of view, namely we have visualized the beam as a collection of beamlet around the corona as illustrated in Fig. C.5. The use of such a point of view is helpful to check the reliability of the previous analysis and reconcile our procedure with a more conventional point of view.

According to the usual procedure we define the r.m.s. of the x and y position and of the relevant velocity components, defined as

$$\begin{aligned} \xi' &= \frac{d\xi}{dz}, \\ \xi &= x, y \end{aligned} \tag{C.1}$$

We then introduce the 2×2 covariance matrices

$$
\begin{aligned}
&\hat{C}_{x,x'},\, \hat{C}_{y,y'},\, \hat{C}_{x,y},\\
&\hat{C}_{\xi-\xi'} = \begin{pmatrix} \sigma_{\xi\xi} & \sigma_{\xi\xi'} \\ \sigma_{\xi'\xi} & \sigma_{\xi'\xi'} \end{pmatrix},\ \hat{C}_{x,y} = \begin{pmatrix} \sigma_{xx} & \sigma_{xy} \\ \sigma_{yx} & \sigma_{yy} \end{pmatrix},\\
&\sigma_{\xi\xi} = \sqrt{\langle \xi^2 \rangle - \langle \xi \rangle^2},\\
&\sigma_{\xi'\xi'} = \sqrt{\langle \xi'^2 \rangle - \langle \xi' \rangle^2},\\
&\sigma_{\xi\xi'} = \sqrt{\langle \xi'\xi \rangle - \langle \xi' \rangle \langle \xi \rangle}.
\end{aligned}
\tag{C.2}
$$

To give an idea of how these quantities evolve, we have reported in Figs. C.6 the evolution along the longitudinal direction of the square root of the associated determinants. In Fig. C.6a we have reported the behavior of $\sqrt{\left|\hat{C}_{x,y}\right|}$ which represents the *rms* area of the annular beam. The evolution of $\sqrt{\left|\hat{C}_{x,x'}\right|}$, $\sqrt{\left|\hat{C}_{y,y'}\right|}$ is shown in the plots of Fig. C.6b. These quantities could be interpreted as the the longitudinal and vertical emittances [1]. A general conclusion which can be drawn from the previous plots is that the condition of minimizing either $\left|\hat{C}_{x,y}\right|$ and $\left|\hat{C}_{x,x'}\right|$, $\left|\hat{C}_{y,y'}\right|$ in the interaction region cannot be achieved, the "matching" condition consists in a gentle comporomise, to be achieved by relaxing the request on the surface minima.

A general comment and a caveat should be added; in designing the transport line of the CARM device we have been faced with a number of design problems, hereafter specified

a) The absence of an appropriate theoretical framework to handle this type of beam transport as in the usual Courant Snyder (*C-S*) theory, allowing the definition of quad-like lenses to drive the beam.

b) The difficulties associated with the control of either annular beam radius an corona thickness.

c) The extreme sensitivity of these quantities to the magnet field distribution inside and outside the cavity interaction region.

[1] There are technical issues regarding the definition of emittance suggested in this text. The quantity we have mentioned does not, strictly speaking, represent an emittance, it refers to the particle beam phase space area and is a conserved quantity during the transport. Its rigorous definition requires the use of canonical variables to properly treat the phase space and the relevant transport. Regarding our case we have used the transverse velocities, which, for the type of fields and forces involved in, are kinetic and not canonical variables. Furthermore, the quantities we have reported are not a transport invariant for different reasons, including the fact that we are not dealing with a Liouvillian transport along the entire line and that, inside the main solenoid, the *x-y* motion is coupled and therefore the real invariant is associated with the *6-D* phase space.

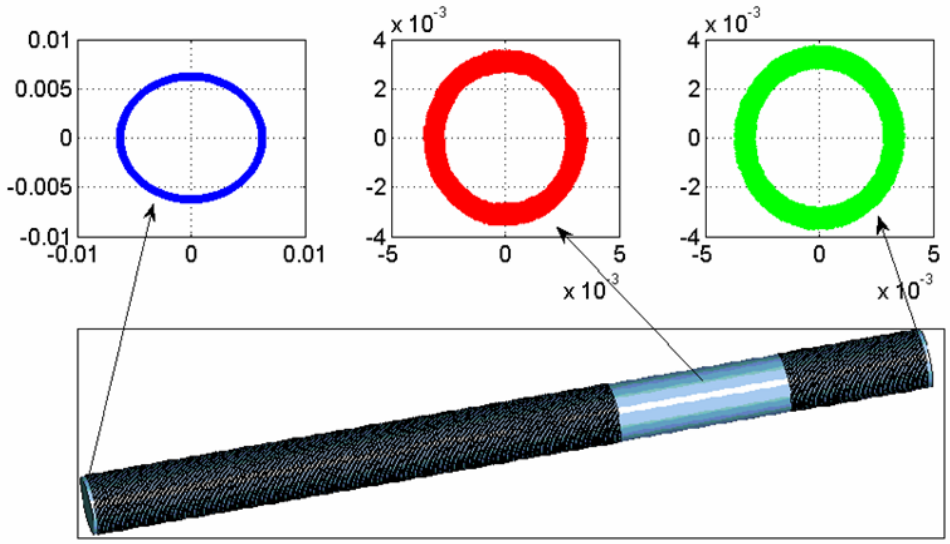

Figure C.4: Geometrical distribution of the beam at different position along the longitudinal axis, *a*) $z = 900\ mm$, *b*) $z = 1613\ mm$, *c*) $1873\ mm$.

d) The importance of the emitting cathode surface roughness, only partially accounted for.

The results we have obtained show that

i) A *C-S* like theory can be partially recovered and some of the relevant paradigmas can be exploited within the present context.

ii) The annular beam geometry and shaping can in principle be controlled, but an analysis of the relevant criticity has not been done.

iii) A global matching of the beam (including the adequate contion on velocity spread) can be obtained, but optimization criteria has not been found yet.

All the above points will be the subject of an intensive study either numerical and theoretical.

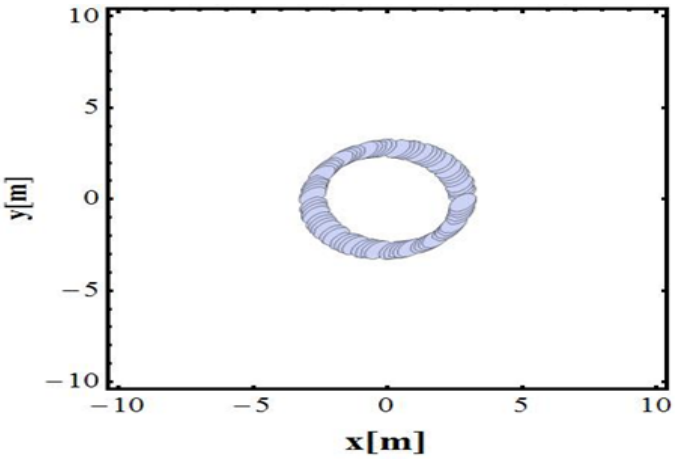

Figure C.5: Beamlet realization of the beam circular corona.

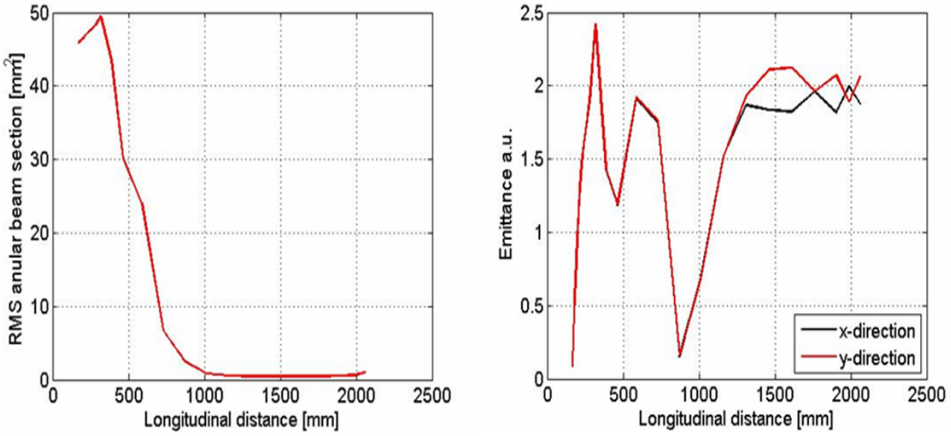

Figure C.6: a) Annular beam r.m.s. area $\left(\sqrt{\left|\hat{C}_{x,y}\right|}\right)$ vs longitudinal coordinate; b) emittance (arbitrary units) $\left(\sqrt{\left|\hat{C}_{x,x'}\right|}, \sqrt{\left|\hat{C}_{y,y'}\right|}\right)$ vs. thelongitudinal coordinate (in current units the a.u. units should be multiplied by $10 \cdot mm \cdot mrad$).

Technical Addendum D

Mode Selection, CARM Theory and Scaling Relations

D.1 Introduction

In the previous addendum we have detailed the beam transport criteria, aimed at providing the e-beam injection, in the cavity region, with the suitable geometrical shape to ensure an efficient overlapping with the chosen TE mode for the CARM operation. To better clarify this point, we have reported in Figs. D.1a-D.1b the intensity distribution of the $TE_{8,2}$ and $TE_{5,3}$ modes, including the e-beam transverse profile (in red). The minimal request, for a safe operation, is that the electrons be contained within the region in which the mode has a non-zero intensity distribution and possibly intercept the maxima.

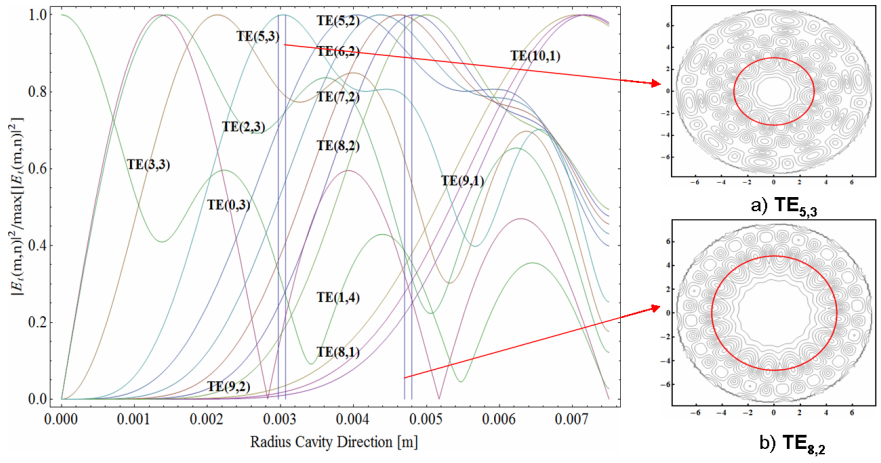

Figure D.1: Transverse Mode distribution vs. the cavity radius, the vertical lines refer to beam transverse dimensions interacting with the $TE_{5,3}$ or $TE_{8,2}$ mode; on the right side the transverse mode distribution with the transverse annular beam in red.

The procedure of mode selection encompasses the following steps

1. The mode distribution is plotted vs. the cavity radius (Fig. D.1), the e-beam transverse section is superimposed to intercept a specific mode. The figure shows that, even for a beam with thickness of few hundred microns, a plethora of modes may be excited by the electron beam current

2. The longitudinal mode selection can also be figured out by using the Brillouin diagram reported in Fig. D.2, where we have reported the dispersion curves of different modes and the relevant intersection with the e-beam line. It is evident that a clean mono-modal operation is this case ensured whenever the beam has a suitably well-defined energy distribution

3. The cold cavity dispersion relations should be embedded in a dynamical theory to estimate the growth rate of each mode, including either the mode-beam distribution, overlapping factor and the other factors we have mentioned in the introductory section.

The accomplishment of step "3" requires a detour on the CARM theory, which will be discussed with a few details, in the forthcoming part of the annex.

The theory of CARM and U-FEL devices is well established. The underlying Physics is satisfactorily well described by the theoretical formulations dating back to more than thirty years ago. The numerical codes originated by these analyses are powerful working tools, useful to analyze experimental data and to fix the design details of new devices.

Even though different, in many constructive details, the physical mechanism, underlying the operation of either CARM [19] and U-FEL [20], traces back to the power transfer from the e-beam to a coherent electro-magnetic field, through a klystron like mechanism, which is the common ancestor for these families of free electron coherent generators [21]. The possibility of establishing a common thread, between these devices, has been discussed in many authoritative papers in the past [22]. More recently [23] some of the present authors used the theoretical analyses developed in refs. [24]-[26] to provide the translation of the CARM into U-FEL formalism by means of the analytical formulae summarized in ref. [27], providing the back-bone of the ***PARSIFEL*** code [28].

The pathway leading to PARSIFEL is the result of an effort aimed at merging analytical formulae, derived from U-FEL theory and scaling relations, benchmarked through the available numerical codes, to get an accurate, reliable and semi-analytical code devoted to preliminary design of FEL, operating in different configurations.

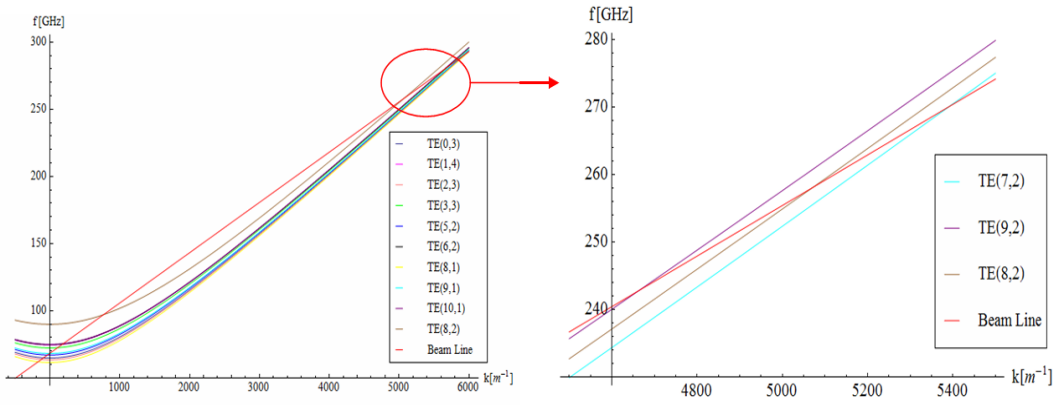

(a) Brillouin diagram and beam line interaction.

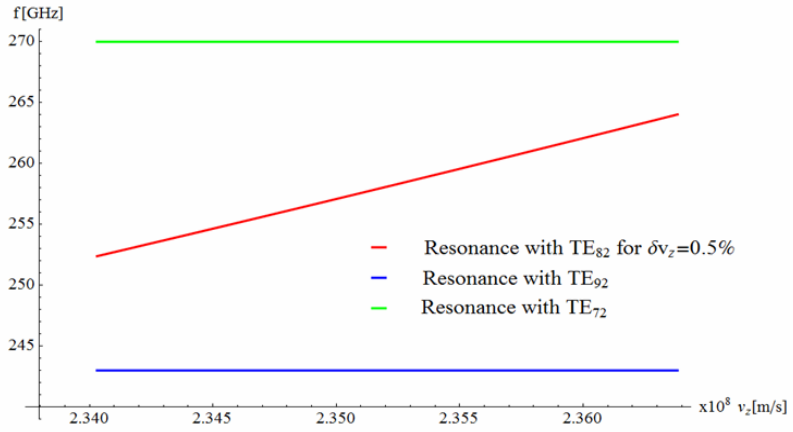

(b) The resonance frequency range for a beam line with an energy spread (*0.5%*) interacting with the TE_{82} mode, well separated from the resonance with the competitor modes TE_{92} (blue line) and TE_{72} (green line).

Figure D.2: Dispersion curves of different modes and the relevant intersection with the e-beam line.

In this annex we perform a step further towards an extension of a PARSIFEL like conception to CARM devices.

Regarding CARM we keep, as reference papers, those listed in refs. [24]-[25] and for U-FEL we have referred to the lines developed in the past by different Authors and summarized in books and review articles, a partial list of which is reported in refs. [29]-[31].

In this introductory section, we will provide a quick review of the results obtained in ref. [24] and fix the formalism, we will adopt in the forthcoming parts of the paper.

We remind that in a CARM-FEL a moderately relativistic e-beam, moves, inside a wave guide under the influence of an axial magnetic field, executing a helical path with a cyclotron frequency $\Omega_0 = \dfrac{e\,B}{m_e}$.

The kinematical variables of the electron beam are specified by the longitudinal (v_z) and transverse ($v_\perp$) velocity components, linked to the relativistic factor γ by

$$\begin{aligned} &\beta_z^2 + \beta_\perp^2 = 1 - \frac{1}{\gamma^2}, \\ &\beta_{z,\perp} = \frac{v_{z,\perp}}{c}, \\ &\alpha = \frac{v_\perp}{v_z} \end{aligned} \tag{D.1}$$

where α is the already defined pitch factor.

The electrons, with longitudinal velocity v_z, interact with a co-propagating electromagnetic field characterized by a wave-vector k_z, linked to the wave phase velocity v_p by

$$k_z = \frac{\omega}{v_p} \tag{D.2}$$

In the case of magnetic undulators the electrons (with the same aforementioned kinematical attributes) enter into an alternating (transverse static) magnetic field with period λ_u, where execute transverse oscillations.

In this case the emission process is not constrained by any waveguide condition, therefore no complications arise with the wave phase velocity.

The two devices can be considered "topologically equivalents", therefore useful analogies can be defined after a judicious analysis of the emission mechanisms.

The derivation of the wavelength, characterizing the emission process inside the undulator, can be obtained using a fairly simple argument. The difference in velocities is such that, after one undulator period, the radiation has slipped ahead of the electron beam by the so called *slippage length*

$$\delta = (c - v_z)\,\frac{\lambda_u}{c} = (1 - \beta_z)\;\lambda_u \tag{D.3}$$

Since δ is linked to the phase advance of the electromagnetic wave with respect to the electrons, constructive interference of the wave front of the emitted radiation at the next undulator period is ensured if

$$\delta = \lambda \tag{D.4}$$

where λ is the frequency of the co-propagating field.

The last two equations yield the FEL resonance condition, which can also be cast in the form

$$\begin{aligned} \omega &= \frac{2\pi\, c}{\lambda} = \frac{\omega_u}{1 - \beta_z}, \\ \omega_u &= \frac{2\,\pi\, c}{\lambda_u} \end{aligned} \tag{D.5}$$

to this aim we note that the electrons, with relativistic factor γ, enter inside the undulator, where, on account of the Lorenz force induced by the magnetic field, acquire a transverse velocity component $\beta_\perp$, the longitudinal velocity can accordingly be written, using eq. (D.1), as

$$\begin{aligned} \beta_z &= \sqrt{1 - \frac{1}{\gamma_z^2}}, \\ \gamma_z &= \frac{\gamma}{\sqrt{1 + \alpha^2}} \end{aligned} \tag{D.6}$$

If the relativistic factor is large enough to allow a series expansion of the square root, in the first of the eqs. (D.6), at the lowest order in $\dfrac{1}{\gamma^2}$, we find

$$\omega \cong 2\,\frac{\gamma^2}{1 + \alpha^2}\omega_u \tag{D.7}$$

The previous derivation can be extended to CARM by noting that the relevant "***resonance***" condition, can be determined by using the same argument as before about constructive interference, which occurs whenever the accumulated slippage between radiation and electrons, in a helix period, equals the wavelength λ. By taking into account that the link between helix period and guiding magnetic field is provided by

$$\Lambda = \frac{c}{\Omega} \tag{D.8}$$

we impose the resonance condition as

$$(v_p - v_z)\,\frac{\Lambda}{c} = \lambda \tag{D.9}$$

Where we have used the phase velocity v_p to determine the radiation electron slippage.

The previous eq. (D.9) can also be written in the more familiar form

$$\omega = \frac{\Omega_0}{\gamma} + k_z v_z \tag{D.10}$$

The above equation has been derived by using a kinematical argument and the analogy with U-FEL has been the pivotal element of the discussion. The physical origin of the previous identity can however be understood on the basis of different arguments, involving e.g. momentum (electron & fields) conservation.

We can further elaborate the previous identities, denoting by ω_R the resonant frequency, we obtain, from eq. (D.10)

$$\begin{aligned} \omega_R &= \frac{\Omega}{1 - \dfrac{v_z}{v_p}}, \\ \Omega &= \frac{\Omega_0}{\gamma} \end{aligned} \tag{D.11}$$

It is worth stressing that, being the phase velocity dependent on the field frequency, eq. (D.11) is not an explicit solution for ω, but only an approximation.

Before further pushing the analogy between U and CARM FEL, we dwell on the physical meaning of the previous equations.

The CARM resonance condition can also be derived by requiring the matching between eq. (D.10) and the waveguide dispersion relation

$$\omega^2 = c^2(k_\perp^2 + \beta_p^2 k_z^2) \tag{D.12}$$

where $k_\perp$ is the transverse mode wave number, associated with the cutoff frequency $\omega_c = ck_\perp$. It is easily checked that, from (D.10) and (D.11), one gets

$$\omega_\pm \cong \frac{\Omega}{1 \mp \dfrac{\beta_z}{\beta_p}} \tag{D.13}$$

The down shifted intersection, yielding the gyrotron mode [19], will not considered in the following.

The upper shifted counterpart ω_+ is the resonant (CARM) frequency and, to better understand its role, it will be rewritten as

$$\begin{aligned} \omega_R &\cong \frac{\Omega}{1-\frac{\beta_z}{\beta_p}} = \frac{\Omega}{1-\frac{1}{\beta_p}\sqrt{1-\frac{1}{\gamma_z^2}}} \cong 2\beta_p\,\gamma_z^2\Omega, \\ \gamma_z &= \frac{\gamma}{\sqrt{1+\alpha^2}} \end{aligned} \tag{D.14}$$

based upon the assumption that γ_z be sufficiently large that $\sqrt{1-\frac{1}{\gamma_z^2}} \cong 1-\frac{1}{2\,\gamma_z^2}$.

Eq. (D.14) accounts for the frequency Doppler up-shift mechanism, characterizing most of the free electron devices.

It is important to emphasize that, at least formally, we have established so far an important analogy between CARM and U-FEL, namely $\Lambda \leftrightarrow \lambda_u$, which justifies the remark that the two devices are topologically equivalent.

The role of the transverse velocity needs a more accurate comment. In the case of the U-FEL the transverse component, induced by the Lorenz force, is the tool allowing the coupling with the co-propagating electromagnetic (transverse) field. The explicit dependence of α on the undulator parameters is provided by

$$\begin{aligned} \alpha &= \frac{K}{\sqrt{2}}, \\ K &\propto e\,B_0\lambda_u \end{aligned} \tag{D.15}$$

In the case of the CARM the role of the transverse velocity component is the same as that of the undulator strength in the undulator FEL.

This velocity component should be induced during the electron beam preparatory phase, before the injection into the cavity.

What we have described so far are the physical conditions underlying the "spontaneous" emission, which is the prerequisite for the onset of the coherent emission process. As is well known, it occurs via the bunching mechanism. The interaction of the electrons with the cavity electric field mode determines their energy modulation, which transforms into a density

modulation, followed by a coherent RF emission when the electrons are bunched on a scale comparable to the RF electric field wavelength.

This description encompasses all devices of FEL type, CARM is however made peculiar by the fact that the auto-resonance is guaranteed even near saturation because any increase of Ω is balanced by a corresponding decrease of the longitudinal velocity[1].

A further important quantity, characterizing U-FEL, is the number of undulator periods, which is associated with the oscillations executed by an electron, while travelling inside the undulator. In the case of CARM it can be linked to the number of helical turns of the electrons inside the magnet. Accordingly we get

$$\begin{aligned} \Omega \frac{L}{\beta_z c} &= 2\,\pi\, N \\ N &\cong \frac{L}{\Lambda} \end{aligned} \tag{D.16}$$

We have fixed the main element of our strategy and in the following section we will see how the correspondences, we have established, may provide an effective tool to evaluate the CARM evolution.

D.2 The CARM Small Signal Theory

In this section we will push further the analogy with U-FEL by showing that the equation describing the CARM field evolution in the linear regime, can be written by taking advantage from simplified expression valid in the former case.
In the analysis of the previous section we did not include any consideration regarding the interaction of the wave with the e-beam. The dispersion relation in eqs. (D.10)-(D.12) are appropriate for the "cold" wave guide condition, which merely applies to the kinematic of the mode propagation. The CARM dynamics, associated with the radiation intensity growth in the wave guide, undergoes different phases characterized by the amount of the field power density.
The weak coupling regime is characterized by a power level well below the threshold of the saturation intensity (namely the power density halving the small signal gain) and the relevant theory can be treated using perturbative methods and, to some extent, useful information can be drawn using analytical means. A significant result from such a treatment is the derivation

[1]The efficiency enhancement is induced in undulator based FELs by tapering the undulator, by reducing e.g. the undulator period, in order to maintain the resonance condition in eq. (D.5) fixed when β_z decreases, thus realizing the effect naturally entangled with CARM operating mechanism.

of a modified dispersion relation including the interaction of the electrons with the wave guide modes. According to refs. [32] we find

$$\frac{\omega^2}{c^2} = (k_\perp^2 + k_z^2) - \varepsilon \frac{k_\perp^2 \left(\omega^2 - c^2 k_z^2\right)}{\left(\omega - \dfrac{\Omega_0}{\gamma} - k_z v_z\right)^2} \tag{D.17}$$

where ε plays the role of coupling parameter. It depends on the beam current and on the geometrical parameters of the wave-guide itself and will be specified later in this section. The previous identity the crucial element of the forthcoming discussion and, for later convenience, we set

$$\begin{aligned} \tilde{k}_z &= k_z + \delta_{k_z}, \\ k_z &= \left(\frac{\omega^2}{c^2} - k_\perp^2\right)^{\frac{1}{2}} = \frac{\gamma\omega - \Omega_0}{\gamma v_z} \end{aligned} \tag{D.18}$$

with δ_{k_z} representing the deviation of the field longitudinal wave vector, induced by the coupling with the electrons. Inserting eq. (D.18) into (D.17) we find that δ_{k_z} is specified by the following fourth order algebraic equation

$$\beta_z^2 \delta_{k_z}^4 + 2\beta_z^2 k_z \delta_{k_z}^3 + \varepsilon k_\perp^2 \delta_{k_z}^2 + 2\varepsilon k_\perp^2 k_z \delta_{k_z} - \varepsilon k_\perp^4 = 0 \tag{D.19}$$

The roots of the above equation specifies the evolution of the CARM field amplitude along the coordinate z, according to

$$E(z) \propto \sum_{j=1}^{4} e_j e^{(\delta_{k_z})_j z} \tag{D.20}$$

where j refers to the roots of eq. (D.19) and e_j are integration constants, fixed by the conditions

$$\begin{aligned} &E(0) = 1, \\ &\left(\left(\frac{d}{dz}\right)^k E(z)\right)_{z=0} = 0, \\ &k = 1,\, 2,\, 3. \end{aligned} \tag{D.21}$$

The linearized field growth along the longitudinal coordinate can accordingly be obtained by plotting $|E(z)|^2$ as shown in Figs. D.3, D.4.

The evolution curve has the well-known shape, characterizing also the Self Amplified Spontaneous Emission (SASE) FEL operating mode, namely a lethargy region where the system (electrons and radiation) organizes the coherence and a linear (in logarithmic scale) growth with a characteristic gain length l_g. In the case of CARM such a quantity is specified by [32]

$$l_g^{-1} = 2\Gamma = \sqrt{3}\left[\frac{\varepsilon\, k_\perp^4}{16 k_z \beta_z^2}\right]^{\frac{1}{3}} \tag{D.22}$$

Let us now invoke the analogy with the U-FEL, whose gain length is defined as [27]

$$l_g = \frac{\lambda_u}{4\,\pi\,\sqrt{3}\,\rho} \tag{D.23}$$

with ρ being the Pierce parameter linked to the small signal gain coefficient g_0 by the identity [27]

$$\rho = \frac{(\pi\, g_0)^{\frac{1}{3}}}{4\,\pi\, N} \tag{D.24}$$

The use of the correspondences established in the previous section and the comparison between eqs. (D.22), (D.23) allows the following identification

$$\rho = \frac{\Lambda\,\Gamma}{4\,\pi\,\sqrt{3}} \tag{D.25}$$

The dependence of U-FEL field amplitude on the longitudinal coordinate has been shown to be provided by [27]

$$\begin{aligned}
&a(\tau) = \frac{a_0}{3(\nu+p+q)} e^{-\frac{2}{3}i\nu\tau}\left\{(-\nu+p+q)e^{-\frac{i}{3}(p+q)\tau} + \right.\\
&\left. +2(2\nu+p+q)e^{\frac{i}{6}(p+q)\tau}\left[\cosh\left(\frac{\sqrt{3}}{6}(p-q)\,\tau\right) + i\frac{\sqrt{3}\nu}{p-q}\sinh\left(\frac{\sqrt{3}}{6}(p-q)\,\tau\right)\right]\right\},\\
&p = \left[\frac{1}{2}(r+\sqrt{d})\right]^{\frac{1}{3}}, \qquad q = \left[\frac{1}{2}(r-\sqrt{d})\right]^{\frac{1}{3}},\\
&r = 27\,\pi\, g_0 - 2\,\nu^3, \qquad d = 27\,\pi\, g_0\left[27\,\pi\, g_0 - 4\,\nu^3\right]
\end{aligned} \tag{D.26}$$

and the intensity evolution is just given by $|a(\tau)|^2$.

The various parameters entering the above expression are recognized as

$\nu \equiv$ Detuning parameter
$z \equiv$ Longitudinal coordinate
$L \equiv N\,\lambda_u \equiv$ Interaction length
$\tau \equiv$ Dimensionless time

We can now get the correspondence with the CARM variables is obtained by defining the normalized detuning $\bar{\nu}$ parameter as

$$\bar{\nu} = \frac{\nu}{(27\pi\ g_0)^{1/3}} \tag{D.27}$$

and then by casting, using the relations (D.22)-(D.24), the dimensionless time in the form

$$\tau = \frac{z}{L} = \frac{z}{Nl_g 4\ p\ \sqrt{3}\rho} = \frac{2\ \Gamma z}{\sqrt{3}(pg_0)^{\frac{1}{3}}} \tag{D.28}$$

Thus finally ending up with

$$\nu\tau = 2\sqrt{3}\Gamma\bar{\nu}z \tag{D.29}$$

The complex amplitude (D.26) can now be assumed to be a function of the normalized detuning parameter $\bar{\nu}$ and of the inverse gain length Γ, which will be exploited to describe the small signal growth of the radiation field amplitude, namely

$$\begin{aligned} a(z,\Gamma,\bar{\nu}) &= \frac{a_0}{3} e^{-i\frac{4\Gamma\bar{\nu}z}{\sqrt{3}\beta_z}} \cdot \\ &\cdot \left\{ A_1 e^{-i\frac{2\Gamma z A_3^{(+)}}{\sqrt{3}}} + 2A_2 e^{i\frac{\Gamma z A_3^{(+)}}{\sqrt{3}}} \cdot \left[\cosh(\Gamma z A_3^{(-)}) + i\frac{\sqrt{3}\bar{\nu}}{A_3^{(+)}} \sinh(\Gamma z A_3^{(-)}) \right] \right\} \end{aligned} \tag{D.30}$$

with

$$\begin{aligned} A_1 :=& A_1(\bar{\nu}) = \frac{(-\nu+p+q)}{\nu+p+q} = \\ &= \frac{\left(\sqrt[3]{1-2\bar{\nu}^3+\sqrt{1-4\bar{\nu}^3}} + \sqrt[3]{1-2\bar{\nu}^3-\sqrt{1-4\bar{\nu}^3}} - \sqrt[3]{2}\bar{\nu} \right)}{\left(\sqrt[3]{1-2\bar{\nu}^3+\sqrt{1-4\bar{\nu}^3}} + \sqrt[3]{1-2\bar{\nu}^3-\sqrt{1-4\bar{\nu}^3}} + \sqrt[3]{2}\bar{\nu} \right)}, \\ A_2 :=& A_2(\bar{\nu}) = \frac{(2\nu+p+q)}{\nu+p+q} = \\ &= \frac{\left(\sqrt[3]{1-2\bar{\nu}^3+\sqrt{1-4\bar{\nu}^3}} + \sqrt[3]{1-2\bar{\nu}^3-\sqrt{1-4\bar{\nu}^3}} + 2\sqrt[3]{2}\bar{\nu} \right)}{\left(\sqrt[3]{1-2\bar{\nu}^3+\sqrt{1-4\bar{\nu}^3}} + \sqrt[3]{1-2\bar{\nu}^3-\sqrt{1-4\bar{\nu}^3}} + \sqrt[3]{2}\bar{\nu} \right)}, \\ A_3^{(\pm)} :=& A_3^{(\pm)}(\bar{\nu}) = \frac{1}{\sqrt[3]{2}} \left(\sqrt[3]{1-2\bar{\nu}^3+\sqrt{1-4\bar{\nu}^3}} \pm \sqrt[3]{1-2\bar{\nu}^3-\sqrt{1-4\bar{\nu}^3}} \right), \\ (p \pm q)\tau =& \frac{\sqrt{3}}{\sqrt[3]{2}} 2\Gamma z \left(\sqrt[3]{1-2\bar{\nu}^3+\sqrt{1-4\bar{\nu}^3}} \pm \sqrt[3]{1-2\bar{\nu}^3-\sqrt{1-4\bar{\nu}^3}} \right) = \\ &= 2\sqrt{3}\Gamma z A_3^{(\pm)} \end{aligned} \tag{D.31}$$

In Fig. D.3 we have provided a comparison between the prediction of the CARM theory and of the U-FEL scaling equations, given in eq. (D.26).

The agreement is satisfactory and further comments will be given below.

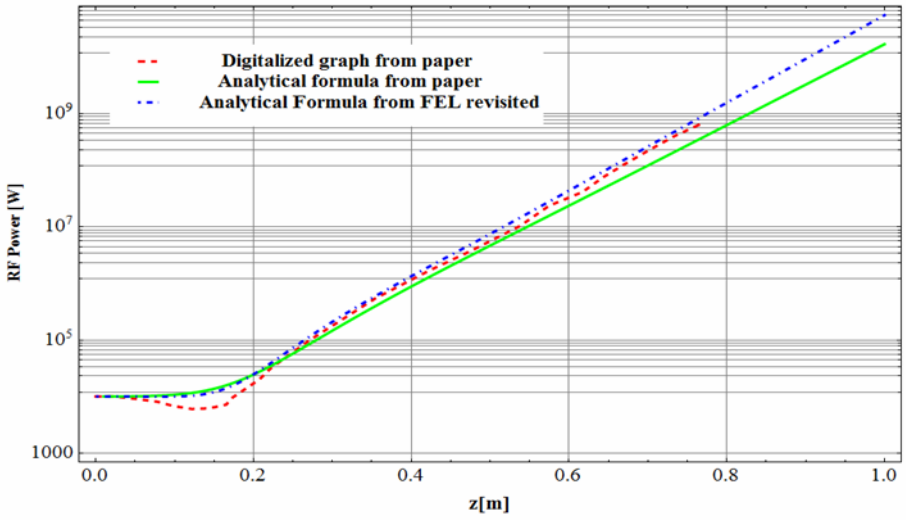

Figure D.3: Comparison between U-FEL (blue) and CARM (green) SSR (small signal growth) intensity growth curves with the result reported in the Wurtele paper ref. [32].

We should put in evidence that the linear solution obtained solving the dispersion relation (D.17) has been regularized neglecting the oscillating root of the equation (D.19) as reported in Fig. D.4 the comparison of the amplitude signal with and without the oscillating solution .

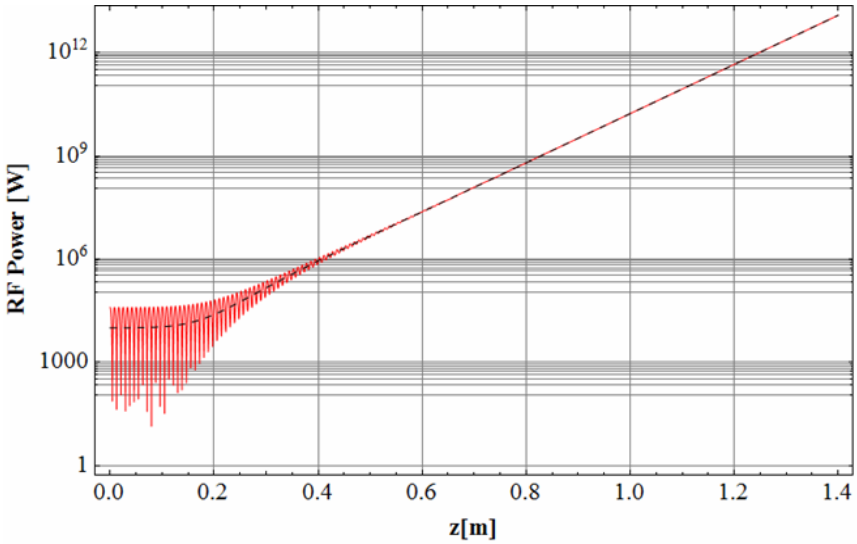

Figure D.4: Small signal CARM growing intensity, with and without the imaginary contributions from eq. (D.19).

The following two remarks are in order to complete the previous discussion

a) The dispersion relations for CARM and U-FEL lead to a fourth and third degree algebraic equations respectively. This is a consequence of the fact that the CARM field equations have been derived without the assumption of paraxial approximation, while, in the case of U-FEL the small signal problem is solved by the approximation of slowly varying envelope (SVE). This assumption leads to a treatment involving algebraic equations of one degree lower. In adapting U-FEL to CARM theory, according to the previous prescriptions and of ref. [24], we did not find particular differences, except for the lethargic parts, where the SVE approximation smoothen the field oscillations.

b) The eqs. (D.17)-(D.22) have been written without fixing the waveguide mode structure, we can however factorize the ε coupling parameter as the product of two terms, namely

$$\begin{aligned} \varepsilon &= \Xi\, \mathrm{f}, \\ \mathrm{f} &= \frac{4\,\pi\,\beta_\perp^2}{\gamma\,\beta_z}\left(\frac{I_b}{I_A}\right) \end{aligned} \tag{D.32}$$

where $I_{b,A}$ denote the beam and Alfvén current, the parameter Ξ summarizes the details of the cavity mode and the effect due to the geometrical overlapping between electrons and wave-guide modes and will be more carefully discussed in the following.

D.3 CARM Non-Linear Regime and Saturated Power

In the previous section we have developed quite a straightforward formalism to prove that most of the scaling formulae developed within the framework of FEL theory can be adapted to the study and design as well of CARM devices, at least for the case of small signal regime.
In this section we include the non-linear contributions and show that the logistic curve model [27]-[28] is an effective tool to study the evolution of the system up to the saturation.
The logistic growth curve belongs to the family of S-shaped curves, the model has been shown to be very effective in reproducing the evolution of any system undergoing a dynamical behavior ruled by an equation of the type

$$\frac{d}{d\,z}\mathrm{P} = \frac{\mathrm{P}}{l_g}\left[1 - \frac{\mathrm{P}}{\mathrm{P_S}}\right] \tag{D.33}$$

even though either CARM and U-FEL satisfy more complicated non- linear equations as to the growth of the power density. Eq. (D.33) captures the essential physics of the problem, namely a linear growth followed by a

quadratic non linearity when the power approaches $\mathrm{P_S}$ which denotes the saturated power. The solution of eq. (D.33) can be written as

$$\mathrm{P}\left(z\right)=\mathrm{P}_0\frac{e^{\frac{z}{l_g}}}{1+\frac{\mathrm{P}_0}{\mathrm{P_S}}\left[e^{\frac{z}{l_g}}-1\right]} \tag{D.34}$$

The definition of the CARM saturated power $\mathrm{P_S}$ is easily given by just following the prescription of ref. [20], we therefore set

$$\mathrm{P_S}\cong\eta\,P_E \tag{D.35}$$

where P_E is the electron beam power and η the efficiency of the device in turn provided by

$$\begin{aligned}&\eta=\eta_{sp}\eta_C,\\&\eta_{sp}\cong\sqrt{2}\rho\\&\eta_C\cong\frac{1}{\left(1-\beta_p^{-2}\right)\left(1-\gamma_0^{-1}\right)}\frac{\beta_\perp^2}{b}\end{aligned} \tag{D.36}$$

where we have denoted by $\eta_{sp,\,C}$ the single particle and collective efficiency, respectively [19]. The single particle efficiency, can be written using the analogy in terms of the Pierce parameter as t

$$\eta_{sp}\cong\sqrt{2}\rho=\frac{\sqrt{2}\Lambda\,\Gamma}{4\,\pi\,\sqrt{3}} \tag{D.37}$$

According to the previous identity the saturated power can be cast in the form

$$\begin{aligned}&\mathrm{P_S}\cong\frac{\sqrt{2}}{4\pi\sqrt{3}}\frac{\Lambda\,\Gamma}{\left(1-\beta_p^{-2}\right)\left(1-\gamma_0^{-1}\right)}\frac{\beta_\perp^2}{b}P_E,\\&b=\frac{\beta_\perp^2}{2\,\beta_z\beta_p\left(1-\frac{\beta_z}{\beta_p}\right)}\end{aligned} \tag{D.38}$$

According to the terminology of ref. [19],[25], b denotes the electron recoil parameter. It accounts for the auto-resonance contribution, including the effect of axial momentum and velocity change with the electron energy loss [20]. Regarding the analogy with U-FEL it can be associated with the undulator tapering parameter [33]-[34].

We have recovered all the crucial parameters (gain length and saturated power) to draw the CARM power growth curve, using the logistic equation. However, eq. (D.34) accounts only for the exponential growth prior the saturation and does not contain any lethargic phase. To overcome this

problem we replace the exponential term in eq. (D.34) with the square modulus of the small signal amplitude derived in the previous section, thus writing

$$\begin{aligned} P(z) &\cong \mathrm{P}_0 \frac{|\beta(z)|^2}{1+\dfrac{\mathrm{P}_0}{\mathrm{P}_\mathrm{S}}\left(|\beta(z)|^2-1\right)}, \\ \beta(\tau) &= \frac{a(\tau(z))}{a_0} \end{aligned} \tag{D.39}$$

To check the validity of the previous formula we have developed an ad hoc numerical code to integrate the CARM equations refs. [19],[22],[25].
The dynamical systems accounting for the evolution of CARM devices is described by a set of equations coupling electrons and field. From the mathematical point of view the problem is that of solving a system of nonlinear ODE, consisting of four differential equations three of which accounting for the electron motion and the other for the complex field amplitude evolution inside the cavity.
The pivotal parameters characterizing the CARM dynamics are summarized by three dimensionless quantities: b, accounting for the auto-resonance, Δ, normalized detuning

$$\Delta = \frac{2\left(1-\dfrac{\beta_z}{\beta_p}\right)^2\left(1-\dfrac{\omega_R}{\omega}\right)}{\beta_\perp^2(1-\beta_p^{-2})} \tag{D.40}$$

and I_g normalized beam current, proportional to the beam current I_b and expressible in terms of ρ parameter as

$$I_g = \left[\frac{4\sqrt[3]{2}\left(1-\dfrac{\beta_z}{\beta_p}\right)}{\beta_\perp^2\left(1-\beta_p^{-2}\right)}\,\rho\right]^3 \tag{D.41}$$

The adopted numerical procedure foresees the use of a Runge-Kutta scheme for the electron dynamics, with the field amplitude kept constant during one discretization step. Furthermore, a finite difference method has been applied to evaluate the differential equation concerning the amplitude wave evolution, in which the crucial step is the careful average on the electron phase distribution and on the transverse velocity distribution in order to include correctly the effect of the beam qualities.
To study the effect of the particles velocity spread, starting form a fixed γ_0 beam energy and an α_0 pitch, a Gaussian distribution of the transverse velocity has been generated centred at the initial value of $\beta_{\perp 0}$.
For each particle we considered an ODE system characterized by a b($\beta_{\perp 0}^i$) and $\Delta(\beta_{\perp 0}^i)$ parameter and the integral average on the electron phase and

velocity distribution, has been evaluated by the use of a standard trapezoidal scheme.
Furthermore, the orbital efficiency has been obtained, by averaging the electron motion on the electron phase and velocity distribution, allowing to evaluate the CARM power growth.

The comparison between eq. (D.39) and the power evolution obtained via the numerical implementation are shown in Figs. D.5, D.6. The two curves compare fairly well; the use of these formulae for fixing the working points of a CARM device is therefore justified.

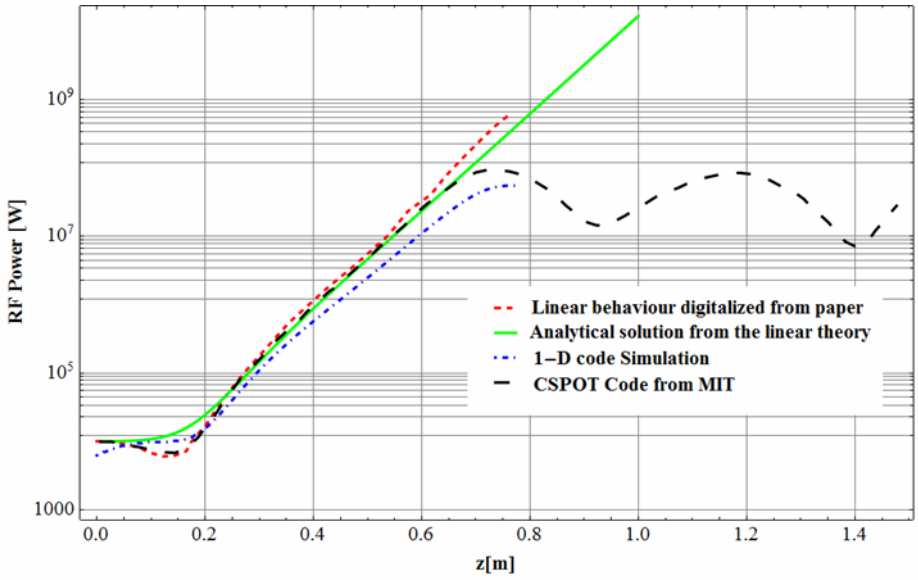

Figure D.5: The analytical growth linear rate of the signal compared with the numerical simulation.

The impact of the beam qualities on the output power have been reported in Fig. 1.5 of Ch. 2. We have successively commented how the associated demand for a high performance electron beam is met by an appropriate modelling of the gun.

We have so far shown that a wise application of the CARM theory and U-FEL scaling formulae developed in the past may provide a heuristic tool useful for CARM device design. Further "practical" consequences from our treatment will be drawn in the forthcoming section.

D.4 Transverse Mode Selection and Operating Configuration

The coefficient Ξ reported in eq. (D.32) summarizes quite a complicated expression including the transverse mode structure and should indeed be

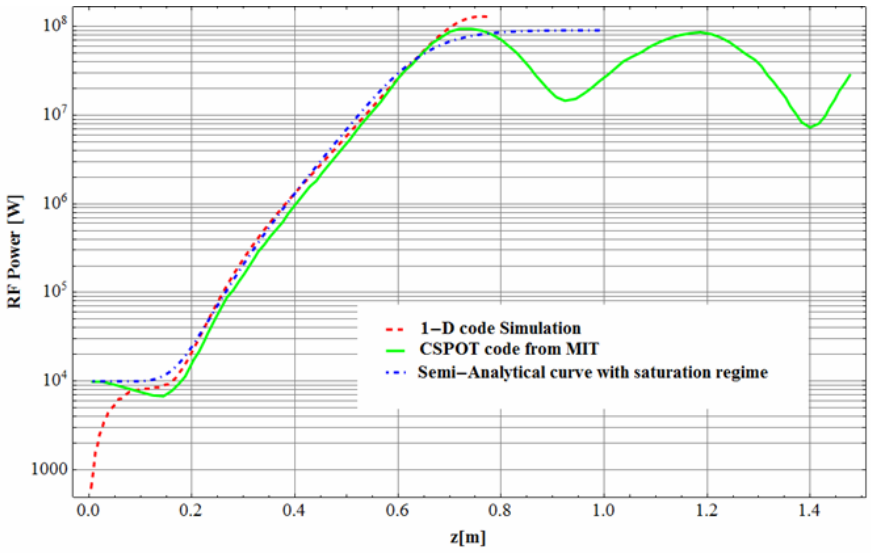

Figure D.6: The revisited semi-analytical formula from FEL compared with numerical code.

characterized by the indices m, n, l labeling the TE mode coupling and the overlapping integral with the beam itself.

This last quantity defines the filling factor, which, in turn affect the gain coefficient and the gain length as well. The problem becomes more and more serious when higher order modes are considered for lasing. In this case the relevant spatial distribution is not provided by a Gaussian, covering smoothly a transverse surface as for TE_{00} mode, but by a kind of circular corona which, as already stressed, demands for an appropriate shaping of the transverse structure of the e-beam to optimize the coupling. Accordingly the beam transverse distribution should be modeled as a thin circular corona.
In Figs. D.7 we have shown the linear part of the intensity evolution, along the z direction, together with the associated mode distribution. According to the previous remarks, it is not surprising that some collections of mode tend to grow in practically undistinguishable way.
We must emphasize that, although Figs. D.7 put the caveat that many transverse modes can be locked (thus creating problems of efficiency reduction), it provides a rather pessimistic view, since the growth has been determined through the root yielding the maximum rate.
The inclusion of the other roots and of the associated imaginary parts, is responsible for the slightly more complex behavior reported in Fig. D.8, in which the growth "degeneration" is removed.

In conclusion although the cavity is evidently over-moded (see Fig. D.1), the use of a convenient shaping of the annular electron beam may allow an efficient tool of mode selection, as further discussed in the following.

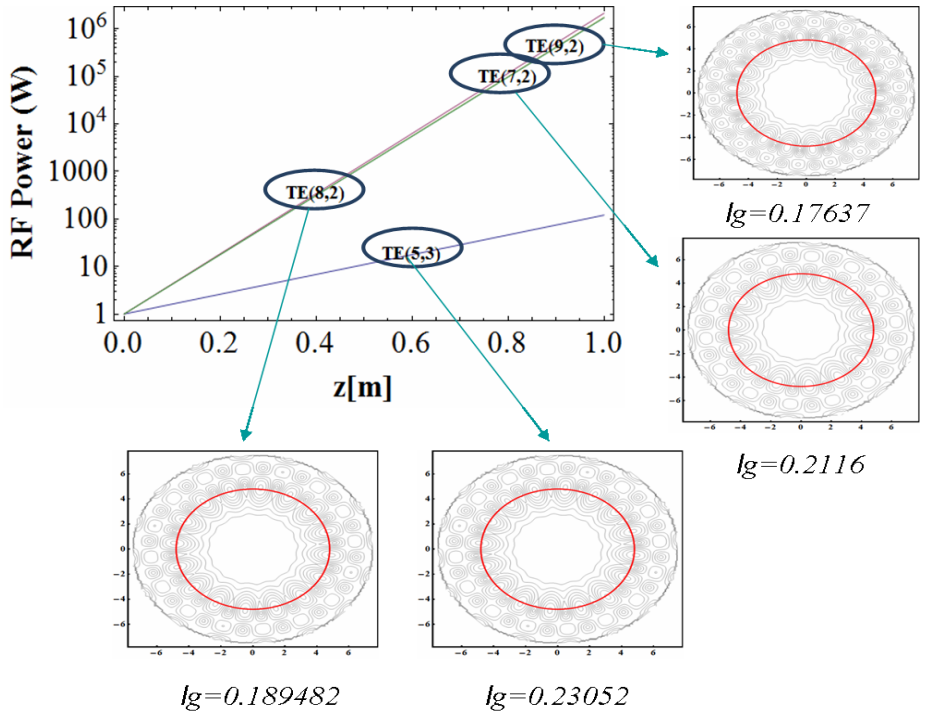

Figure D.7: Linear growth regime for different transverse mode distribution and associated gain length for a frequency resonance equal to *250 GHz*. The red circle represents the electron beam transverse distribution with radius R_b *=0.0048 m*, which is assumed to stay well inside the mode itself thus maximizing the filling factor.

Let us now come to the choice of the most convenient operating configuration. If we fix e.g. the output efficiency around *30%* consider the mode *5,3* and foresee an amplifier operating condition, with a modest input power of *0.1 W*, we can estimate a saturation length of few meters.

To overcome the problem of having a long section (including the high magnetic field) for the intensity growth in a single passage, the use of an oscillator configuration is foreseen. It allows the growth of the signal after a number of oscillations inside the optical cavity, which is placed in the centre of the Bragg reflector, where the magnetic field is flat.

The formalism we have exploited so far can be easily adapted to the oscillator, without any significant effort; by using the analogy developed with FEL devices we use the following relation yielding the equilibrium intensity intra-cavity power

$$I_e = \left(\sqrt{2}+1\right)\left(\sqrt{\frac{1-\eta_a(1+a)}{\eta_a(1+a)}G_M}-1\right) I_s, \qquad a = \frac{\eta_p}{\eta_a} \tag{D.42}$$

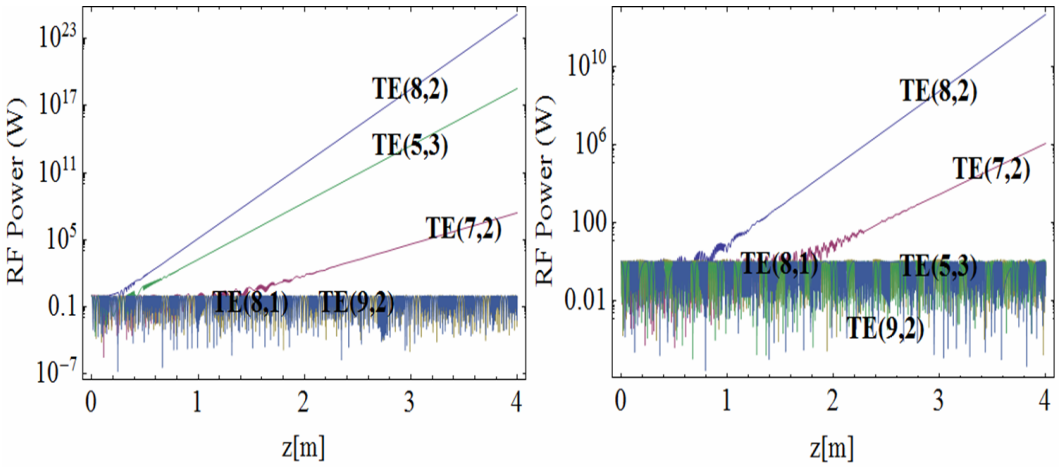

Figure D.8: Mode intensity evolution including the lethargic part changing the radiation frequency (f) and the annular beam radius (R_b): *a)* $f = 258\ GHz$, $R_b = 0.0048\ m$; *b)* $f = 250\ GHz$, $R_b = 0.0042\ m$.

where I_s is the CARM saturation intensity, I_e the equilibrium intracavity intensity, G_M is the maximum small signal gain and $\eta_{p,\,a}$ are the passive and active cavity losses.

We remind that by intensity we mean the power density, calculated on the operating mode surface.

The saturation intensity is defined according to the identity

$$\begin{aligned} &g_0 I_s \cong \eta\, P_E, \\ &P_E \equiv \text{electron beam power density} \end{aligned} \tag{D.43}$$

which yields

$$I_s = \frac{\eta p_E}{g_0} \tag{D.44}$$

and the active losses are linked to the cavity quality factor by

$$Q_c = \frac{2\,\pi\,\nu\,L_c}{c\,\eta_a} \tag{D.45}$$

with L_c being the cavity length and ν the frequency of operation.

A fairly practical mean to evaluate the small signal gain coefficient is provided by the use of eqs. (D.24), (D.25), (D.45), which yield the simple identity

$$g_0 = \frac{1}{3\,\pi\,\sqrt{3}}(\Gamma L)^3 \tag{D.46}$$

a small signal gain coefficient of the order of 1, requires $\Gamma L \cong \sqrt{3}\sqrt[3]{\pi} \cong 2.54$, a safe oscillator operation can be therefore foreseen by design an interaction length in such a way that

$$L \cong \frac{2.54}{\Gamma} \tag{D.47}$$

The cavity out-coupled power is simply given by

$$\begin{aligned} I_o &= \eta_a I_e = E(\eta_a, a, G_M)\ I_s, \\ E(\eta_a, a, G_M) &= \left(\sqrt{2}+1\right)\ \eta_a \left(\sqrt{\frac{1-\eta_a(1+a)}{\eta_a(1+a)} G_M} - 1\right) \end{aligned} \tag{D.48}$$

where $E(\eta_a, a, G_M)$ represents the extraction efficiency.

We can now exploit the previous formulae to derive a suitable Q factor for the CARM operation.

In Fig. D.9 we have reported the output efficiency vs. the active losses, for a cavity length of ***26 cm*** and an operating frequency around ***250 GHz***. The optimum output efficiency is therefore corresponds to active losses around *20%* and therefore (see Fig. D.10) to quality factor close to 10^4.

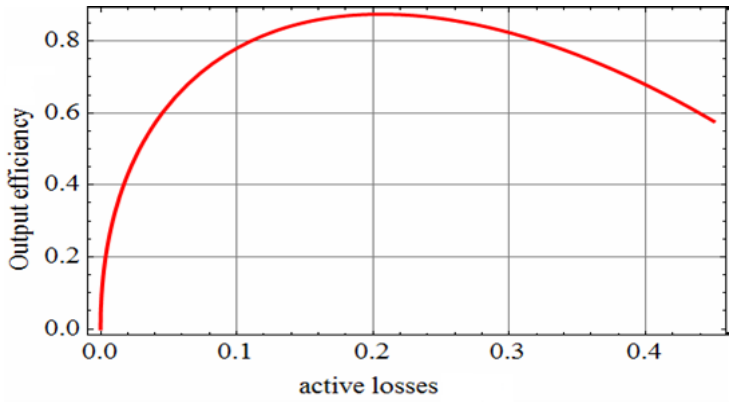

Figure D.9: Output efficiency vs. the cavity quality factor (a = *0.05*, I = *5 A*, L_c = *26 cm*, g_0 =*1.315*, $l_g \cong$ *0.11 m*, ω = *0.954* $\omega_+ \Rightarrow \nu$ = *250 GHz*).

If we require an output power of *1 MW* we are left with a corresponding intra-cavity power larger than *1.5 MW*. The passive losses, heating the cavity have been assumed to correspond to a *5%* of the active parts, and therefore the power to be cooled is below *100 KW*.

The Q-factor is larger than the value discussed in the first part of the document, but we can relax such a request by bringing it below $4 \cdot 10^3$, as shown in Fig. D.11.

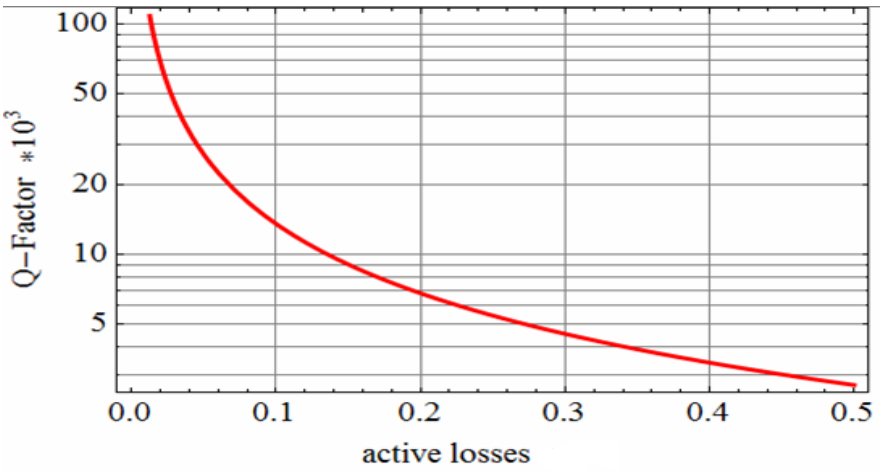

Figure D.10: Quality factor vs. the active cavity losses same parameters of Fig. D.9.

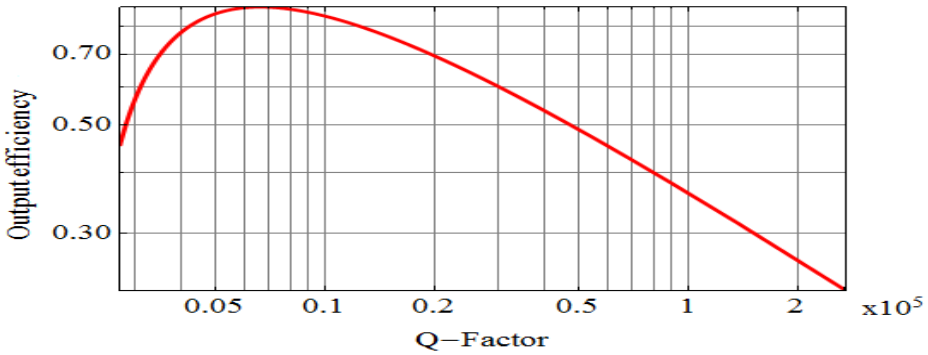

(a) Output efficiency vs. the Q-factor (same parameters of Fig. D.9).

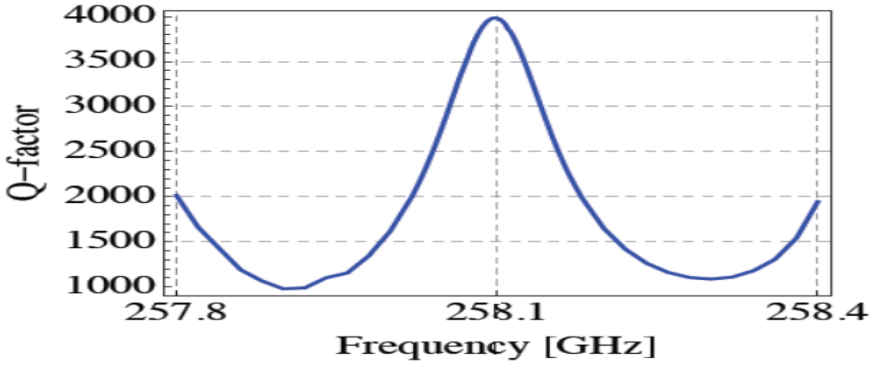

(b) Quality factor from mode competition and cavity optimization.

Figure D.11: Output efficiency, Quality factor, Cavity optimization.

Technical Addendum E

Modelling of a Bragg Resonator

As far as the coupled-mode theory is concerned, the theoretical formulation has been re-derived starting from Maxwell equations. Given a set of modes propagating along z, the system of differential equations that relate the longitudinal variation of direct (A^+) and reflected (A^-) wave amplitudes is

$$\begin{cases} \dfrac{dA_i^+}{dz} = -\left(j\beta_i - j\ \dfrac{\pi}{\Lambda} + \alpha_i\right) A_i^+ - j \sum_p g_1 G_{ip}\ A_p^- \\ \dfrac{dA_i^-}{dz} = -\left(j\beta_i - j\ \dfrac{\pi}{\Lambda} + \alpha_i\right) A_i^- - j \sum_p g_1 G_{ip} A_p^+ \end{cases} \tag{E.1}$$

where β, α and Λ are respectively the phase constant, the attenuation coefficient and the ripple period. The attenuation constants for smooth-wall circular waveguides reported in classical textbooks have been used. Nevertheless, at the present working frequency, the effective electrical resistivity is usually twice higher than the nominal one due to surface roughness, so actual losses are expected to be somewhat higher than the computed ones.

The term g_1 is the first coefficient of the Fourier series of an equivalent ripple profile with unitary amplitude; the coefficients of the most common profiles are summarized in Fig. E.1. The use of different ripple profiles produces negligible differences. Square and triangular profiles give rather similar reflectivity of the sinusoidal case, which has been adopted in the present design. Nevertheless, provided that the reflector length is fixed, they respectively achieve a target reflectivity with shallower and deeper corrugations than the sinusoidal case.

The coupling coefficients G_{ip} have the following expressions:

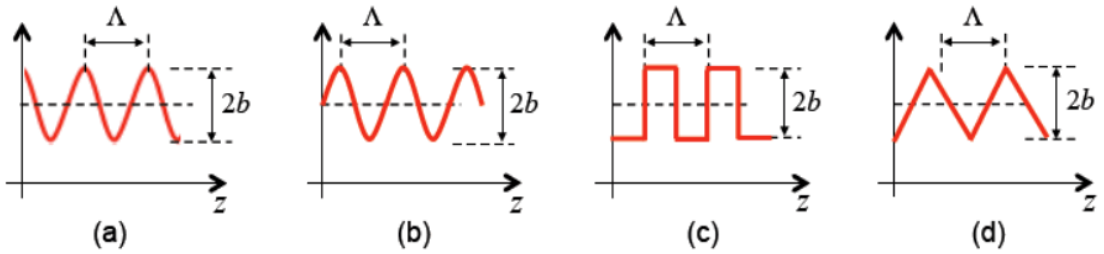

Figure E.1: (a) Cosine , (b) sine, (c) square and (d) triangle profiles.

$$\frac{k_b b_0}{a_0}\begin{cases} \dfrac{u'^4_{lm} - a_0^2 l^2\left(\dfrac{\omega^2}{c^2}+\beta^2_{lm}\right)}{2a_0^2\beta^2_{lm}\left(u'^2_{lm}-l^2\right)} & TE_{lm}-TE_{lm} \\ -\dfrac{\left(\dfrac{\omega^2}{c^2}+\beta^2_{lm}\right)}{2\beta^2_{lm}} & TM_{lm}-TM_{lm} \\ \dfrac{u'^2_{lm}\beta_{qp}(u'^2_{qp}-q^2)-u'^2_{qp}\beta_{lm}(u'^2_{lm}-l^2)}{\left(u'^2_{lm}-u'^2_{qp}\right)\sqrt{\beta_{lm}\beta_{qp}(u'^2_{qp}-q^2)(u'^2_{lm}-l^2)}} & TE_{lm}-TE_{qp} \\ \dfrac{u^2_{qp}\beta_{lm}-u^2_{lm}\beta_{qp}}{\left(u^2_{lm}-u^2_{qp}\right)\sqrt{\beta_{lm}\beta_{qp}}}\delta_{lq} & TM_{lm}-TM_{qp} \\ \dfrac{l\frac{\omega}{c}}{\sqrt{\beta_{lm}\beta_{qp}}\sqrt{u'^2_{lm}-l^2}}\delta_{lq} & TE_{lm}-TM_{qp} \end{cases} \tag{E.2}$$

where $k_b = \dfrac{2\pi}{\Lambda}$, ω is the angular frequency and c the speed of light; u_{qp} and u'_{qp} are the $p-th$ zeros of the Bessel function of the first kind and the $q-th$ order (J_q) and of its first derivative (J'_q), respectively.

This analytical model is derived under the following approximations:

- Ripple depth $b_0 \ll$ waveguide radius a_0,
- Ripple depth $b_0 \ll$ vacuum wavelength λ,
- Frequency range close to the Bragg condition: $\lambda_g = 2\Lambda$.

Only modes with the same azimuthal index interact and those very far from satisfying the Bragg condition give a negligible contribution. The summation can be thus truncated to N modes with the same azimuthal index of the working mode. Most authors take $N = 2$ that in the present case does not assure the convergence of results. For structures with an unperturbed radius of *7 mm*, the reflectivity at *250 GHz* exhibits larger variation when very few modes are included and, after about $N = 5$, it becomes almost constant. The design of reflectors and cavity for this CARM has been carried out taking *N=6*.

The systems of coupled equations defining each element of the resonator (two mirrors and a central smooth-wall waveguide) can be combined together. A single matrix is created with the coupling coefficients of each section so as to relate the wave amplitudes with their derivatives. Assuming a solution of the form $A\alpha e^{kz}$, an eigenvalue problem is obtained; from its solution the electromagnetic field in each point of the cavity is determined and parameters like ohmic losses and Q-factor can be calculated. This approach provides a more rigorous evaluation than the approximate formulas reported in literature.

The theoretical formulation has been implemented in a numerical code and validated against results from both literature and other numerical tools. The benchmark, carried out with respect to smaller structures than the one to be designed, has resulted in an excellent agreement, providing confidence on the reliability of the developed tool for resonators relevant to the present CARM project.

The reliability of the coupled mode theory is hampered by its intrinsic approximations. An alternative approach, currently under development, is the mode-matching method. The advantages the latter method offers are listed below:

- ⋆ It is a full-wave method (no physical approximations);
- ⋆ It probably allows the internal excitation of the cavity;
- ⋆ It is suitable for the study of particular geometries such as the advanced Bragg reflectors.

As a drawback, it is not very suitable to analyse sinusoidal corrugations.

Technical Addendum F

RF Components of the Cold Test

The RF cold test consists in the low power characterization of the resonant cavity and Bragg reflectors for the CARM. It will be performed with a vector network analyser provided with frequency extension modules to operate in the *WR-3* band (*220-325 GHz*).

The design of mode converters, able to transform the fundamental mode in rectangular waveguide to the operational TE_{82} mode in the oversized circular waveguide, is of utmost importance to check the cold performance of the beam-wave interaction region and presents unprecedented challenges as regards the oversized output waveguide that allows the propagation of almost *400* modes at *250 GHz*.

Two different conversion chains have been studied by means of CST Microwave Studio. The first one uses an in-line coupling corrugated converter, whereas the other is based on a sidewall coupling converter. Both cases require a final conversion from the TE_{81} to the TE_{82}, which is realized through a step-type mode converter; the performance of the latter has been calculated with an in-house mode-matching code too.

F.1 In-Line Coupling Corrugated Mode Converter

Fig. F.1 shows the model of the in-line coupling corrugated converter.

The initial transition, aimed at transforming the TE_{10} in *WR-3* rectangular waveguide into the TE_{11} in circular waveguide, is realized through a linear taper. A beat–wave converter follows, exploiting longitudinal and azimuthal corrugations to transform the TE_{11} into the TE_{81} mode. The inner radius is given by the expression

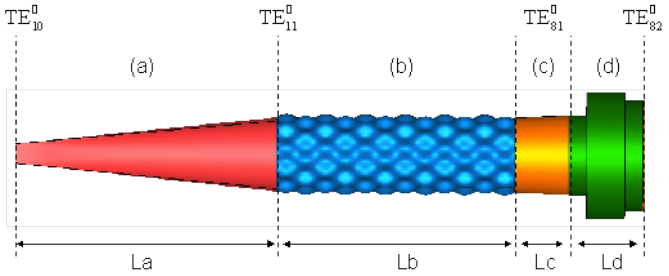

Figure F.1: Components of the first configuration: input transition from *WR-3* to circular waveguide (a), beat-wave converter (b), linear taper (c) and step-type converter (d). Radii at section outputs are from left to right: $R_a = R_b = 2.05\ mm$, $R_c = 2.21\ mm$, $R_d = 3.05\ mm$. Main modes at section ends are reported.

$$R(q,z) = R_a + 2a\cos(m_c q)\cos(b_c z) \tag{F.1}$$

where R_a is the average radius and $2a$ the amplitude of the corrugation. Conversion from an initial (i) to a final (f) mode occurs when the following beat conditions are satisfied

$$m_c = m_f \pm m_i$$

$$\beta_c = \beta_i - \beta_f$$

being m and β respectively the azimuthal eigenvalues and the propagation constants of the modes. In our case $m_f = 8$ and $m_i = 1$.

After a short taper, a step-type coupling converter increases the radial order of the mode. It consists of simple radius steps. The middle section acts as a cylindrical cavity allowing the propagation of the TE_{81}, TE_{82} and TE_{83}, whereas the output circular waveguide propagates the TE_{81} and TE_{82} modes. A preliminary setting was carried out with a mode matching code and the particle swarm optimization algorithm assuming perfect electric conducting walls. The simulations were repeated with CST Microwave Studio, resulting in a very good agreement. The output radius is $3.05\ mm$ and an output taper, which is not shown in Fig. F.1, increases the radius of the circular waveguide to $7.5\ mm$.

The overall length of the corrugated mode converter is $50\ mm$ and the efficiency about 80% for the presence of losses and spurious modes.

F.2 Sidewall Coupling Mode Converter

In the second configuration the TE_{81} mode is achieved using a sidewall coupling mode converter consisting in a cylindrical tube short-circuited at

one side and wrapped by a rectangular waveguide. The cylindrical cavity is excited with eight equally spaced rectangular holes.

The spacing of the rectangular holes must satisfy the following relation

$$n\lambda_g = 2\pi r_m \tag{F.2}$$

where n is the azimuthal mode number of the working mode (in our case $n = 8$), λ_g is the guided wavelength in the rectangular waveguide and $r_m = \dfrac{(R_1 + R_2)}{2}$ (see Fig. F.2a). The radius (R_3) of the cylindrical waveguide is set to make the guided wavelength of the TE_{81} mode equal to λ_g and avoiding the propagation of higher order modes such as the $TE_{10,1}$. The whole RF structure, reported in Fig. F.2a, where P_1 is the input port in rectangular waveguide and P_2 the output port in circular waveguide, has been simulated with a single model. In Fig. F.2b, the electric field amplitude at *250 GHz* along the structure is shown. The electric field does not change its polarization and the pattern at the output corresponds to the TE_{82} mode.

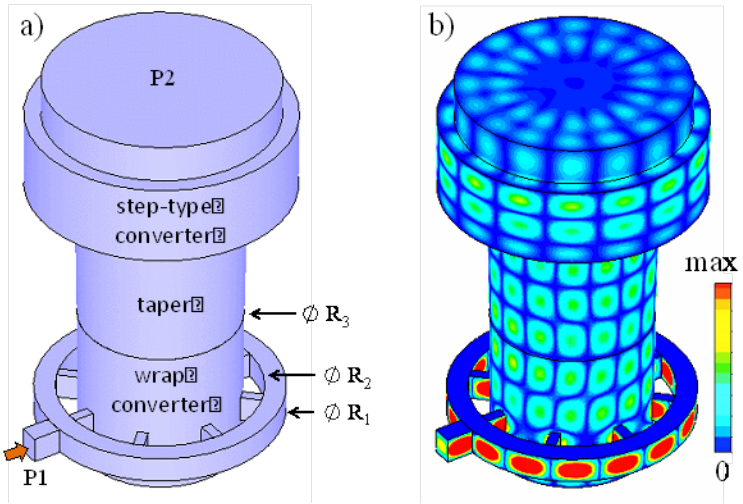

Figure F.2: *a*) Schematic of the sidewall converter: the input rectangular waveguide has size $a \times b = 0.7 \times 0.55\ mm^2$, while the rectangular holes are $a \times b/2$; $R_1 = 3.25\ mm$, $R_2 = 2.69\ mm$, $R_3 = 2.14\ mm$, cavity length = *4 mm*, distance of the short circuit from holes = *1.35 mm*. *b*) Pattern of the electric field at *250 GHz*.

Fig. F.3a shows the reflection and transmission of the working mode versus frequency for a device optimized at *250 GHz* while in Fig. F.3b the amplitude of the parasitic modes is depicted. The efficiency of the converter is about *83%* and the overall length without taking into account the flanges and the final taper is only *13.14 mm* with output radius of *3.05 mm*.

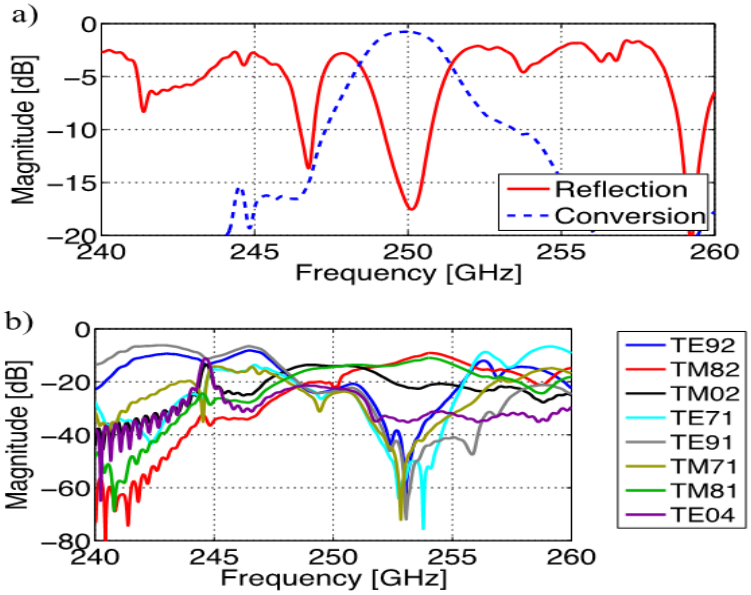

Figure F.3: *a*) Reflection of TE_{10} in rectangular waveguide and conversion into the TE_{82}; *b*) Undesired modes with the highest amplitude at the output.

F.3 Output Taper

The transition between the output radius ($R_d = 3.05\ mm$) of the converters and the radius of the cavity ($R = 7.5\ mm$) is foreseen using a linear taper.

Available computational resources only allowed the simulation of a taper with a length of *25 mm* and a maximum output radius of *5.5 mm*, providing a transmission efficiency of about *0.22 dB* and a reflection coefficient lower than *-40 dB*. Either an improvement of the computational capabilities or the use of different numerical methods are required to design a taper with the foreseen output radius of *7.5 mm* and assessing the performances of exponential and Chebyshev profiles.

F.4 Construction and Ohmic Losses

The construction of these high frequency components requires a mechanical accuracy better than $\pm$ *2* μm. Therefore the simplest geometry has to be preferred and high precision micromachining technique has to be adopted for the construction. Copper electroforming, allowing to reach dimensional tolerances up to *1* μm and surface roughness comparable to the skin depth of the copper at $f = 250\ GHz$, could enable the fabrication of the prototypes. Reliable simulation results in term of ohmic losses are obtained by assuming a model having virtual walls with half the conductivity of the real metal to compensate for imperfection and surface roughness effects. Our simulations consider aluminum, whose electrical conductivity of

$\sigma = 35.6 MS/m$ allows the emulation of RF losses in realistic components made of copper ($\sigma = 59.7\ MS/m$).

Technical Addendum G

Vacuum System

Any free electron based device, used to generate coherent radiation, requires an operation in vacuum due to the presence of charged particles, for which we need to guarantee the longest free mean path. Moreover the presence of delicate electron emitter surfaces and the transport of high power radiation demand the design of an appropriate vacuum system.

The classical equations to be used to evaluate the pressure behaviour as function of time are:

$$P = -\frac{V}{S_e}\left(\frac{dP}{dt}\right) \tag{G.1}$$

where V is the volume to be pumped and S_e is the effective pumping speed related to the pumping speed of the pump S_P and to the conductance C of the evacuation pipe by the relation

$$\frac{1}{S_e} = d\frac{1}{S_P} + \frac{1}{C} \tag{G.2}$$

From equation (G.1) we can evaluate the value of the final pressure P_2 as function of the starting pressure value P_1 and the other physical parameters as

$$P_2 = P_1 \exp\left[-\frac{S_e}{V}\left(t_2 - t_1\right)\right] \tag{G.3}$$

The simple equation (G.1) must be corrected by the fact that all materials undergo to the outgassing effect expressed by the outgassing rate Q [Pressure·Volume/time]. The pressure inside a vacuum chamber disconnected from the pump, increases to an asymptotic value P_{Lim} following the experimental behaviour

$$P = P_{Lim}\left\{1 - exp\left[-\left(\frac{Q}{VP_{Lim}}\right)t\right]\right\} \tag{G.4}$$

that corresponds to a pressure variation rate given by

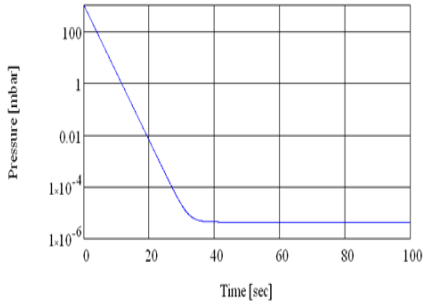

(a) $Q = 1.3 \cdot 10^{-3}$ $Pa\ l/s$.

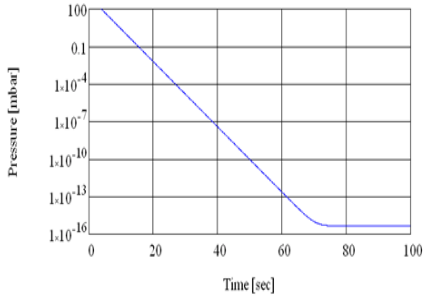

(b) $Q = 1.3 \cdot 10^{-13}$ $Pa\ l/s$.

Figure G.1: Pressure behaviour in a vacuum chamber of $V = 500\ l$ and a pumping speed of $S_e = 300\ l/s$ an for two different outgassing rates

$$\frac{dP}{dt} = \frac{Q}{V} \exp\left[-\frac{Q}{VP_{Lim}}t\right] \tag{G.5}$$

During the pumping process the equations (G.1) and (G.5) compete one to each other and only a proper evaluation of the outgassing rate of all the materials contained in vacuum chamber, and of the chamber itself, can return an accurate value of the vacuum final pressure. Also the conductance should be suitably evaluated in order to not reduce too much the pumps pumping speed. A composite system, as a CARM or any free electron based laser, require an appropriate simulation in order to evaluate the correct pumping system, but an estimation of the behaviour of the pressure as a function of time, as reported by equations (G.1) and (G.5), is reported in Figs. G.1a, G.1b.
The parameters utilised for Fig. G.1a are a volume of $V = 500$ litres made of stainless steel for which we have an outgassing pumping rate of about $3.3 \cdot 10^{-8}$ $[Pascal \cdot litre \cdot second^{-1} \cdot cm^{-2}]$ that leads to a value of $Q = 1.3 \cdot 10^{-3}$ $[Pascal \cdot litre \cdot second^{-1}]$ having considered an internal surface of the vacuum tank of $4 \cdot 10^4\ cm^2$. For Figure G.1b it has been hypothesised a vacuum chamber material without outgassing, having, thus a $Q = 9.9 \cdot 10^{-14}$. For both the figures the effective pumping speed, that includes the conductance as stated in equation (G.1), has been set at $S_e = 300$ $[litres/second]$.

The Figure G.1 analysis tells us that the outgassing rate of the surfaces of the vacuum chamber and of the all elements in it contained is relevant for the estimation of the final pressure value.

The CARM device can be considered as casted by four essential parts as viewed by the vacuum technology point of view. The first element is the electron gun; the second is the radiation cavity and more in general the interaction region; the third is the depressed collector section and the last is the high power microwave transport region after the diamond window to the target.

The electron gun is the most demanding element of the CARM as far as the vacuum technologies is concerned, requiring the lowest pressure values and the highest pumping speed at the same time. This is due to the fact that the thermionic electron emission process requires ultra high vacuum conditions in order to not poison the cathode emitter. Scientific literature says that the lower the pressure the better the emitting results; typical values are in the range of 10^{-9} mbar or better. The second issue for the electron gun is the possibility to recover the proper pressure values in a short time, when anomalous outgassing events occur. These events are mainly related to the electron beam hitting, or scraping, accidentally, the vacuum tank.

The interaction region, consisting in the waveguide cavity, is the second element of the CARM, where the electron kinetic energy is converted in electromagnetic radiation. The electron beam transport do not requires a pressure as low as that in the gun section, but a correct gradient must be established among all the section downstream the electron gun. The interaction region is directly connected to the electron gun and thus its pressure value should not be much different from that of the gun, in the range of 10^{-8} mbar for instance.

The depressed collector is the element where the energy of the exhausted electron beam is recovered both as radiofrequency and as charge. There are some solutions to increase the separation between the depressed collector and the upstream regions, such as a diaphragm to eliminate the backstreaming of electrons from the dump into the ultra-high-vacuum region of the beam line and the gun chamber. When such solutions are adopted, pressure values in the range $10^{-5} - 10^{-6}$ $mbar$ are suitable for the dumping operation.

The light pipe for the radiation transport is connected to CARM device through an optical window that separates it from the ultra-high vacuum region being capable to sustain the high power level of the electromagnetic field. Radiation in the millimetre and sub-millimetre spectral range presents the characteristics to be absorbed by the rotational modes of the molecules in air, with a particular reference with water vapour. To reduce this absorption effect the radiation transport channel can be evacuated, but pressure values in the range 10^{-3} $mbar$ are, in this case, sufficient to manage the issue.

The exposed analysis is very preliminary because a proper simulation ought to include a good knowledge of all the elements placed under vacuum, the nature of the materials of their surfaces and their baking features. In any case a rough estimation of the needs of a vacuum pump system can be done on the basis of this note, including a budgetary evaluation of the costs. As expressed the most demanding element of the CARM is the electron gun for which a Ultra-High Vacuum is required connected with a high pumping

rate and a fast recovery system; a possible scheme is given by one or two of the following elementary block:

- 1 Dry primary pump with at least *500 l/min* ($1 \cdot 10^{-3}$ *mbar*)
- 1 Turbo pump with *350 l/sec* ($1 \cdot 10^{-10}$ *mbar*)
- 1 Ion pump with *400-500 l/sec* with sublimation ($1 \cdot 10^{-11}$ *mbar*)

As far as the waveguide cavity element the previous block can be left as it is with the exception of the ion pump that in this case do not need the sublimation cryo-panel. The price of this version of the ion pump can be lowered down of about *20%* (see Table G.1 below).

The depressed collector section is a "dirty" part of the CARM and requires an adequate vacuum system avoiding the use of any of the ion pumps; thus the scheme can be given by one or two of the following elementary block:

- 1 Dry primary pump with at least *500 l/min* ($1 \cdot 10^{-3}$ *mbar*)
- 1 Turbo pump with *350 l/sec* ($1 \cdot 10^{-10}$ *mbar*)

Concerning the high power radiation transport system this will consist of a series of pipes with some mirror chamber to be designed. Due to the separation from the CARM, by means of a window, and to the values of pressure discussed before, the pumping scheme can be casted by a series of the following block, depending on the total length of the pipes:

- 1 Dry primary pump with at least *500 l/min* ($1 \cdot 10^{-2}$ *mbar*)
- 1 Turbo pump with *80 l/sec* ($5 \cdot 10^{-10}$ *mbar*)
- 1 Ion pump with *70-80 l/sec* ($1 \cdot 10^{-11}$ *mbar*)

From the previous considerations it can be concluded that a very basic estimation for the costs of a vacuum system of the CARM starts from about *100.000* € (plus VAT) as can be deduced from the Table G.1 reported below. This minimal evaluation may rapidly rise with the growth of the system complexity.

Table G.1: Cost evaluation of the single CARM blocks

E-gun Block	Dry Pump Turbo Pump Ion Pump	7.000 € 10.000 € 18.000 €	35.000 €
Cavity Block	Dry Pump Turbo Pump Ion Pump	7.000 € 10.000 € 13.000€	30.000 €
Depressed Collector Block	Dry Pump Turbo Pump	7.000 € 10.000 €	17.000 €
Radiation Transport Block	Dry Pump Turbo Pump Ion Pump	5.000 € 7.000 € 5.000 €	17.000 €
Total			99.000 €

Technical Addendum H

RF Vacuum Window for a 250 GHz, 200 kW CARM Experiment

In the CARM project a challenging problem appears to be the efficient launching of the generated high power radiation outside the vacuum tube. If the output Quasi Optical Converter (QOC), which transforms the cavity mode into a linearly polarized Gaussian beam, is located outside the vacuum region, the high-power RF vacuum window will be positioned in an oversized circular waveguide, where the electromagnetic pattern corresponds to the operating mode generated by the resonant cavity. The vacuum window is aimed at separating the high vacuum present inside the CARM from the external atmospheric air.

In the first step of the design, with maximum RF pulse duration of *50* μs and output RF power of *200 kW* a suitable dielectric for the vacuum windows of a high power microwave source prototype could be the polycrystalline aluminum oxide (Al_2O_3), also known as alumina [19], often adopted in applications with short pulses and very high power. This material exhibits many satisfactory properties tailor suited for the present purposes. It has low dielectric losses, high dielectric strength, high mechanical strength and an excellent thermal shock resistance; it can bears high processing and operating temperature and its thermal expansion coefficient matches with metallic materials; moreover it has low cost, ease of metallization and non-toxic properties. Then it can withstand up to *900* $^{\circ}C$ for the cycled vacuum baking useful for the effective cleaning of the dielectric surfaces and to obtain an ultra- high vacuum of order 10^{-10}.

Another dielectric, which is often employed in CW operation at lower frequencies (*3-10* GHz), is the Beryllium Oxide (BeO). It presents a higher thermal conductivity but it is a toxic material and not particularly strong mechanically. Among the remaining materials crystal quartz and silicon are low-loss dielectrics employed in vacuum windows for submillimeter and mil-

limeter waves. These dielectrics provide low-loss properties using a quarter wave transformer on both the sides of a silicon wafers [20] and anti-reflection layers for a crystal quartz [21]. These vacuum windows require a more careful evaluation in our application because they could suffer from a limited power handling capability and a too low fracture stress (i.e., the stress exerted on the edge by an overpressure in a circular disk of dielectric). In any case the RF design needs the characterization of the chosen material for frequencies in the range *230-280 GHz*.

Regardless of the material, the vacuum window assembly is based on a single cylindrical disk of dielectric brazed on a stainless steel flange. The design criteria to minimize the reflectivity consist in setting the thickness of the dielectric as a multiple of $\frac{\lambda}{2}$ (half a wavelength in the dielectric) at the operating frequency. The number of half wavelengths must be sufficient to bear the overpressure between the vacuum and the pressurized region. The best choice is a thin thickness to reduce the losses on the dielectric but large enough to avoid that the exerted stress exceeds the fracture stress. In our experiment for an output power of *500 kW* a disk with diameter of *50 mm* and thickness in the range *0.8-1.6 mm* meets the previous requirements.

The properties of alumina are well known at $f = 19\ GHz$ but the main risk at higher frequencies is an increase of dielectric losses. Taking as example the alumina *995* with a relative permittivity of *9.4*, at $f = 250\ GHz$, $\frac{\lambda}{2}$ is about *0.2 mm*, therefore a suitable thickness will be within the interval from $4\left(\frac{\lambda}{2}\right)$ to $8\left(\frac{\lambda}{2}\right)$.

The expected power deposition is given by the following equation

$$P_{loss} = \frac{[\pi f\,(1+\varepsilon)\tan\delta\ P_{RF}\ d]}{c} \tag{H.1}$$

where c is the speed of light in vacuum, f the frequency, ε the relative permittivity, tanδ the dielectric loss tangent, P_{RF} the injected power and d the thickness of the disk. Assuming a thickness $d = 0.6\ mm$ and using at $f = 250\ GHz$ the properties measured at microwaves ($\tan\delta = 10^{-4}$, $\varepsilon = 9.4$), the evaluated deposition power for $P_{rf} = 500\ kW$ is about 830 W ($P_{loss} = 0.016 \times P_{rf}$). With a more realistic thickness ($d = 1\ mm$), the deposition power becomes *1250 W*.

In the second phase of the experiment (CW operation with pulses duration of *500 ms* and output RF power of *0.5 MW*) the configuration of the vacuum window will be similar replacing the alumina, unusable in CW operation, with CVD-diamond. CVD-diamond, apart from its cost, has superior characteristics and nowadays it is adopted as output window in gyrotrons and vacuum barrier in Electron Cyclotron Resonance Heating (ECRH) systems in the frequency range *100-170 GHz*. Its main properties

are: very high thermal conductivity (*1800* $Wm^{-1\circ}K^{-1}$), five times that of copper, heat transfer coefficient of *12* $kW/(m^2K)$ to the cooling water, low thermal expansion coefficient, very low values of dielectric loss and high average fracture toughness (*8.5* $\pm$ *0.4* $MPa/m^{1/2}$) [22], kept even at high temperature. The high fracture stress , despite its decrease with disk thickness and grain size, makes the CVD-diamond window capable to bear a high pressure without failure also utilizing a thin disk of dielectric. In the last *20* years a great progress in the synthesis technology has made possible to manufacture large size of very high quality CVD-diamond window disk with loss tangent of 10^{-5}. Nowadays a disk of CVD-diamond (the output vacuum window of the *170* GHz gyrotrons) with diameter *120* mm and thickness of *2.25* mm [23], is the largest ever made. Usually the diameter of the CVD-diamond will be higher than the window aperture so the periphery of the disk is directly cooled by water. Typical flow speeds of the cooling water are included in the interval *12-18* m^{-1} for an output RF power of *500* kW. The properties of the CVD-diamond have been investigated in the frequency range *110-170* GHz and the extension of the characterization at higher frequencies is essential for the design of the CVD-diamond vacuum window for a CARM at f = *250* GHz. A possible assembly [24] is constituted by two Inconel cylinder bonded by aluminum braze from both sides of the metalized CVD-diamond disk edge. Inconel tubes are welded to a stainless flange. Assuming a relative permittivity of *5.6*, the value of $\frac{\lambda}{2}$ is about *0.25* mm; the thickness of the disc with diameter of *60* mm, which satisfies both design criteria and feasibility, will be included in the range from $3\frac{\lambda}{2}$ (*0.75* mm) to $5\frac{\lambda}{2}$ (*1.25* mm).

Technical Addendum I

Single Stage Depressed Collector for a CARM

A not secondary problem, to fulfil the request of sustainable efficiency of the device, is that of recovering the exhausted electron beam after the interaction. In high power vacuum electron devices the electron beam recovery for collecting spent electrons, is essential to increase the efficiency by using a single step or multistage depressed collector. The advantages of High Power RF source with depressed collector are the following:

- Increase the total efficiency of the tube;
- Reduction of the power of the main power supply;
- Reduction of the thermal load of the collector.

In a CARM (a microwave sources based on the induced cyclotron radiation of electron oscillators moving along a homogeneous magnetostatic field) the recovery voltage (U_{rec}) is limited to that corresponding to the minimum possible electron energy at the output of the interaction region to avoid the reflection of electrons from the collector. The minimun energy is

$$eU_{rec} = m\left(\gamma_{min} - 1\right)c^2 \tag{I.1}$$

Using a single stage depressed collector the total efficiency writes

$$\eta_{total} = \left(\frac{\Delta E}{e\,U_0}\right) f_{rec} \tag{I.2}$$

where ΔE is the energy subtracted to the electrons via CARM interaction, U_0 is the accelerating voltage or anode voltage interaction and f_{rec} is the recovery factor which reads

$$f_{rec} = \frac{1}{1 - \dfrac{U_{rec}}{U_0}} \tag{I.3}$$

In Fig. I.1 we have reported of sketch of the whole device including the depressed voltage collector ($U_0 - U_{rec}$) applied between collector and

cathode and the anode voltage (U_0) between anode e cathode electrode.

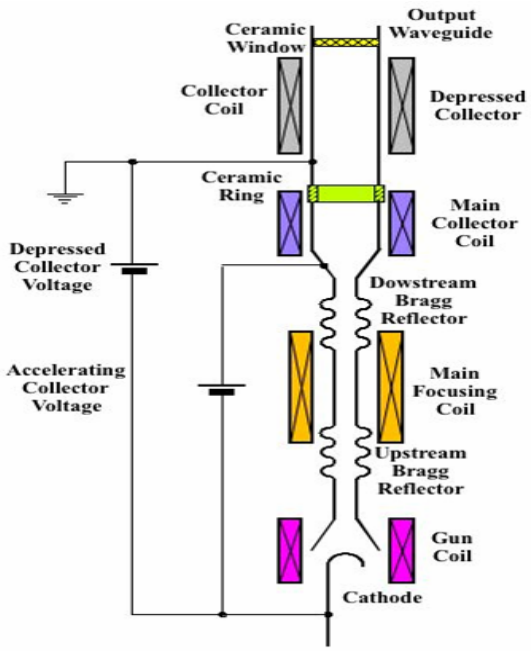

Figure I.1: CARM simplified schematic with single-step depressed collector for energy recovery.

The beam recovery system consists of a decelerator and of a single or multistage beam collector. The electron energy spread limits the applicable deceleration and requires a multistage depressed collector with many power supplies in order to optimise the system efficiency. For our CARM with low longitudinal spread probably the simpler and less expensive solution with only one stage.

In any case the CARM feasibility study is now in the initial phase and the choice between single or multistage depressed collector will be taken subsequently. So in Fig. I.2 is shown a depressed collector multistage to understand better the different parts of the recovery system.

The main parts of the multistage depressed collector are:

1. copper electrodes mounted between ceramic rings to provide electrical insulation while completing the vacuum envelope. The electrodes are coated with a thin layer of carbon of *2* to *5* micron thickness to minimize the adverse effect of secondary electrons. Carbon provides a good surface for low secondary yield, in fact compared with many other materials (copper, titanium carbide, graphite etc) presents the lowest secondary electron emission yield versus the primary electron energy. Each electrodes contains passages for water cooling.

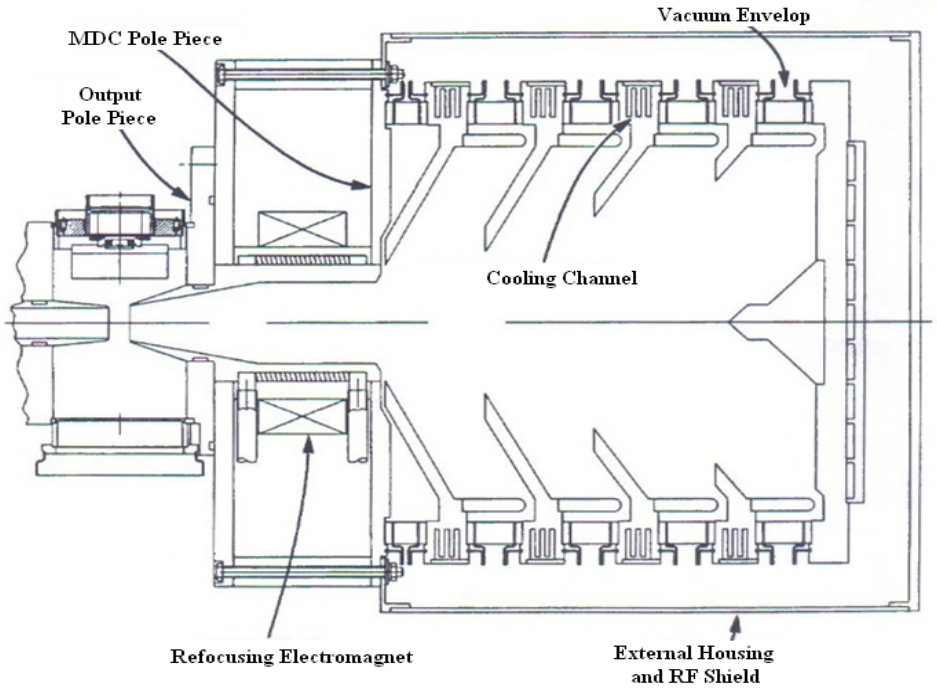

Figure I.2: Multistage depressed collector with 5 electrodes.

2. cooling system: each electrodes contains passages for water cooling. The collector need to be cooled using techniques with a sufficient heat exchange coefficient, usually hyper-vapotron cooling is utilized.

3. Magnetic sweeping coils: and relative power suppliess

Suitable sweeping systems performed with several coils located around the collector, powered with powerful power supplies, allow to sweep the spent electron beam along the surface of the collector. These tecniques, already adopted for the gyrotrons, ensure a nearly uniform distribution of the electron beam on a larger surface area. The commonly utilized approaches are combined longitudinal and transversal field sweeping systems as sketched in Fig. I.2

I.1 Simulation of a Depressed Collector

After the electron cyclotron interaction in the cavity, the spent electron beam has to be absorbed in the collector. The collector can be manufactured using pure or dispersion strengthened copper, known as Glidcop. It is a family of copper based metal matrix composite (MMC) alloy mixed primarily with aluminium oxide ceramic particles. The addition of a small amount of aluminium oxide has minuscule effects on the performance of copper (such as small decrease in thermal and electrical conductivity), but greatly increases the material's resistance to thermal softening and enhances

strongly the elevate temperature strength. In this phase of the design we don't foresee the cooling system of the collector with water flow aligned perpendicular to grooves. It is necessary to provide the ceramic insulator to apply the depression voltages. For long lifetime, the maximum acceptable wall loading for pure copper is *500* W/cm^2 and *1000* W/cm^2 for Glidcop due to the different materials' tensile strengths. To guarantee long lifetime of the collector, a limited average wall loading must be achieved. The Glidcop (dispersion strengthened copper) allows a more compact collector design with respect to radius and axial length. The loading must be smoothly distributed along the collector surface length utilizing collector coils for the sweeping along the longitudinal dimension of the collector. Power supplies are required for the coils which absorb high current and hence a suitable water cooling of the coils will be necessary.

Assuming a CARM with a maximum RF output power of *500 kW* and efficiency about *33%*, the maximum power of electron beam dissipated on the collector will be *1.5 MW* in the worst conditions without the energy recovery on the collector and if all the beam electron energy will be dissipated on the collector. A average wall loading of about *0.30* kW/cm^2, much lower than the maximum value of *1* kW/cm^2 (Glidcop), has been calculated for a collector with radius *20 cm* and long *50 cm*. assuming the beam electron energy uniformly distributed along the surface. A low wall loading ensures long lifetime of the collector. The applied depression voltage requires an electrode coated with a thin layer of carbon of *2* to *5* micron thickness in the regions of impingement to minimize the adverse effect of secondary electrons. The electrodes must contain the passages for water cooling. It is necessary to provide the ceramic insulator to apply the depression voltage on the collector.

A preliminary evaluation of the overall cost of a depressed collector (DC) is indicated in the following Table.

Table I.1: **Evaluation of the overall cost of a DC**

Glidcop collector (material, processing and production)	110 *K€*
Coils and power supply	100 *K€*
Insulator and electrode	10 *K€*
Total Cost	210 *K€*

The Glidcop is much expensive than the copper but with a maximum wall loading of about *1000* W/cm^2 allows a more compact collector design with respect to the radius and the axial length. Using suitable codes to study the trajectory of electron beam in the collector region it is possible to evaluate the efficiency with one or two stage of depressed collector and

the maximum value of depressed voltages.

Technical Addendum J

The CARM Control System

The design of a control system starts from the definition of the device to be controlled. This is important for non- commercial devices, whose specifications should be indicated to the manufacturer: it's important to define the physical quantities that need to be monitored, the format of the data and the interface to be used for data communication between components of the control system.

In order to design the control system, the CARM device was divided in "blocks", and the requirements of each block was described, taking into account the interconnection and the data transfer between blocks.

For each block a certain number of data to be monitored was indicated and the physical and logical format of the interface was defined.

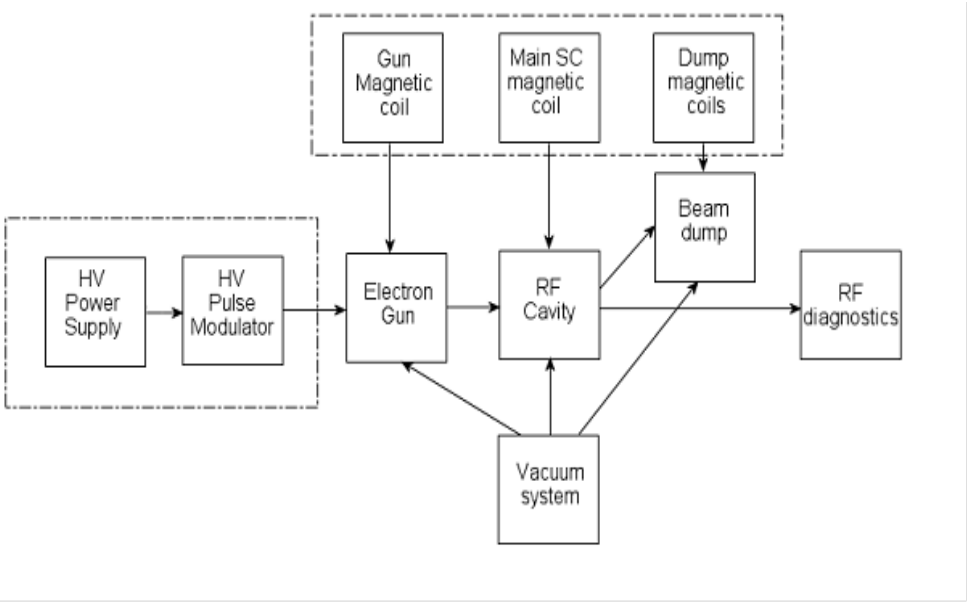

Figure J.1: CARM device divided in "blocks".

J.1 Power Supply/Modulator

The power supply/modulator assembly will be custom-built according to the provided design, it is then possible to ask for a certain number of controls and readouts to be available to the user through the preferred interface in the required format. All control units should be able to be operated both in "local" and in "remote" mode. A local-remote switch should be places on the physical controls and should include removable keys. It is necessary that all settings could be operated both on local and remote mode. The standard configuration gives priority to remote controls over local control, when remote mode is selected.

A certain number of parameters need a fast feedback to switch off the device is critical conditions are detected. At the same time a "slow" signal should be generated, to be acquired by the CARM control system, to be visualized on the synoptic graph.
Some fast interlock should be made available to shut off the device when critical conditions occur in other components of the CARM device.
Data will be managed by the embedded electronic and will be controlled/read by global control system through the required interface
(*RS232/RS485/IEEE488* , in the following referred to as **Digital**").

Table J.1: **Power supply/modulator controls**

Parameter	**action**	**Time**	**Data type**	**Interface**
ON/OFF switch	set	slow	Digital (boolean)	Digital
ON/OFF switch	read	slow	Digital (boolean)	Digital
Current	set	slow	Digital (numeric)	Digital
Current	read	slow	Digital (numeric)	Digital
Voltage	read	slow	Digital (numeric)	Digital
Current ripple	read	slow	Digital (numeric)	Digital
Voltage ripple	read	slow	Digital (numeric)	Digital
Rise time	set	slow	Digital (numeric)	Digital
Rise time	read	slow	Digital (numeric)	Digital
Pulse duration	set	slow	Digital (numeric)	Digital
Pulse duration	read	slow	Digital (numeric)	Digital
Repetition rate	set	slow	Digital (numeric)	Digital
Repetition rate	read	slow	Digital (numeric)	Digital
Temperature	read	slow	Digital (numeric)	Digital
Discharge detection	read	slow	Digital (numeric)	Digital
General failure	read	slow	Digital (numeric)	Digital
Interlock input (1 to 8)	set	fast	Analog	TTL

Other parameters could be available on the digital interfaces:

- Total number of digital ports: *2* **Digital**,

- Analog input (interlock): *8* .

J.1.1 Magnetic Coils

The system includes *3* magnetic coil systems, used to control the electron beam along its path: gun magnetic coil, main superconducting coil and beam dump coil.

Each of the coil is powered by a commercial power supply working in current mode; the gun and the beam coils are cooled by an industrial chiller, while the SC coil makes use of a commercial cryocooler. Fast electronic is required to detect any failure that could modify the required value of the magnetic field (causing the loss of the e-beam). For this reason a fast analog readout of the Magnet power supply current is required, to be used to drive the Power supply/modulator interlock.

Table J.2: **Magnetic Coils**

Gun and beam dump magnetic coil (each)				
Parameter	**Action**	**Time**	**Data type**	**Interface**
P.S. ON/OFF switch	set	slow	Digital (boolean)	Digital
P.S. ON/OFF switch	read	slow	Digital (boolean)	Digital
P.S. Current	set	slow	Digital (numeric)	Digital
P.S. Current	read	slow	Digital (numeric)	Digital
P.S. Current	read	fast	Analog	→ to custom electronics → interlock
Chiller				
Parameter	**Action**	**Time**	**Data type**	**Interface**
Chiller ON/OFF switch	set	slow	Digital (numeric)	Digital
Chiller ON/OFF switch	read	slow	Digital (numeric)	Digital
Chiller Temperature	set	slow	Digital (numeric)	Digital
Chiller Temperature	read	slow	Digital (numeric)	Digital
Coooler flux	read	slow	Digital (numeric)	Digital
Coil thermocouples (8)	set	slow	Analog	–> to ADC

Table J.3: **Magnetic Coils**

SC magnetic coil				
Parameter	**Action**	**Time**	**Data type**	**Interface**
PS ON/OFF switch	set	slow	Digital (boolean)	Digital
PS ON/OFF switch	read	slow	Digital (boolean)	Digital
PS Current	set	slow	Digital (numeric)	Digital
PS Current	read	slow	Digital (numeric)	Digital
PS Current	read	fast	Analog	–> to custom electronics –> interlock
Crycooler ON/OFF switch	set	slow	Digital (numeric)	Digital
Crycooler ON/OFF switch	read	slow	Digital (numeric)	Digital
Fluid Temperature	read	slow	Digital (numeric)	Digital
Fluid Pressure	read	slow	Digital (numeric)	Digital
General Alarm/warning	read	slow	Digital (numeric)	Digital

Other parameters could be available on the digital interfaces:

- Analog output: (*16* thermocouples + *3* current): *16* → to a *24* **channel Digital-Controlled ADC**;
- Fast analog outputs: *3* current fast readout to **custom electronics** (compares with correct value of the current and in case of failure sends a TTL signal to Power supply/modulator interlock);
- Total number of digital ports: *5 + 1* **Digital**.

J.1.2 RF Cavity

A certain number of diagnostic will be hosted in the interaction area:

- Electron beam position and current monitors
- RF radiation monitors
- X-ray radiation detectors

The electron beam position will be monitored by *1* Beam Position Monitor (BPM) placed in the region before the first Bragg mirror, and one after the outstream Bragg mirros and the current will be measured by means of *2* Rogowsky coils, placed before and after the cavity.

Beam position monitors require specifically designed electronics to reduce noise and achieve the required precision and sensitivity. The output data should be available for fast elaboration, in order to be used to send a fast interlock shut-off signal to the Power supply in case of beam loss.

RF detectors will be placed before the input Bragg Mirror. They will detect the fraction of the radiation that is lost by the RF cavity due to the non perfect reflectivity of the Bragg mirror, providing a signal proportional to the intensity of the RF inside the resonator.

X-Rays detectors will be placed in the area around the vacuum tube, to detect x-rays generated in case of beam loss. There will be *40* point detectors placed around the tube and distributed along it's length. The output data should be available for fast elaboration, in order to be used to send a fast interlock shut-off signal to the Power supply in case of beam loss.

- Fast analog outputs: *44* current fast readout to **custom electronics**, to verify the event of beam loss. In such a case a fast TTL signal will be sent to the Power supply interlock;
- Analog output: *50* voltages → to a **Digital-controlled ADC**;
- Total number of digital ports: *1* **Digital** (ADC).

J.1.3 Beam Dump

In the first stage of the project the electron beam is simply dispersed by the last coil system and is delivered to an annular lead-made beam dump. No electrical measurement is possible, due to the required electrical contact with the cavity. It's possible to inserts a few thermocouples inside the dump to detect temperature changes. In such a case a digital-controlled ADC to process 8 voltages should be added to the system.

J.1.4 RF Diagnostics

The radiation produced by the device should be characterized by means of specific instruments:

– Power meter

– Phase meter

Table J.4: **RF Cavity**

Electron beam diagnostics				
Parameter	**Action**	**Time**	**Data type**	**Interface**
4 Voltages (2 lines each BPM)	read	fast	Analog	→ to custom electronic & ADC
2 V - Custom electronic (BPM)	read	fast	Analog	TTL
2 Voltages (Rogowsky coils)	read	slow	Analog	→ to ADC
RF diagnostics				
Parameter	**Action**	**Time**	**Data type**	**Interface**
V - RF Diodes (4)	read	slow	Analog	–> to ADC
X-ray diagnostics				
Parameter	**Action**	**Time**	**Data type**	**Interface**
V - X ray detectors (40)	read	fast	Analog	–> to custom electronic & ADC
V - Custom electronic (X-ray)	read	fast	Analog	TTL

– Spectrum analyzer

– Beam profile monitor (for mode identification)

The power meter is simply a diode that will produce a voltage proportional to the RF intensity.The power meter can be moved by means of an x-y motorized system in the directions perpendicular to the beam axis, in order to provide a profile of the RF beam intensity. The control of Part of the radiation can be extracted by means of a waveguide to be delivered to a commercial spectrum analyzer. The waveguide is also splitted in two branches, one with a RF phase shifter, and the other with a variable attenuator, in order to provide a mean to perform a phase measurement with 2 diodes.

Other parameters could be available on the digital interfaces:

- Analog input/output: *5* voltages output + *2* voltage input → to an *8 + 2* **channels Digital-controlled ADC/DAC**;
- Total number of digital ports: *4* **Digital** (ADC).

J.1.5 Vacuum System

The Vacuum system is composed by *5* elementary blocks, each one including a Dry primary pump, a Turbomolecular pump, and an Ion pump, with different specifications, but all with the same structure for controllers and probes. For each block a high vacuum probe and *2* low vacuum probes are necessary. A gauge controller, able to read both low vacuum and high vacuum probes will be used. Digital interface is required both for pumps controllers and gauge controllers. Primary pumps will be only switched on and off by means of relays. In this document controllers able to read *3* probes will be considered, but controllers able to read up to *12* probes at the same time are available on the market. Three voltage controlled vacuum valves are also necessary for each of the pumping blocks. Two more bigger voltage controlled vacuum valves are necessary to be placed along main vacuum line. Vacuum loss should generate interlock signals to shut off power and to immediately shut valves, to avoid damages to the cathode. Such signals are usually generated by the probe controller itself, on the basis of programmed pressure thresholds.

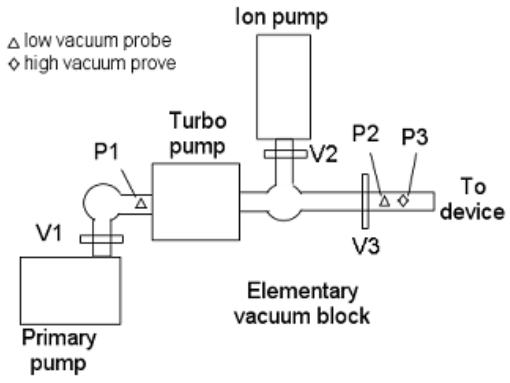

All controllers are commercial products, with digital interfaces, providing information about many parameters of the controlled devices. In the table only the interface is indicated, without the specification of the performed measurements.

- Relay switches: *22* high power relays (*24* **relays Ethernet or Digital controlled board**);
- TTL output (to interlock): *5*; can be combined in "OR" configuration to provide a single interlock signal to the Power supply;
- Total number of digital ports: *16* **Digital** (ADC).

Due to the large number of ports and to the fact that the feedback from the vacuum system does not need to be fast, it is advisable to have a dedicated computer controlling the vacuum components.

Resuming the situation, a table with the required interfaces and signals du be read is reported below.

The experiment is hosted in a radiation shielded area, all devices have to be controlled remotely and also the electronics should be shielded from x-radiation to avoid damages.

The large number of cables suggests the use of $RS242$ (or better $RS485$). In order to reduce the number of cables and electrical interferences two *16* ports serial to Ethernet servers could be used to send all the collected data to the control room using a single LAN cable. Such servers should be well shielded from the x-rays produced by the device.

The logical structure of the control system is simple enough and will make use of *4* PCs:

1. $PC1$: control of the main blocks of the device: Power supply, magnets, diagnostic for the e-beam and in the cavity section;
2. $PC2$: characterization of the produced radiation: RF diagnostics, RF beam profile, RF spectral content... all controls for devices that will make use of the produced radiation;
3. $PC3$: control of the vacuum system;
4. $PC4$: logging and data representation (synoptic layout with a graphic representation of the relevant parameters).

Our team has a long expertise in the use of Labview as software platform for instrumentation control, but also other solutions could be considered.

Software modules will be built to control each of the blocks of the control system, with automation procedures designed for safe operation of the machine.

Examples of such procedures are:

- Vacuum startup/shutdown procedure
- Power supply startup/shutdown procedures
- RF profile X - Y scanning procedure
- Beam position aligning procedure

Each module should be able to communicate with the other modules, to allow the simultaneous control of the different components of the device.

A PC will be dedicated to logging/data representation. All machine parameters will be collected at defined time intervals and data will be saved of this PC. Data will be used to show the actual machine situation on a graphic layout, providing a fast visual information about the system status.

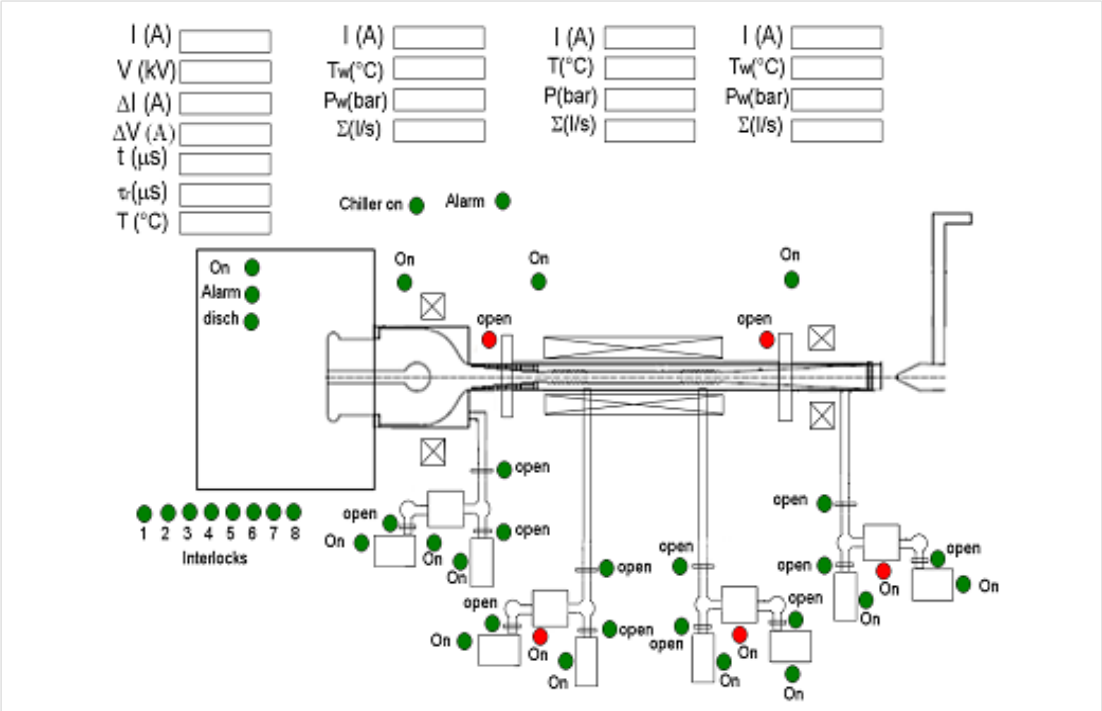

Figure J.2: Example of a graphic layout.

J.2 Costs

In the following table an estimation of the cost of the hardware is reported:

Choosing Labview or Pyton for the software would not increase the overall costs: ENEA already owns a site license for Labview, while Pyton is open source software.

It would be correct to consider buying some spare part for the commercial devices, in order to have a replacement available in case of malfunction of a device.

Table J.5: **RF Diagnostics**

Electron beam diagnostics				
Parameter/device	**Action**	**Time**	**Data type**	**Interface**
Power meter voltage (3)	read	slow	Analog	→ to ADC
Phase shifter	set	slow	Analog	DAC
Phase shifter	read	slow	Analog	→ to ADC
Variable attenuator	set	slow	Analog	DAC
Variable attenuator	read	slow	Analog	→ to ADC
Spectrum analyzer	read	slow	Digital control	Digital
Spectrum analyzer	set	slow	Digital data	Digital
Motor controller (2)	read	slow	Digital control	Digital
Motor controller (2)	set	slow	Digital data	Digital

Table J.6: **Vacuum system**

Each vacuum pumping block (× 5)				
Device/parameter	**Action**	**Time**	**Data type**	**Interface**
Primary pump ON/OFF	set	slow	Power supply	relay
Turbo controller	set	slow	Digital control	Digital
Turbo controller	read	slow	Digital data	Digital
Ion pump controller	set	slow	Digital control	Digital
Ion pump controller	read	slow	Digital data	Digital
Probe controller	set	slow	Digital control	Digital
Probe controller (3 probes)	read	slow	Digital data	Digital
Pressure threshold	read	fast	Analog	TTL
Valves controller × 3	set	slow	Power supply	relay
Vacuum line valves				
Parameter	**Action**	**Time**	**Data type**	**Interface**
Valves controller × 2	set	slow	Power supply	Relay

Table J.7: **Interfaces and signals**

Block	**Analog out**	**Analog in**	**Digital**	**notes**
Power supply/modulator		8	2	
Magnetic coils	19		6	3 Analog to fast c.e.
RF Cavity	50		1	44 Analog to fast c.e.
Beam dump	8		1	
RF Diagnostics	5	2	4	
Vacuum system	5	22	16	5 TTL, 22 relays

Table J.8: **Hardware costs in €**

Device	**n**	**Price x item**	**Total**	**notes**
PC	4	1250	5000	
Monitor	8	250	2000	
ADC multifunction x 32	4	2000	8000	
Serial to Ethernet converter 16 port	2	1500	3000	
Ethernet controlled 32 relays board	1	1000	1000	
Digital interfaces for PC	2	1000	1000	
Custom electronics			5000	
Network components			500	
Rack cabinet	1	2000	2000	
Power distribution	1	500	500	
Total			28000	

Technical Addendum K

Experimental Hall

The CARM device needs special requirements to be operated due to the safety issues mainly related to the high voltage and high current electron beam, but also to the high power and long pulse duration of the radiofrequency generated. The electron beam characteristics are such to generate undesired high intensity X-ray beams, in the case of bad electrons transport, or loss, along the transport channel. This accidental event necessitates a special experimental hall where the CARM could operate, far from human attendance, with adequate safety requirements and with a presence of a control room from which the experiment might be remotely operate.

In the ENEA Frascati Research Centre we have located a suitable area for the above purposes. This area has been used, in the past, for the Frascati Tokamak (FT) experiment, and offers all the features needed for a medium scale experiment, including electrical services, water, compressed air, a crane for the heavy loads movements, a carriage access and a control room. In the following two figures we ha reported a drawing plan and a sectional sketch of the FT room with the CARM device positioned respectively.

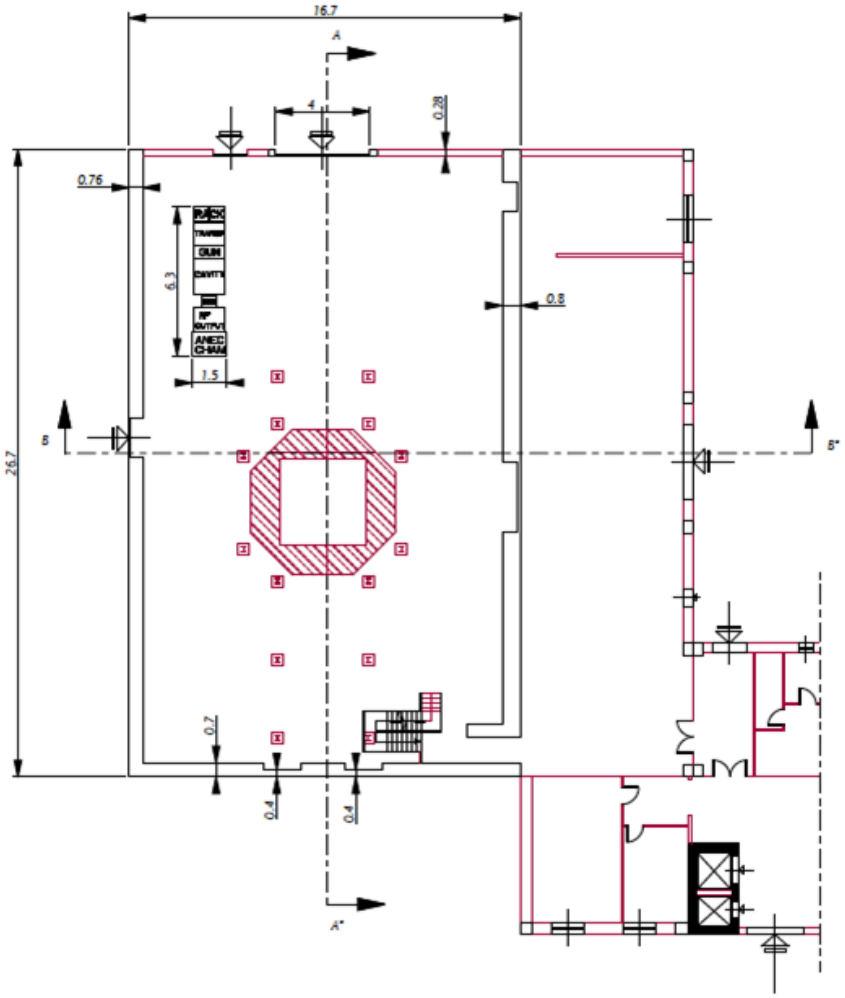

Figure K.1: Design plan of the CARM source in the FT room.

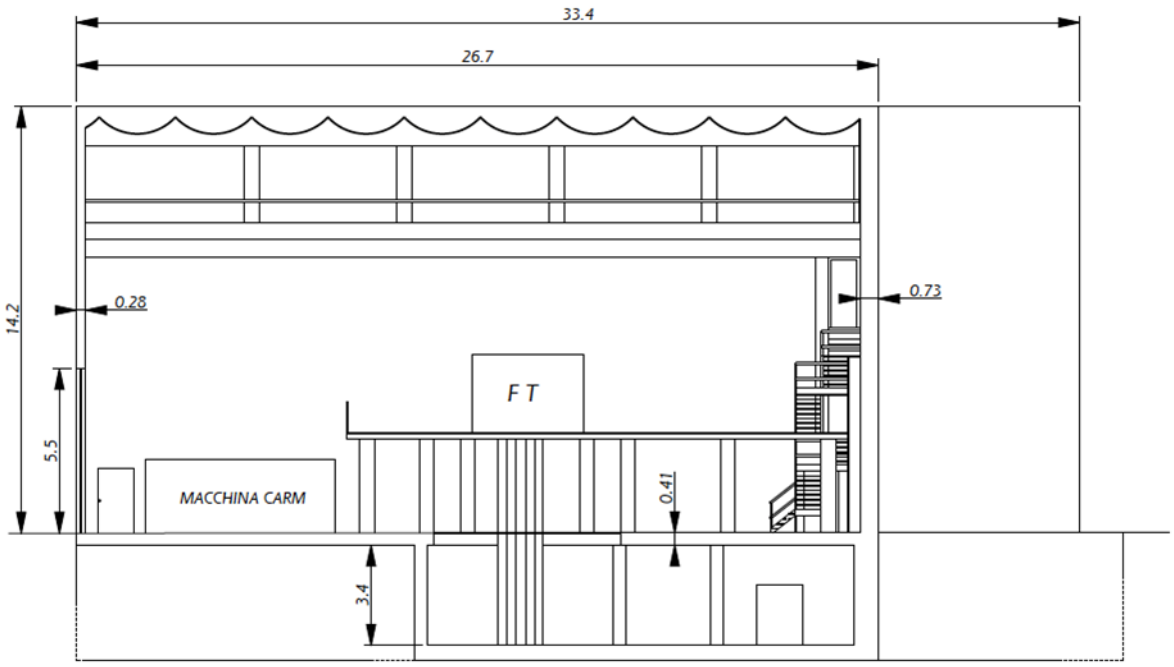

Figure K.2: Sectional drawing of the CARM source in the FT room.

Bibliography

[1] V. Erckmann and U. Gasparino, *"Electron cyclotron resonance heating and current drive in toroidal fusion plasmas"*, Plasma Phys. Control. Fusion 36, pp. 1869-1962 (1994).

[2] T.C. Luce, *"Applications of high-power millimeter waves in fusion energy research"*, IEEE Trans. on Plasma Science 30(3), pp. 734-754 (2002).

[3] R. Bartolini, G. Dattoli, L. Mezi, A. Renieri, M. Migliorati, M.E. Couprie, G. De Ninno, R. Roux, Phys. Rev. Lett., 2001 Sep 24;87(13).
R. Bartolini, G. Dattoli, L. Giannessi, L. Mezi, A. Renieri, M. Migliorati, C. Bruni, M.E. Couprie, D. Garzella, and G. Orlandi, Phys. Rev. E 69, 036501 (2004).

[4] G.G. Denisov et al., *"Development status of gyrotron setup for ITER ECW system"*, 40th Int. Conf. on Infrared, Millimeter and Terahertz waves 2015, Aug. 13-28, Hong Kong, China.

[5] Y. Yamaguchi et al., *"High power 303 GHz gyrotron for CTS in LHD"*, Journal of Instrumentation 10(10), pp. C10002 (2015).

[6] E. Poli et al., *"Electron-cyclotron-current-drive efficiency in DEMO plasmas"*, Nucl. Fusion 53(1), pp. 013011 (2013).

[7] S. Garavaglia et al., *"Preliminary Conceptual Design of DEMO EC System"*, AIP Conf. Proc. 1689, pp. 090009 (2015).

[8] J. Jelonnek et al., *"Developments for Future EU DEMO Gyrotrons - 2015 Update on Developments within EURO-fusion"*, Workshop on RF Heating Technology of Fusion Plasmas 2015, Aug. 31 -Sep. 2, Tokyo, Japan.

[9] I.T. Chapman et al., *"Empirical scaling of saw-tooth period for onset of neoclassical tearing modes"*, Proc. 22nd Int. Conf. Geneva, 2008) IAEA, (2008).

[10] V. Bratman, G. Denisov, N. Ginzburg, and M. Petelin, *"FEL's with Bragg reflection resonators: Cyclotron autoresonance masers versus ubitrons"*, IEEE J. Quantum Electron., vol. 19, no. 3, pp. 282–296, Mar. 1983.

[11] R.B. McCowan, A.W. Fliflet, S.H. Gold, V.L. Granatstein, and M.C. Wangh, *"Design of a waveguide resonator with ripled wall reflectors for a 100 GHz CARM oscillator experiment"*, Int. J. Electron., vol. 65, no. 3, pp. 463–475, 1988.

[12] AA. VV., 2007, IEEE *"Standard for Pulse Transformers"*, ANSI/IEEE Std 390^{TM}-1987 (R2007), pp. 1-42.

[13] D. Bortis et al., *" Design Procedure for Compact Pulse Transformers with Rectangular Pulse Shape and Fast Rise Times"*, IEEE Transactions on Dielectrics and Electrical Insulation Vol. 18, No. 4; 2011, 1171-1180.

[14] Y. Wang, et al., *"Optimal Design and Experimental Study of Pulse Transformers With Fast Rise Time and Large Pulse Duration"*, IEEE Trans. On Plasma Science, In press, 1-7.

[15] J.D. Jackson, *"Classical Electrodynamics"*, John Wiley & Sons, Inc, (1998).

[16] E.E. Callaghan, S.H. Maslen *"The Magnetic Field of a Finite Solenoid"*, (Technical note D-465), Washington, USA: Nation Aeronautics and Space Administration, (1960).

[17] http://www.df.unipi.it/˜fuso/dida/solenoide.pdf

[18] D.B. Montgomery, *"Solenoid Magnet Design"*, Wiley-Interscienc.

[19] , G. Nusinovich, *"Introduction to the physics of Gyrotrons"*, The Johns Hopkins University Press, June 2004.

[20] , E. Saldin, E.V. Schneidmiller and M.V. Yurkov, *"The Physics of Free Electron Lasers"*, Springer-Verlag Berlin Heidelberg 2000.

[21] Gapanov et al., *"The induced radiation of excited classical oscillators and its use in high-frequency electronics"*, Radiophys. Quantum Electron. 10(9), pp. 794-813 (1967).

[22] V.L. Bratman, N.S. Ginzburg and M.I. Petelin, *"Common properties of free electron lasers"*, Opt. Commun., vol. 30, no. 3, pp. 409–412, 1979.

[23] S. Ceccuzzi et al., *"The High Gain Integral Equation for CARM-FEL Devices"*, IEEE J. Quantum Elect. 51(7), pp. 1-9 (2015).

[24] A.W. Fliflet, *"Linear and non-linear theory of the Doppler-shifted cyclotron resonance maser based on TE and TM waveguide modes"*, Int. J. Electron., vol. 61, no. 6, pp. 1049–1080, 1986.

[25] V.L. Bratman et al., *"Relativistic gyrotrons and cyclotron autoresonance maser"*, Int. J. Electron. 51(4), pp. 541-567 (1981).

[26] G.S. Nusinovich, Latham and Li, *"Efficiency of frequency Up-Shifted Gyrodevices: Cyclotron Harmonics Versus CARM's "*, IEEE Trans. Plasma science, Vol.22, No. 5, October 1994.

[27] G. Dattoli, P.L. Ottaviani and S. Pagnutti, *"Booklet for FEL Design: A Collection of Practical Formulae"*, Frascati, Italy: Edizioni Scientifiche Frascati, 2007.

[28] Marcello Artioli, Giuseppe Dattoli, Pier Luigi Ottaviani, Simonetta Pagnutti, *"Virtual Laboratory and Computer Aided Design for Free Electron Lasers outline and simulation"*, Energia Ambiente e Innovazione / Anno 2012 / n. 3 Maggio-Giugno 2012.

[29] T. Marshall, *"Free Electron Lasers"*, New York, NY, USA: Macmillan, 1985;

[30] G. Dattoli, A. Renieri and A. Torre, *"Lectures on the Free Electron Laser Theory and Related Topics"*, Singapore: World Scientific, 1993;

[31] P. Luchini and H. Motz, *"Undulators and Free-Electron Lasers"*, Oxford university press W.B. Colson, *"Classical Free Electron Laser Theory"*, Chapter 5, pages 115-194, in "Free Electron Laser Handbook", W. B. Colson, C. Pellegrini and A. Renieri (editors), North-Holland Physics, Elsevier Science Publishing Co. Inc., The Netherlands (1990).

[32] C. Chen, S. Wurtele, *"Linear and non linear theory of cyclotron autoresonance masers with multiple waveguide modes"*, Phys. Fluids B 3, 2133 (1991).

[33] N. Kroll, P. Morton and M.N. Rosenbluth, IEEE J. Quantum Electron. 17, 1436 (1981).

[34] G. Dattoli, S. Pagnutti, P.L. Ottaviani, and V. Asgekar , *"Free electron laser oscillators with tapered undulators: Inclusion of harmonic generation and pulse propagation"*, Phys. Rev. ST Accel. Beams 15, 030708 – Published 22 March 2012.

ENEA
Promotion and Communication Service
www.enea.it

October 2016